UNIVERSITY OF NOVA GORICA
GRADUATE SCHOOL

SPECTROSCOPIC INVESTIGATION OF OXYGEN VACANCIES IN CeO_2

DISSERTATION

Thanveer Thajudheen

Mentor: Prof. Dr. Matjaž Valant

Nova Gorica, 2021

UNIVERZA V NOVI GORICI
FAKULTETA ZA PODIPLOMSKI ŠTUDIJ

SPEKTROSKOPSKE RAZISKAVE KISIKOVIH VRZELI V CeO_2

DISERTACIJA

Thanveer Thajudheen

Mentor: Prof. Dr. Matjaž Valant

Nova Gorica, 2021

UNIVERSITY OF NOVA GORICA
GRADUATE SCHOOL

Thanveer Thajudheen, *Spectroscopic investigation of oxygen vacancies in CeO_2,* Dissertation, (2021)

Dedicated to

Umma and Thayicha

Acknowledgement

I express my gratitude to prof. dr. Matjaž Valant for his support during this whole thesis. His guidance, motivation, and criticisms made this thesis a reality. I would like to thank prof. dr. Mattia Fanetti who trained me to use SEM and especially the use of the Cathodoluminescence (CL) system on which this thesis is based on. I thank prof. dr. Sandra Gardonio for helping me understand the fitting and analysis of CL emission spectra. I thank prof. Iztok Arčon for EXAFS experiments and his help throughout data analysis and interpretation.

Many thanks to Ms. Mojca Vrčon Mihelj for helping me in the laboratory in the early stages of experiments. I would like to extend my gratitude to assist. prof. dr. Luigi Giacomazzi, and prof. dr. Egon Pavlica for the fruitful discussions. I thank dr. Rizwan Zahoor who helped me immensely during my move and stay in Slovenia. My deep gratitude to Gašper Kukec Mezek, Zipporah Rini Benher, Manel Machreki, Takwa Chouki, dr. Akansha Mehta, Uroš Luin, Arun Ravindran and all the other lab members whose friendship and presence helped me a lot the whole time.

I thank my parents who helped me do this even if it kept me away from them for a long time. My family and friends whom I don't mention by name here, every one of them was an indispensable part of this journey and I thank them all wholeheartedly.

I would like to acknowledge the financial support from javni štipendijski sklad (ad-futura program), Slovenia. I also would like to acknowledge access to synchrotron radiation facilities ELETTRA (beamline XAFS, pr. 20185092) in Italy and PETRA III at DESY (P65 beamline, project number I-20200036 EC) in Germany.

Abstract

A unique material, ceria (CeO_2), which is widely applied in automobile exhaust catalysts, is functional due to presence of defects in its crystal structure. Furthermore, the structural defects dictate electrical and chemical properties of ceria. The creation of intrinsic oxygen vacancies in ceria is responsible for oxygen-ion conductivity in solid oxide fuel cells. This unfolds the keen interest in ceria defects. Using the analytical technique cathodoluminescence spectroscopy (CLS) we can characterize ceria for its band gap and the defect states within the band gap. Since CLS has a high spatial resolution, high sensitivity to low concentration of defects and ability to obtain depth resolved information it is an obvious technique of choice.

The first part of the thesis is an introduction to the topic and description of the experimental techniques. Importance of ceria as a multifaceted material finding applications in areas spanning from energy production and conversion to biomedical applications is detailed. CLS as a tool to understand defect-related optical properties and advancement in the CL detection systems are discussed. To study the relationship between local structure and its impact on CL emission spectra, an X-ray absorption spectroscopy techniques were used. The X-ray absorption near edge structure (XANES) and the Extended x-ray absorption fine structure (EXAFS) techniques are summarized.

The second part discusses CL emission from ceria. Initially, CL emission from reduced ceria and its dependence on oxygen vacancy concentration are presented. The origin of emission was attributed to different configurations of the oxygen vacancies and polarons. The recent F center description in ceria was adopted here. The intriguing observation of CL emission quenching as a function of oxygen vacancy concentration was explained on the basis of a relative change in population of F centers in ceria. This demonstrated the relevance of local structure for the CL emission in ceria. In order to have a better understanding of the system, La-doped ceria was proposed as a model system. A precise control over the stoichiometry helped to achieve a desired oxygen vacancy concentration. The CL emission behavior, as observed in reduced ceria, was replicated in the case of La-doped ceria and the analysis revealed that F^+ centers favor CL emission whereas F^0 centers are disadvantageous. The local structure investigation using EXAFS analysis of both cations Ce and La (K-Edge) showed distortion from the fluorite symmetry and corroborated the F center description of oxygen vacancies in ceria. Our results provide an experimental evidence for F center description involving oxygen vacancies and polarons.

Key words: ceria, cathodoluminescence spectroscopy, local structure distortion, EXAFS analysis, La doped ceria, luminescence quenching, F centers

Povzetek

Uporaba cerijevega dioksid (CeO_2) kot katalizatora v avtomobilskih izpušnih sistemih je pogojena s prisotnostjo napak v njegovi kristalni strukturi. Te napake določajo električne in kemične lastnosti tega materiala. Prisotnost lastnih kisikovih vrzeli v materialu je odgovorna za prevodnost kisikovih ionov v trdnih oksidnih gorivnih celicah. Z uporabo katodoluminescenčne spektroskopije (CLS) lahko karakteriziramo energijsko vrzel cerijevega dioksida in dodatne pasove znotraj energijske vrzeli, ki nastanejo zaradi strukturnih napak. Metoda CLS je očitna izbira, predvsem zaradi visoke prostorske ločljivosti, visoke občutljivosti na nizko koncentracijo napak in sposobnosti pridobivanja informacij o globinski strukturi materiala.

Prvi del disertacije je uvod v temo in opis uporabljenih eksperimentalnih metod. Prav tako podamo podroben opis in pomembnost cerijevega dioksida kot vsestransko uporabnega materiala na področjih proizvodnje in pretvorbe energije ter za biomedicinsko uporabo. Opisali smo CLS kot orodje za razumevanje optičnih lastnosti, ki nastanejo zaradi strukturnih napak, ter napredek pri razvoju detekcijskih sistemov CL. Pri preučevanju razmerja med lokalno strukturo in njenim vplivom na emisijske spektre CL smo uporabili rentgensko absorpcijsko spektroskopijo. Od tega smo povzeli metodi analize obrobnih struktur rentgenske absorpcije (amg. X-ray absorption near edge structure - XANES) in analize finig struktur podaljšane rentgentske absorcije 8ang. Extended X-ray absorption fine structure - EXAFS).

V drugem delu obravnavamo CL emisijo cerijevega dioksida. Predstavimo CL emisijo reduciranega cerijevega dioksida in njegovo odvisnost od koncentracije kisikovih vrzeli. Izvor emisije smo pripisali različnim konfiguracijam kisikovih vrzeli in polaronov. Pri tem smo uporabili nedavno sprejet opis F centra v cerijevem dioksidu. Na podlagi relativne spremembe populacije njegovih F centrov razložimo zanimivo dušenje CL emisije kot funkcijo koncentracije kisikovih vrzeli. To je pokazalo na pomemben vpliv lokalne strukture na CL emisijo cerijevega dioksida. V disertaciji smo uporabili La-dopiran cerijeve dioksida kot model, na osnovi katerega lahko bolje razumemo sistem. Z natančnim nadzorom nad stehiometrijo smo dosegli želeno koncentracijo kisikovih vrzeli. Preko CL emisije smo opazili, da se z La dopiran cerijev dioksid obnaša enako kot reduciran cerijev dioksid, analiza pa je pokazala, da F^+ centri inducirajo CL emisijo, medtem ko jo F^0 centri dušijo. Preiskava lokalne strukture obeh kationov, K-robu Ce in La, z uporabo EXAFS analize je pokazala popačenje strukture fluorita in potrjuje opis F centrov kisikovih vrzeli v cerijevem dioksidu. Naši rezultati zagotavljajo eksperimentalne dokaze za opis F centrov, ki vključujejo kisikova vrzeli in polarone.

Ključne besede: cerijev dioksid, katodoluminescenčna spektroskopija, popačenje lokalne strukture, analiza EXAFS, La-dopiran cerijev dioksid, luminescenčno dušenje, F centri

Table of Contents

We all look for perfections around us and within us; to some extent we are all pursuing it. But the fact is that the imperfection is the essence of reality we live in. It is interesting to note that imperfections in crystals make them functionally important. Because of these imperfections (aka defects) they are qualified to be a part of our technology.

1 Introduction

The interest in the crystal structure, defect chemistry, electronic structure, ionic and electronic conductivities of ceria, CeO_2, and doped ceria derivatives comes from a variety of industrial applications that these materials can be used for, ranging from environmental to medical applications. Due to the inert nature of the material, CeO_2 is compatible with a vast range of biological and inorganic materials. It is noteworthy that CeO_2 is stable even under harsh conditions like high temperatures (up to 2000^{o}C) and is abundant in earth's crust. [1] The multifaceted usefulness of the material arises as a result of its remarkable ability to sustain a high density of point defects (especially oxygen vacancies) in the crystal structure, which can be used for tailoring its functional properties.

1.1 Applications of CeO_2

Here I give a brief account of ceria and its derivatives with regards to well established areas to niche and prototypical applications.

1.1.1 Three-Way Catalysts

The well-established application of CeO_2 is in the automotive three-way catalysts (TWCs). The role of the TWCs in the exhaust of an automobile is to assist in oxidation of CO and unburned hydrocarbons and in reduction of nitrogen oxides (NO_x). The role of ceria and ceria-based materials to act as a promoter in TWCs has been associated with its property known as oxygen storage capacity (OSC). The ability of these materials to transform between Ce^{3+} and Ce^{4+} oxidation states is known as OSC. The introduction of CeO_2-based TWCs in 1970s-1980s, dramatically improved the performance of TWCs. The method of preparation of TWC consists of co-impregnation of noble metals and CeO_2 precursors on doped Al_2O_3 support. [2]

The next generation of CeO_2-based TWCs developed in the mid-1980s was able to achieve performance enhancement, but it was not sufficient to meet the standards set in the USA and Europe for car pollution control. The decrease of OSC due to CeO_2 sintering and the loss of contact between CeO_2 and the noble metals were the problems related to these TWCs. [3]

Today's TWCs employ CeO_2-ZrO_2 solid solution instead of pure CeO_2. Because ZrO_2 in the CeO_2 lattice enhances OSC of the materials by improving the activity of the catalyst and reducing emission at the start of the engine. [4] Since TWCs are exposed to high temperature for very long periods, the active components get sintered. Sintering leads to the depletion of the exposed metal surface area, and loss of contact between noble metal particles and the CeO_2-based promoter. It is found that CeO_2- ZrO_2 solid solutions are more resistant to sintering than bare CeO_2. [5] Additionally, CeO_2- ZrO_2 on the doped Al_2O_3 prevents the transformation of Al_2O_3 into the alpha form which has very low surface area. [6,7]

1.1.2 Solid Oxide Fuel Cells

Ceria has proven to be useful in multi-dimensions in solid oxide fuel cells (SOFCs). (the multi-dimensional use of Ceria in SOFCs is well known). Ceria finds application in SOFC as: (1) an electrolyte, (2) as a barrier layer for cathodes and (3) as a catalyst in both cathodes and anodes. [8]

An example for ceria as catalyst is a Gd-doped ceria anode, in which performance increase has been attributed to an increase in the oxygen vacancy concentration as a result of the doping. [9] An yttria-doped ceria (YDC) anode has been used for intermediate temperature SOFC. [10] A comparison of Ni-yttria stabilized zirconia (Ni-YSZ) and Ni-samaria-doped ceria (Ni-SDC) as anodic components showed that a performance improvement in the case of Ni-SDC. Such an enhancement has been attributed to the higher catalytic activity that results from the partial reduction of Ce^{4+} to Ce^{3+} under reducing atmosphere. [11]

As an electrolyte, the ceria-based composites have been explored in great detail because of its high ionic conductivity and electronic insulator properties. [12,13] The classic dopants include gadolinium, samarium, yttrium, and calcium. Recently, the trend has converged to studies of two-phase electrolytes since such materials can offer an improved ionic conductivity arising from the binary conductive nature (O^{2-}/H^{+}). In this class, the most promising candidate is obtained by combining ceria with carbonates. [14–19] Currently, composite electrolyte materials containing doped ceria and oxides ($BaCe_{0.8}Y_{0.2}O_{3-\delta}$, Y_2O_3) [20–24], hydroxides (NaOH) [23], and sulfates (Li_2SO_4) [24] are also becoming more and more popular two-phase electrolytes.

1.1.3 Photocatalysis

A transition from the conventional TiO_2 photocatalyst for wastewater treatment [25–29] and water splitting [30,31] to cerium-based materials has been seen in the literature. Since CeO_2 is a wide band gap semiconductor the photogeneration of charge carriers is achieved by UV light. A band gap reduction has been reported for mesoporous ceria due to the presence of Ce^{3+}. [32] Also a defect engineering approach through electron beam irradiation was shown to be effective to narrow the band gap of pristine CeO_2 and, thereby, enhance the visible light activity. [33] The introduction of the oxygen vacancies can improve the photocatalytic activity of ceria, because

the oxygen vacancies act as strong binding and dissociation sites for adsorbates and prevent hole-electron recombination by acting as electron traps. [34]

Another side of the story regarding the catalyst performances is about mobility of the oxygen vacancies. A recent study on mesoporous nanorod like ceria in the temperature range 160-240°C showed that the photocatalytic activity can be improved by enhancing the mobility of oxygen vacancies. [32] Similar performance improvement has been reported for Y-doped ceria. [34] The comparison of photodegradation of methylene blue by TiO_2, CeO_2-doped TiO_2 and CeO_2-ZrO_2 co-doped TiO_2 showed that the catalytic performances of the catalysts improved by the addition of CeO_2. [35–37]

1.1.4 Biomedical Applications

Due to the fast transition between Ce^{4+} and Ce^{3+}, ceria has multi-enzyme mimetic properties. It has a potential in a large variety of medical applications: catalase mimetic activity, hydroxyl radical scavenging and oxidase mimetic activity and phosphatase-mimetic activity. [38] The remarkable biomedical performances of ceria are tied to its redox capability and the possibility of vacancy engineering by making nanostructured materials. Ceria can effectively interact with many radicals and superoxides and it has also been tested for its ability to protect against oxidative stress. [39–41] Nano ceria has been found to be effective to protect primary cells from radiation therapy and to prevent retinal degeneration induced by intracellular peroxides. [42]

From the advent of semiconductor industry, it was clear that crystal defects have immense potential for the advancement of the technology. All the applications explained above exploit the property of ceria to create and maintain oxygen vacancies in the crystal structure. In this regard understanding the fundamental nature of oxygen vacancies in CeO_2 has utmost importance. The defect structure of oxygen vacancies in CeO_2 is still a debatable issue. A coordination number of the cation and the geometry of the defect structure is not resolved yet. In this thesis I addressed these problems using different spectroscopic techniques. Delivering new insights into the cathodoluminescence emission of ceria is another objective of this thesis. In the next sections I will give a brief background of CeO_2 crystal structure, defects structure and electronic structure. Then the unresolved issues about the oxygen vacancies in CeO_2 will be discussed.

1.2 Defects are Inevitable

Perfect crystals are fictitious; the defects in the crystals are thermodynamic necessity. From a thermodynamic perspective for a crystal, it is energetically favorable to have defects. The Gibbs free energy of a crystal is given by

$$\Delta G = \Delta H - T\Delta S \tag{1.1}$$

Where H is the enthalpy and S is the configurational entropy. Let's ponder the effect of creating a defect on the free energy of a perfect crystal. Creating a defect, say a cation vacancy, is associated with a gain in ΔH. But the increase in configurational entropy S is larger because of the large number of positions a defect can occupy. The configurational entropy is given by the Boltzmann equation:

$$S = k \ln \Omega \tag{1.2}$$

Where Ω is proportional to the number of cation sites. So, the creation of a cation vacancy is associated with an increase in ΔH, the subsequent increase in entropy outweighs it and results in a reduction of free energy ΔG. Free energy change as a function of defect concentration is shown in Figure 1.1. At the equilibrium, the free energy changes due to the defect formation. $\frac{d\Delta G}{dn}$ is zero and the minimum in the free energy curve corresponds to the equilibrium number of defects in the system.

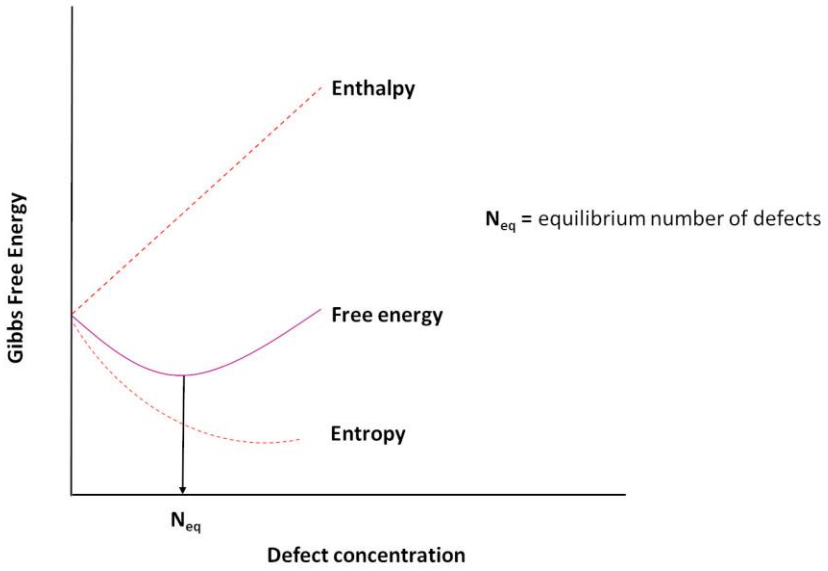

Figure 1. 1. Variation of free energy as a function of defect concentration. The minimum in the free energy curve corresponds to the equilibrium number of defects. Adapted from Ref. [43]

On the other hand, if the defect concentration is extremely high then the entropy change introduced by creating more defects is smaller compared to the energy required to create more defects. Hence, such a high concentration of defects may not be possible in a thermodynamic equilibrium. Nevertheless, the defect concentration in a solid can be tailored by means of chemical stoichiometry, doping, and quenching etc. The stoichiometric changes (slight variation in one of the components) can lead to defects concentration other than the equilibrium concentration for an ideally stoichiometric system. Also the addition of impurities (doping) will cause change in the defect concentration as a result of charge conservation. Furthermore, a fast cooling from high temperatures (quenching) can lead to frozen defect concentrations typical for the high temperatures.

1.2.1 Kröger-Vink Notation

The system suggested by Kröger and Vink helps to describe point defects in crystals analogous to atoms and molecules in chemical reaction equations. [44] Consider a crystal AB, the notation for an atom A on an A-site is A_A whereas a vacancy on B site is denoted as V_B. The atoms

occupying the interstitial sites are written as A_i or B_i. In this notation, the excess charge relative to the neutral lattice is counted. The neutral charge is represented by a cross ($\times$), while an excess positive charge is marked by a dot ($\bullet$) and negative charge is denoted by a dash ('). Thus, if an A atom occupying the A-site is neutral with respect to the lattice is denoted as $A_A^{\times}$, a positive excess charge is denoted $A_A^{\bullet}$ and a negative charge is marked as A_A'.

As an example, we consider NaCl crystal. In this case the Kröger -Vink notation and its meaning are the following:

$Na_{Na}^{\times} \rightarrow$ Na on Na-site

$V_{Na}' \rightarrow$ a vacancy on the Na-site

$Na_i^{\bullet} \rightarrow$ an interstitial Na ion

$Ca_{Na}^{\bullet} \rightarrow Ca^{++}$ ion on the Na-site.

Using this method, it is quite easy to write reactions involving point defects. For instance, formation of Schottky defects for a crystal AB can be written as

$$A_A + B_B = V_A' + V_B^{\bullet} + AB \tag{1.3}$$

For the Frenkel defect formation, it becomes

$$A_A + V_i = V_A' + A_i \tag{1.4}$$

Note that by definition an interstitial is occupied by a vacancy and denoted as V_i.

1.2.2 Types of Point Defects

Any sort of deviation from a perfect crystal is considered as a defect. An atom/ion missing from its usual position is termed as a **vacancy**. If the atom is displaced from its normal position in the crystal structure to a gap site that is under ordinary circumstances not occupied, is called an **interstitial**. An **anti-site** defect occurs when an atom of one type of ion in the solids occupies a

crystallographic site of another type of ion (cation vs. anion). The vacancy, interstitials and anti-sites are **intrinsic** point defects, since their origin can be traced back to the material seeking thermodynamic equilibrium. **Extrinsic defects** arise as a result of the presence of foreign atoms in a pure material. This foreign atom either could be an impurity or a dopant (deliberately added atom). For instance, an impurity ion such as Ca^{2+} substitutes for Na^{+} in the ionic solid NaCl. In this case a Na^{+} vacancy is created to compensate for the charge imbalance. The substitution of atom in a material could be such that both the original atom and the substituting atom have the same oxidation state, and it is called **isovalent substitution**. When the replacing atom is in a different oxidation state compared to the original atom, it is called **aliovalent substitution**. Doping is the way to control concentration of charge carriers in semiconductors. Adding phosphorous to silicon leaves behind a phosphorous valence electron weakly bound to it. This delocalized electron can be thermally ionized and results in conduction. On the other hand, doping silicon with nitrogen does not yield a weakly bound electron. All the electrons from the nitrogen form bonds with silicon, thus they are localized. [43]

1.2.3 Schottky Defect

The Schottky defect arises as a result of an equal number of cations and anions missing from their regular sites in the crystal. [43] This is a stoichiometric defect, which does not alter the stoichiometry of the compound. The electro-neutrality is maintained. The Schottky defect for an ionic crystal is schematically shown in the Figure 1.2. It is commonly found in ionic solids such as halides or oxides. For a general compound MO, the formation equation for Schottky defect can be written as,

$$M_M + O_O \rightleftharpoons V_M'' + V_O^{\bullet\bullet} + M_M + O_O \tag{1.5}$$

Or rather

$$\phi \rightleftharpoons V_M'' + V_O^{\bullet\bullet} \tag{1.6}$$

And concentration of these defects are expressed as,

$$K_S = [V_M''][V_O^{\bullet\bullet}] = \exp\left(-\frac{\Delta g_S}{kT}\right) \tag{1.7}$$

where Δg_S is the free energy of formation of a Schottky defect and K_S is mass action constant.

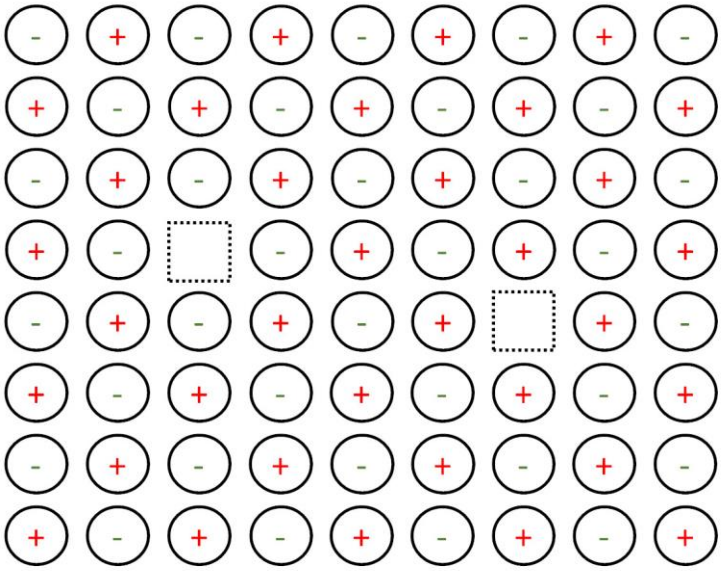

Figure 1. 2. Schematic representation of Schottky defect in an ionic crystal. The cations are represented as (+) and anions as (-). The vacancy is represented by the dashed rectangle. Adapted from Ref. [43]

1.2.4 Frenkel Defect

Frenkel defect is another stoichiometric defect resulting from the displacement of an atom from its lattice site into an interstitial site that is supposed to be vacant. [43] AgCl is an example for a material with predominantly Frenkel defects. Figure 1.3 shows a schematic representation of such a defect. If the Frenkel defect is associated with the displacement of anions off their lattice site into interstitial position, then it is called anti-Frenkel defects. The formation equation for Frenkel defect is:

$$M_M^{\times} \rightleftharpoons M_i^{\bullet\bullet} + V_M'' \tag{1.8}$$

and their concentration can be expressed as

$$K_F = [\mathrm{M_i^{\bullet\bullet}}][V_M''] = \exp\left(-\frac{\Delta g_F}{kT}\right) \quad (1.9)$$

where Δg_F and K_F are the free energy for formation of a Frenkel defect and mass action constant, respectively.

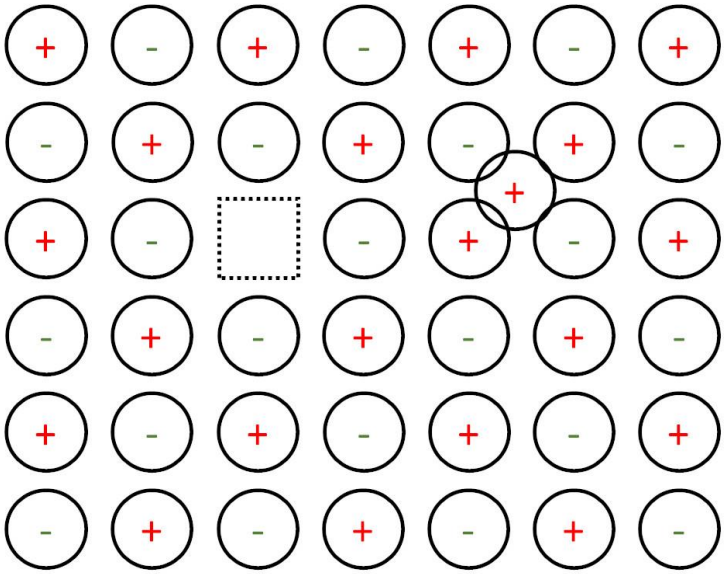

Figure 1. 3. Frenkel defect in an ionic crystal. The cations are represented as (+) and anions as (-). The vacancy is represented by the dashed rectangle. Adapted from Ref. [43]

1.2.5 Color Centers

Color centers are electrons trapped in an anion vacancy. Because an anion vacancy is essentially a positive charge, the electrons get trapped in it. The well-known example of a color center is the F-center (Farbenzentre) in crystals. In the F-centers the trapped electron at the anion vacancy has a series of energy levels available and the electron can jump from one level to the other. If the energy required to transfer electron from one level to another falls within the visible region of the electromagnetic spectrum, the crystal appears colored. The magnitude of these energy levels depends on the host crystal. For example, NaCl heated in K vapour has yellowish colour whereas KCl heated in K vapour has violet color. [43]

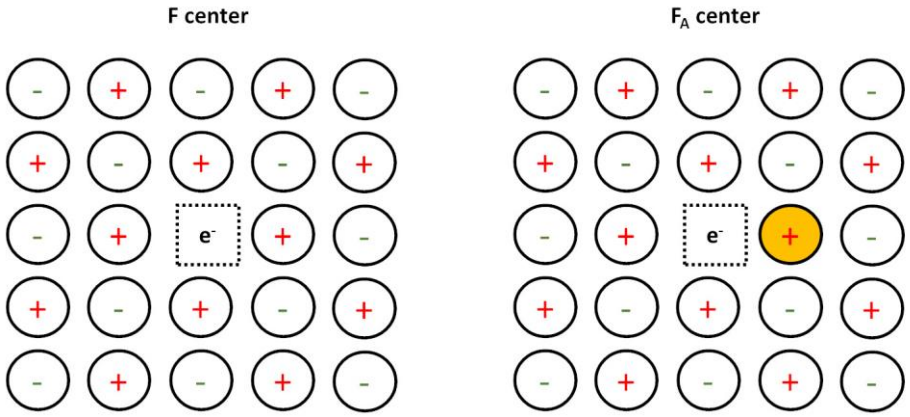

Figure 1. 4. The F and F_A center structures in alkali halides. Ions are represented by their respective charges. Adapted from Ref. [45]

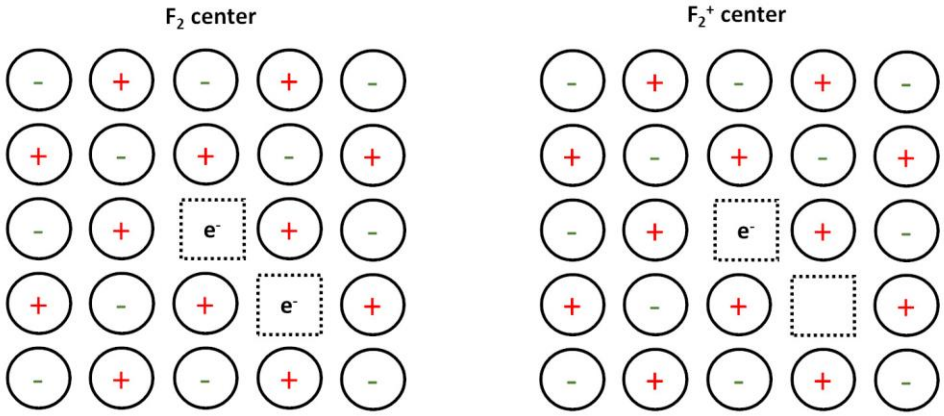

Figure 1. 5. The F_2 and F_2^+ center structures in alkali halides. Ions are represented by their respective charges. Adapted from Ref. [45]

Apart from the simple F center, aggregates of these basic centers can lead to other F centers as shown in Figure 1.4 and Figure 1.5. An F_2 center has two F centers in nearest neighbor positions. Depending on the number of F center that coagulate they can be termed as F_3, F_4 centers and so on.

From an application perspective, the F centers that are useful in solid state lasers are F_A and F_2^+ color centers. If one of the neighboring cations in an F center is replaced by another cation that is

different from the host lattice, we will get a F_A center. The F_2^+ center has been formed as a result of removal of an electron from an F_2 center.

There are different methods for formation of F centers. The two main experimental methods are (i) additive coloration: heating alkali halide crystal in an alkali vapor atmosphere followed by rapid cooling and (ii) irradiation: using UV, x-rays, γ-rays or electrons to create the anion vacancies. After the generation of certain concentration of F centers, the other centers can be created by different aggregation or illumination processes. [45]

The F center can be approximated as a particle in a box problem (i.e., an electron trapped in a vacancy). Solving Schrödinger's equation for an electron trapped in a cubic box of side 2a, the energy eigenvalues are given by,

$$E_n = \frac{h^2}{8m_0(2a)^2}\left(n_x^2 + n_y^2 + n_z^2\right) \tag{1.10}$$

Where h is Planck constant, m_0 is the mass of electron and n_x, n_y and n_z are quantum numbers taking integer values 1,2,3…

The ground state energy for the F center E_F is given by,

$$E_F = \frac{3h^2}{8m_0}\frac{1}{(2a)^2} \tag{1.11}$$

But the experiments showed variation from equation (1.11) because the F centers are not exactly cubic box (it's a rough approximation) and also they are not rigid but dynamic. In the dynamic structure, the neighboring ions move about their equilibrium position, hence the size of the box changes. For these reasons the absorption and emission peaks corresponding to F centers are broad and have large Stokes shifts. Although, F_A and F_2^+ color centers are great for tunable solid-state laser applications, the use of the color centers as lasers is limited. The special case of F centers in CeO_2 is detailed in Chapter 4.

1.3 Crystal Structure, Point Defects and Electronic Structure of CeO_2

CeO_2 crystallizes in a cubic fluorite crystal structure. Ce ions are occupying the cube corners and face centers of the unit cell while O ions are positioned in the interstitial sites. Figure 1.6 shows the unit cell of the CeO_2 crystal structure. The Ce atoms occupy the 4a sites of the *Fm-3m* space group, while oxygen anions fill the 8c sites. This results in an 8-fold coordination of Ce and 4-fold tetrahedral coordination of O ions.

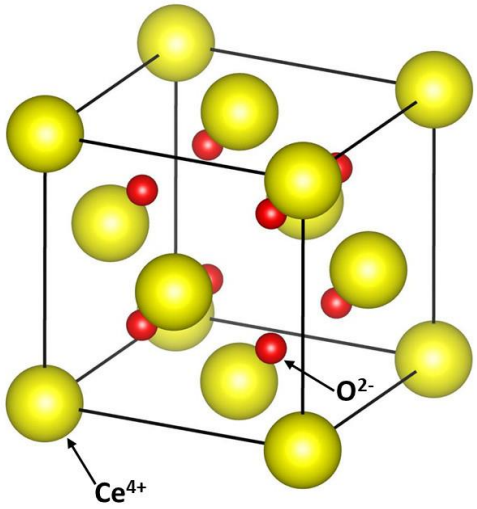

Figure 1. 6. Crystal structure of CeO_2. Ce atoms (yellow) occupying cube corners and face centers, the O atoms (red) form a simple cube within the face centered cubic array Ce ions. Drawing produced by VESTA. [46]

The electronic structure of CeO_2 (Figure 1.7) is still a debatable issue. It has two gaps, one between O2p and Ce4f states and one between O2p and Ce5d states. The valence band is composed of O2p orbitals and the conduction band is composed of Ce5d orbitals. The gap between O2p and Ce5d is 6 eV, while the O2p – Ce4f gap is about 3.3 eV. The native point defects in ceria are the following.

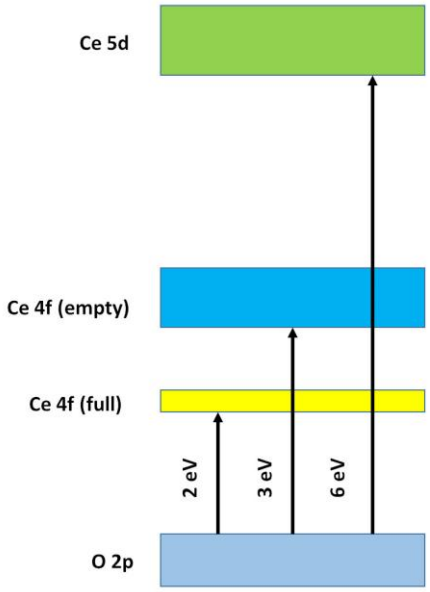

Figure 1. 7. Schematic of the electronic structure of CeO_2. O (2p) and Ce (5d) band gap is ~6 eV, whereas O (2p) and Ce (empty 4f) level lie about 3 eV apart.

1.3.1 Oxygen Vacancy

When an oxygen atom leaves the lattice position, two Ce atoms change their oxidation state from Ce^{4+} to Ce^{3+}. Because of the localization of two electrons, left behind by oxygen atoms, on two cerium atoms. Hence a doubly charged vacancy at an oxygen lattice is formed.

The oxygen vacancy formation can be written in Kröger -Vink notation as follows:

$$O_O^{\times} + 2Ce_{Ce}^{\times} \rightarrow V_O^{\bullet\bullet} + 2Ce_{Ce}' + \frac{1}{2}O_2(\mathrm{g}) \qquad (1.12)$$

Where $Ce_{Ce}^{\times}$ is a neutral cerium at cerium site; $O_O^{\times}$ represents a neutral oxygen at the oxygen lattice; $V_O^{\bullet\bullet}$ is a vacancy at the oxygen lattice site with two positive charges; and Ce_{Ce}' is cerium at a cerium lattice site with single negative charge (Ce^{3+}).

Since a vacancy site is an effective positive charge center, the neighboring oxygen atoms move toward the vacancy while the Ce atoms move away from the vacancy. [47] It is also found that the formation of oxygen vacancy in the CeO_2 crystal is facilitated by the presence of two Ce^{3+} atoms. Besides, the most favorable position of these two Ce^{3+} atoms in the CeO_2 crystal is next

to the oxygen vacancy. [48] The electronic density of states for an oxygen vacancy in CeO_2 (with ferromagnetic arrangement of electrons) is shown in Figure 1.8. The appearance of a peak (at 1.3eV), as a result of oxygen vacancy, indicates the presence of Ce^{3+} ions. [49]

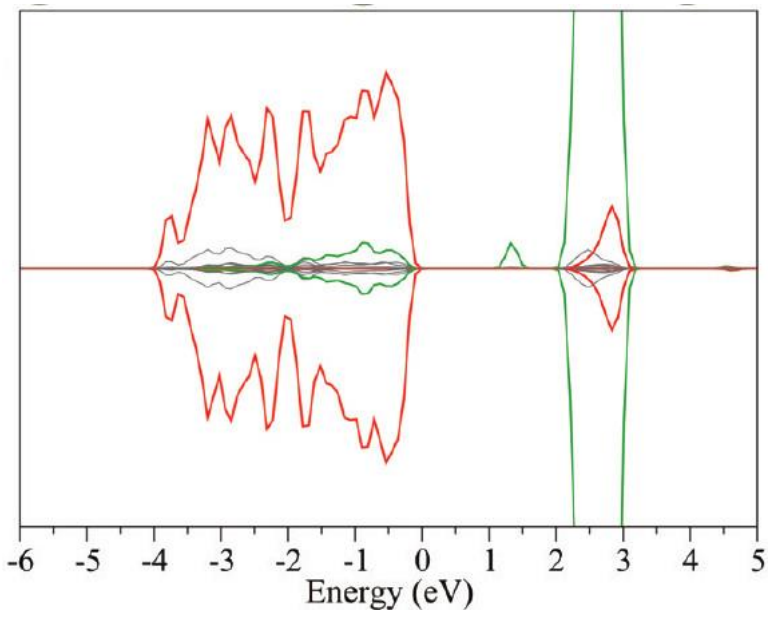

Figure 1. 8. The density of states (total DOS) of an oxygen vacancy in CeO2. The Ce4f states are represented by green lines, and the O2p states are represented by red lines. All other states are in gray. Reproduced from Ref. [49] with permission from American Chemical Society, copyright 2012.

1.3.2 Cerium Vacancy

The defect formation reaction for Ce vacancy would be like:

$$Ce_{Ce}^{\times} + 4O_O^{\times} \rightarrow V_{Ce}^{''''} + 4O_O^{\bullet} + Ce(\mathrm{s}) \qquad (1.13)$$

Since the formation of Ce vacancy removes four electrons from the lattice, holes are expected to localize on the O2p states. [49] The energy of formation of cerium vacancy (V_{Ce}) is double compared to the formation energy of V_O^0 under oxygen rich condition. [50] The V_{Ce} gives four - hole states on its adjacent O sites. It is found that after structural relaxation the O atoms without localized hole states move away from V_{Ce}, whereas the O atoms with localized hole states move toward the V_{Ce} site. [47] The cerium vacancy has been proposed as a possible source of ferromagnetic behavior in CeO_2. [51,52] The Figure 1.9 shows the EDOS for a Ce vacancy. This indicates that the cerium vacancy is semimettalic in nature. But, it was also found that an onsite

coulomb correction gives empty O2p states within the band gap. This indicates that the metallic solution is a result of failure of self-interaction error (SIE) correction. [53–57]

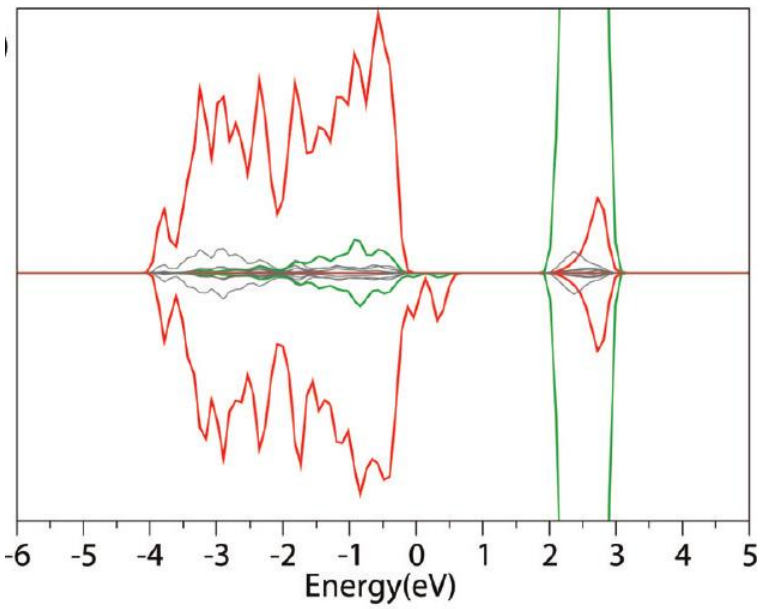

Figure 1. 9. Density of states (total DOS) for a Ce vacancy. The Ce4f states are represented by green lines, and the O2p states are represented by red lines. All other states are in gray. Reproduced from [49] with permission from American Chemical Society, copyright 2012.

1.3.3 Oxygen Interstitial

One possibility is that an oxygen interstitial would form localized holes on the interstitial ion and the neighboring oxygen ions

$$O_O^{\times} + \frac{1}{2}O_2(\mathrm{g}) \rightarrow \mathrm{O}_O^{\bullet} + O_i' \tag{1.14}$$

It is reported that the interstitial oxygen ions are unstable in the fluorite structure, thus leading them to relax into a position close to lattice oxygen ion to form a peroxide ion. [47,49]

$$O_O^{\times} + \frac{1}{2}O_2(\mathrm{g}) \rightarrow (\mathrm{O}_2)_O^{\times} \tag{1.15}$$

The EDOS for the oxygen interstitial in ceria (After Keating et al) is shown in Figure 1.10. The peaks in the EDOS between -6 and 0 eV correspond to the peroxide ion (possible occupation of a σ, two π, and two π* orbitals). However, Zacherle et al. [50] showed that the energy cost for the

doubly charged oxygen interstitial in a configuration similar to peroxide ion is greater than the one corresponding to oxygen interstitial in the octahedral position. In the case of neutral interstitial, they found a configuration where the interstitial is displaced from the octahedral site, but cannot be classified as a peroxide configuration.

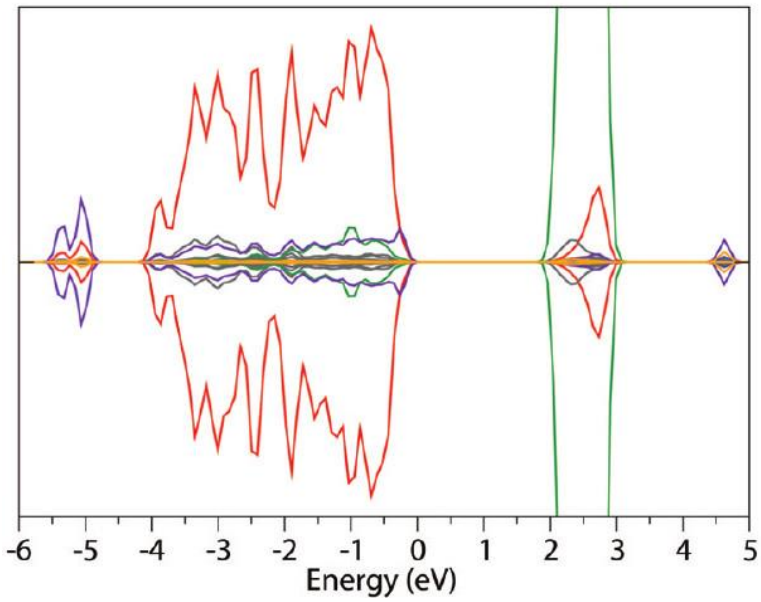

Figure 1. 10. Density of states (total DOS) for oxygen interstitial in CeO_2. The Ce4f states are represented by green lines, and the O2p states are represented by red lines. All other states are in gray. Reproduced from [49] with permission from American Chemical Society, copyright 2012.

1.3.4 Cerium Interstitial

Since a cerium interstitial introduces four extra electrons to the system; there are two ways for the excess electrons to localize: either reduce the four Ce neighbors

$$4Ce_{Ce}^{\times} + Ce(\mathrm{s}) \rightarrow 4Ce_{Ce}' + Ce_i^{\bullet\bullet\bullet\bullet} \tag{1.16}$$

or the displaced Ce atom provides three electrons to the neighboring cerium atoms with one electron remaining on the interstitial Ce (I_{Ce}). So that three of the neighbor Ce atoms become Ce^{3+} and the other remains Ce^{4+}.

$$3Ce_{Ce}^{\times} + Ce(\mathrm{s}) \rightarrow 3Ce_{Ce}' + Ce_i^{\bullet\bullet\bullet} \tag{1.17}$$

The local structure relaxation is achieved by moving Ce atoms from their normal positions so that Ce^{4+} ions move farther from their original positions compared to Ce^{3+}. The defect peaks in the EDOS (Figure 1.11) are made up of occupied Ce 4f states.

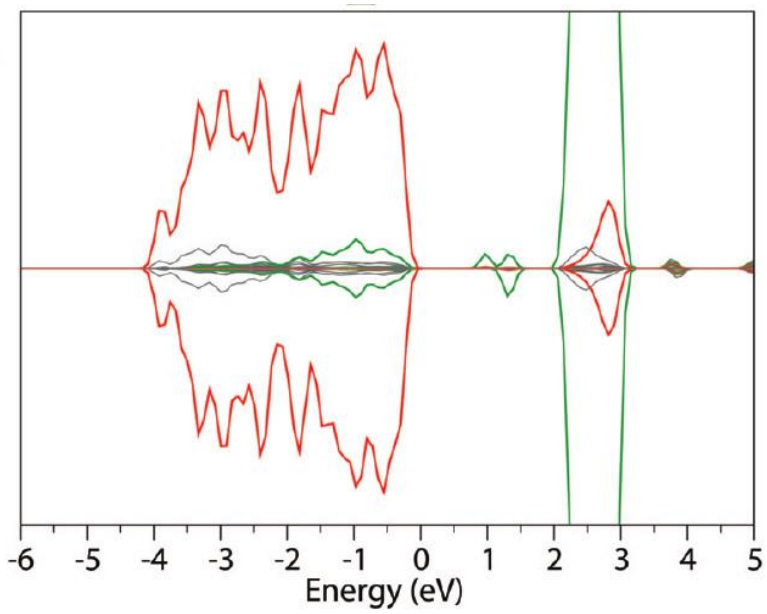

Figure 1. 11 Density of states (total DOS) of Ce interstitial in CeO_2. The Ce4f states are represented by green lines, and the O2p states are represented by red lines. All other states are in gray. Reproduced from [49] with permission from American Chemical Society, copyright 2012.

1.3.5 Frenkel, anti-Frenkel and Schottky Defects

The Kröger -Vink notation for the Frenkel, anti-Frenkel and Schottky defects are as follows

$$Ce_{Ce}^{\times} \rightleftharpoons V_{Ce}^{''''} + Ce_i^{\bullet\bullet\bullet\bullet} \tag{1.18}$$

$$O_O^{\times} \rightleftharpoons V_O^{\bullet\bullet} + O_i'' \tag{1.19}$$

$$Ce_{Ce}^{\times} + 2O_O^{\times} \rightleftharpoons V_{Ce}^{''''} + 2V_O^{\bullet\bullet} \tag{1.20}$$

The anti-Frenkel (a-Fr) defect is a result of moving an oxygen atom from its lattice position to an interstitial position so that a vacancy (V_O) and an interstitial (I_O) are produced. The EDOS for the a-Fr and Schottky defects are shown in Figure 1.12 and Figure 1.13 respectively. It is found that the EDOS of the pure bulk is not affected by the presence of Schottky defect. [58]

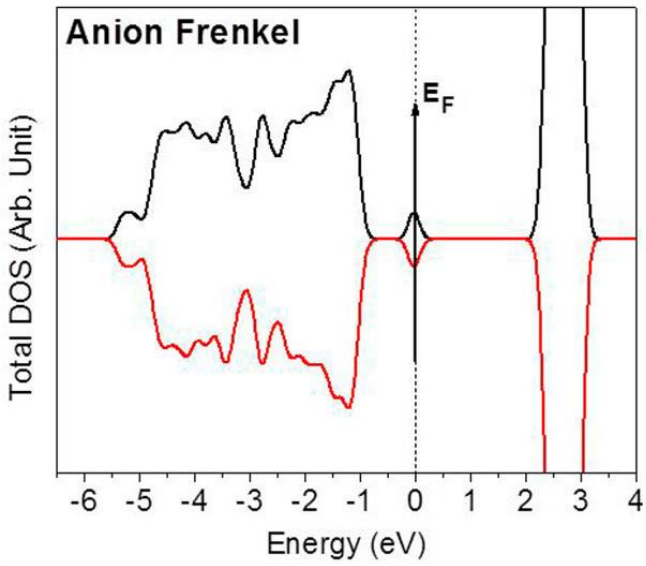

Figure 1. 12. Density of states of an anti Frenkel defect; the Fermi level is shown by the arrow. Reproduced from [47] with permission from American Chemical Society, copyright 2014.

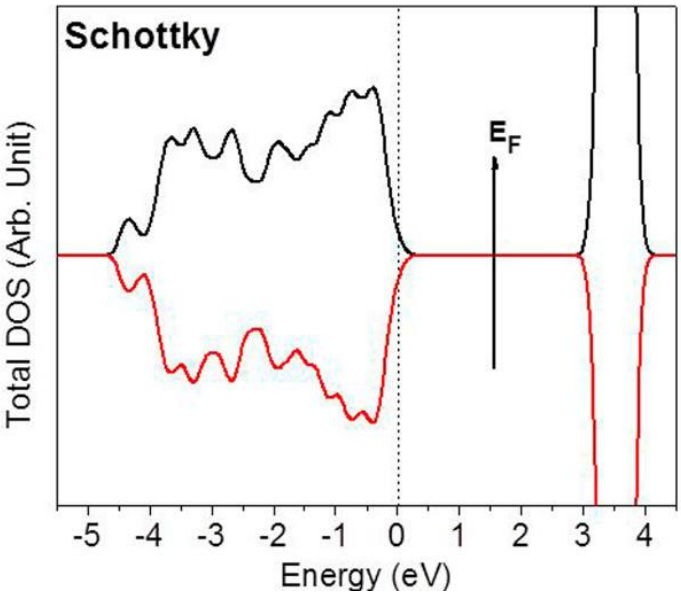

Figure 1. 13. Density of states of Schottky defect. Reproduced from [47] with permission from American Chemical Society, copyright 2014.

The relaxed structure of a-Fr shows that the lattice around Vo is more distorted than the structure near I_O. [47] The Schottky defect does not alter the structure. The Frenkel defect can form easier than the Schottky defect.

Another important thing regarding any discussion about the point defects in ceria is the presence of polarons. The polarons are formed as a result of self-trapping of electrons entering the Ce 4f states, whether by electron transfer processes at a surface or interface or through the defect formation. [59] When an oxygen vacancy is created, two electrons are left behind. Both of these electrons form the polarons, Ce_{Ce}'. But they remain bound to $V_O^{\bullet\bullet}$ as a neutral defect complex, $[V_O^{\bullet\bullet} - 2Ce_{Ce}']^x$. The implications of this association between the polarons and oxygen vacancies towards the F centers in ceria are the topic of discussion in Chapter 4.

1.4 Dominance of Oxygen Vacancies in CeO_2

Ceria can exist in varying stoichiometry (CeO_{2-x}) that depends on the temperatures and partial pressures of oxygen. The fluorite structure of CeO_2 is stable for incorporation of oxygen vacancies up to about 14%. [60] Ceria is unique in respect that it offers the opportunity to study the defect properties for small as well as large concentrations of defects. Because stoichiometric ceria can sustain deviations as small as $x=10^{-4}$-10^{-5} under oxidizing conditions in the temperature range 700˚-1000˚C. This is perfect for testing the ideal defect theory. Besides, the existence of large single-phase region at elevated temperatures is useful to study the transition between ideal defect behavior and defect interactions. [60,61]

Identification of defective sublattice is at the root of any defect structure determination. Historically, it is done by electrical and thermodynamic measurements. [62] Rudolph et al. [63] concluded from the oxygen partial pressure (pO_2) dependence of electrical conductivity that ceria is an n-type semiconductor. Greener et al. suggested that the defects are either quadruple ionized cerium interstitials or fully ionized oxygen vacancy pairs. [64] A defect model based on the cerium interstitials in multiple states of ionization was also proposed. [65] From Steele and Floyd, [66] it was concluded that the oxygen vacancies are the dominant defect in CeO_2. The seminal work by Tuller and Nowick lifted the ambiguity concerning the identity of the dominant

ionic defect in CeO_2. [62] They established a model that includes the single and double ionized oxygen vacancies. The double ionized vacancies were shown to be dominant at small x with a transition occurring toward single ionized vacancies at larger deviations from the stoichiometry.

The advances in theoretical methods and computational technology accelerated the computational studies of surface chemistry of ceria. As illustrated in the former sections, the functional properties of ceria arise as a result of the presence of oxygen vacancies. For instance, the near-stoichiometric CeO_2 is a poor ionic conductor (with conductivity $3.13\times10^{-3} S\ cm^{-1}$) due to low concentration of vacancies. [67] Studies have shown that the ionic conductivity can be increased by creating oxygen vacancies, which act as a path for ionic diffusion. [68–74] The calculations of formation energy for various defects in CeO_2 using different approaches (wave function based techniques and density functional theory) showed that the defects with the lowest formation energy are the oxygen vacancies under oxygen-poor conditions. [49,75,76] But studies do differ in the case of formation of oxygen interstitials. According to Keating et al. under oxygen-rich conditions the oxygen interstitials, which form peroxide ions, will be favorable. But the calculation from Zacherle says that the oxygen interstitials cannot be classified as a peroxide configuration because of a large oxygen-oxygen distance. Additionally, the polarons and the associates of polarons with oxygen vacancies are considered in CeO_2. [59,77] It is indicated that to best describe the properties of ceria description of polarons is necessary.

In summary, the oxygen vacancies are the dominant defect in CeO_2, and a complete understanding of the defect chemistry of ceria demands a comprehensive knowledge about all possible defect charge states and also the polarons and the associates of polarons with oxygen vacancies to be considered.

1.5 Unresolved Problems of Oxygen Vacancies in CeO_2

Despite the CeO_2 defect chemistry and its relation to the macroscopic properties have been studied for decades, little attention has been given to the defect induced local distortions and short range associates. Such an understanding is necessary to answer the questions regarding electro-mechanical and electrostrictive properties of doped ceria. [78–80] For example, the unusual properties of doped ceria, like the anomalously large electrostriction effect and anelastic

behavior in the case of Gd doped ceria are proposed to originate from anisotropic lattice distortions in the near neighbour shells of the cations and oxygen vacancies in the average fluorite structure. [81,82]

Since these features (i.e. local distortions and short-range order) are not periodic, they cannot be analyzed with the conventional x-ray powder diffraction. For this reason, we have to resort to techniques that are sensitive to local structure. Here we are presenting an approach combining X-ray fine structure absorption spectroscopy (XAFS) and Cathodoluminescence spectroscopy (CLS) to unravel the local structural distortion in doped and undoped ceria. These spectroscopic methods are suitable techniques of choice for revealing of the lattice distortions and the interaction of oxygen anions and vacancies with dopant or Ce^{3+} ions. Combining methods that are capable of probing the local distortions and the oxygen-vacancy related interactions can grant insights into the role of defect clustering and local distortions on reducibility of ceria. This will in turn help designing ceria-based materials with targeted properties for a variety of applications.

2 Review on Cathodoluminescence Studies

A thorough knowledge of the structure and disorder of oxygen sublattice in ionic materials is important to solve a number of technological problems like improving ionic conductivity in fuel cell electrolytes, enhancing the dielectric permittivity in ferroelectrics, employing oxynitride materials with perovskite structure or oxide ceramics in biomedical devices. [83–88] In all these cases, the anion order seems to have an influence on the physical properties, especially when the properties are sensitive to local distortions. Given this context, cathodoluminescence spectroscopy (CLS) has immense potential to solve fundamental problems related to functional materials. This is so because CLS is capable of providing mechanical stress information and also sensitive to oxygen vacancy concentration in oxide surfaces. [89]

Cathodoluminescence (CL) is the emission of photons (light) from solids upon interaction with an electron beam (of energy keV). The emitted photons could be in the ultraviolet, visible and infrared spectral ranges. Traditionally, CL has attracted researchers' attention because it offers contactless method with high spatial resolution for characterization of semiconductors. Since the emission mechanisms are similar for different types of excitation energy, it is expected that CL should give similar results as the photoluminescence (PL) and electroluminescence (EL). But in practice the observed differences are attributed to generation rate and volume of the excitation processes of electron-hole pairs. [90] An added advantage of CL is that it can provide more detailed depth resolved information by changing the electron beam energy. A detailed description of the CL technique is given in Chapter 3. Here I aim to give a discussion about how the technique has been used in the studies of materials and what are the insights derived from them.

2.1 Defect Study

One of the applications of CL mode is that it is used for imaging of defects. The defect contrast is possible in CL thanks to the enhanced non-radiative recombination at various types of irregularities in the crystal structure. For example, the non-radiative recombination in GaP is described by the contribution of point defects, dislocations, surface and the interface between

epitaxial film and substrate. [91] Most of the studies in the earlier times tried to understand the dislocation induced electronic levels in the gap and their effects on electrical and optical properties of the materials. Contrasting dislocations by CL resulted in the appearance of lines and dots. The dots were due to threading dislocations while the lines were due to misfit dislocations. CL is also used in the determination of a dislocation density in semiconductors. [92–94]

The advent of low temperature CL radically changed the way the spectroscopic technique had been used thus far. At the liquid helium temperature, the intensity of CL has increased tremendously and the width of the emission bands decreased. This lead to the improvement of signal to noise ratio and offered the possibility of seeing new spectral phenomena. [95,96] The observation of an emission line at 1.36 eV for epitaxially grown InP was due to an exciton bound to a defect. [97] The observation of deep level band, which was ascribed to a phosphorous vacancy complex, was made in the case of InP annealed at 750^{o}C. [98] These results showed the power of CL as a tool to study point defects and their complexes in the semiconductors.

CLS was used by Pezzoti et al. [99] to study the topographic distribution of oxygen vacancies and lattice strain on alumina/zirconia composites. They showed that the CLS is extremely efficient for simultaneous monitoring of the concentration of point defects (oxygen vacancies) and surface lattice strain with a spatial resolution in the order of nanometer. A depth resolved cathodoluminecsence spectroscopy (DRCLS) was employed to study the defects and their distribution in $SrTiO_3$ single crystals and epilayers. They found that in $SrTiO_3$ single crystals, the dominant defects are the oxygen vacancies that reside mainly at the free surface, while the Ti interstitials are located further inside the bulk. [100] The study demonstrated the potential of CLS as a tool to identify the nature of defects, their density and distribution as a function of thickness and stoichiometry. Fukatsu et al. [88] used CLS to explain the role of surface stoichiometry on the mechanisms leading to polymorphic transformation in yittria-stabilized zirconia. They characterized two kinds of Y_2O_3-stabilized ZrO_2 with respect to their tetragonal to monoclinic transformation and surface oxygen stoichiometry variations. Through the spectrally-resolved CL analysis, they confirmed the notion that the annihilation of oxygen vacancies in Y_2O_3-stabilized ZrO_2 is the main cause for the phase transformation.

2.2 Quantitative CL

The cathodoluminescence study, performed on pure zirconia and Y-doped zirconia powders by Bofelli et al. [89] showed the dependence of CL spectrum morphology on the dimension of the lattice cell. From this they have retrieved a phenomenological equation that relates monoclinic volume fraction and average lattice cell volume to CL intensity ratio (i.e., the ratio of sub-band areas). This CL (intensity ratio) parameter helped them to quantitatively assess polymorphic phase fractions by CL spectroscopy. The CL emission attributed to three types defects are: an intrinsic oxygen vacancy (F center) and two different extrinsic oxygen vacancy complexes capable to coordinate one or two Y^{3+} atoms (i.e., the F_A and F_{AA} centers, respectively) as shown in Figure 2.1.

The study showed a systematic decrease in the CL intensity with an increase in the dopant concentration. Based on this observation, they argued that the luminescent center could be related to the distortion of the oxygen sublattice. A phenomenological relationship between monoclinic volume fraction and the lattice cell average volume to a CL spectrum parameter has been obtained, thus showing the quantification ability of CL to map the polymorphic fractions in materials.

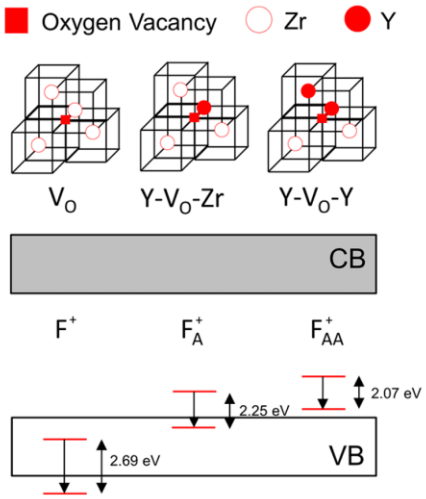

Figure 2. 1. Simplified schemes of different vacancy sites in Y-doped zirconia. Corresponding positions of their energy levels in the bandgap is also illustrated. Reproduced from [89] with permission from American Chemical Society, copyright 2014.

The existence of thermally induced residual stress leads to formation of point defects such as voids, oxygen vacancy centers etc. Leto et al. [101] showed that through the cathodoluminescence activity in the visible range, point defects can be used to directly characterize the internal stress in Cu-Ta/SiO_x carbon-doped model chip prepared on a Si substrate. They have used a piezospectroscopic (PS) approach for this purpose. The CL bands generated from optically active defects in dielectric silica reflects the structural features of silica network. Besides that, the CL spectrum contains information about the stress state of the silica clusters. It means that the observed defect population can be used as a stress sensor. According to Leto, the PS behavior of CL spectrum can be rationalized based on the following conditions: (1) the CL spectrum may change its morphology with the electron beam irradiation conditions, however in this case the spectrum was reasonably stable for given irradiation conditions; (2) the selected electron probe should be sufficiently large in order to probe a statistically meaningful (i.e., invariant) defect population at each selected location. So, the spectral shift of selected bands experiences high sensitivity to stress and, therefore, can be used as a probe for monitoring local stress states within the silica network. [101] Later, Pezzoti and Leto demonstrated the ability of CL as a stress sensor for silica glass to understand its fracture behavior. They exploited the optical activity of nonstoichiometric sites in the amorphous network. [102]

2.3 Time Resolved CL

By introduction of time resolved CL, it has become possible to calculate both the minority carrier lifetime and the surface recombination velocity. Assuming an exponential decay of the luminescence intensity L(t)

$$L(t) = L(0)\exp(-t/\tau) \tag{2.1}$$

the minority carrier lifetime can be obtained. Note that the measured values are effective lifetimes

$$\frac{1}{\tau_{eff}} = \frac{1}{\tau_{bulk}} + \frac{1}{\tau_{surf}} \tag{2.2}$$

Hastenrath and Kubalek [103] showed that the estimated value of surface recombination velocity was within the range of values of surface recombination velocity for GaAs. The CL decay measurements were also used for carrier lifetime mapping. [104]

2.4 New Directions

As described so far, the use of cathodoluminescence spectroscopy spans diverse fields. In mineralogy and petrology, it was used to identify geological samples by scrutinizing mineral specific luminescence. The luminescent properties were used to understand variations in the local composition, local dopant concentration, stress and strain, and point or extended defects in materials science. [105–107] Quite recently, CL has gained attention from nanophotonics community pertaining to studies of plasmonic systems. [108] A combination of spectral and angular data measured with a nanoscale probe makes CL into a very powerful tool to study the dispersion, radiation profiles, and spatial modal distributions of optical antennas, [109–111] plasmonic nanocavities, [112,113] waveguides and periodic crystals. [114–116] Brenny et al. [108] used the angle-resolved cathodoluminescence to separate coherent and incoherent contributions to CL from bulk materials like Si, GaAs, Al, Ag, and Cu. This method of separation of different radiative processes in the CL emission is quite useful for material characterization and to study electron-matter interactions as well as light-matter interactions in metals and semiconductors. For instance, the coherent emission of an antenna from the luminescence of the substrate can be distinguished using this method of separation.

The study of single photon sources is very important in the context of next generation technologies like quantum computing and quantum cryptography. [117] The reliable single photon sources (SPS) have been demonstrated on nitrogen vacancy centers in diamond, [118,119] Cs atoms in an optical cavity, [120] and quantum dots (GaN in a AlN matrix or CdSe nanocrystals). [119] To probe these SPS, the conventional optical techniques are not suitable because these techniques have a diffraction limit well above the size of the objects being investigated. In this situation, CL is an ideal candidate for such experiments. Tizei and Kociak [121] demonstrated the single photon state generation and characterization in electron microscope using CL. The single photon sources are called so, because after excitation of an SPS, the probability of detecting two simultaneous photon emissions is zero, independently of

the exciting probe statistics. This quantum effect is called photon antibunching. The SPS are quantified by the measurement of the second order correlation function $g^{(2)}(\tau)$.

$$g^{(2)}(\tau) = \frac{\langle I(t)\, \mathrm{I}(\mathrm{t}+\tau)\rangle}{\langle I(t)\rangle \langle \mathrm{I}(\mathrm{t}+\tau)\rangle} \tag{2.3}$$

This function provides intensity correlations [I (t)] of a given light field at different time delays, tau. This can be measured using a Hanbury Brown-Twiss (HBT) intensity interferometer. [122] For classical light $g^{(2)}(\tau) \geq 1$ for any τ. But, for a single photon beam $g^{(2)}(0) = 0$. [118] With the ability of CL to dodge the limitations of other optical microscopy methods, Tizei and Kociak [121] proved that the nitrogen vacancy centers in diamond particles can trigger single photon emission. In a similar way Bourrellier et al. [123] combining CL in a STEM microscope with HBT, identified a new ultra violet single photon emitter in hexagonal boron nitride (h-BN). They attributed it to a point defect ie. carbon substitutional at nitrogen sites in h-BN.

Most of the applications of semiconductors, from LEDs to quantum optics depend on the understanding of structures as small as an atom and separated by few nanometers. CL in the scanning transmission electron microscopy (STEM), has proposed to meet this need of a characterization technique capable of lifetime measurements at the nanoscale and providing structural and morphological information. According to Sophie Meuret et al. [124] the measurement of individual life times of quantum emitters is possible by monitoring the extremely localized cathodoluminecsence signals. The CL signals are further analyzed through intensity interferometry to measure the lifetime of the emitters. Later Meuret et al. [125] used an extension of the method to determine cathodoluminecsence emissiom statistics of InGaN quantum wells embedded in GaN. They found that the light emission rate varies strongly from electron to electron. Another advancement in the field of CL comes from exploiting the momentum distribution, i.e., the direction in which light is emitted from a material. This can be used to obtain useful information about optical properties of nanostructures and electron-mater interaction. [126] Examples include, local probing of the band structure of periodic systems, [115,116,127] plasmon outcoupling [128], and separation of coherent and incoherent CL processes in bulk materials. [108]

With the advances in electron microscopy, photon detectors, and imaging capabilities cathodoluminescence is now capable of using all the information contained in the light emerging

from a material as a result of electron beam excitation. The accessibility domain of CL technique consists of wavelength and time domain, angular distribution, polarization, spatial distribution and correlation to structural and electronic properties of the emitted light. Wavelength expansion into the infrared and the soft x-ray limit will usher in new range of physical phenomena and materials that can be studied by CL. [126]

2.4.1 Angular CL

The momentum distribution of cathodoluminescence emission can be used to understand the optical properties of nanostructures. This includes plasmon out-coupling, [128] multipolar decomposition of nanoparticle scattering, [129–133] local band structure probing of periodic systems etc. There are different methods to gain momentum information and carry out angle resolved CL imaging.

In one method, [115,116] a pinhole is scanned transversely through the beam coming from the paraboloid collection system. Since the light is send to a spectrometer after the pinhole, this method can determine angle response with a high spectral resolution. But, it takes longer time to acquire the full angular profile. Another approach is to project the CL emission coming from the paraboloid onto a 2D imaging array, so that a fast angle resolved imaging is possible (Figure 2.2). [133,134] Both approaches give raw data which have to be converted to represent the angular profile in the desired form. The angular profile is represented by displaying emission intensity per steradian in spherical coordinates (as a function of θ and ϕ)(Figure 2.2).

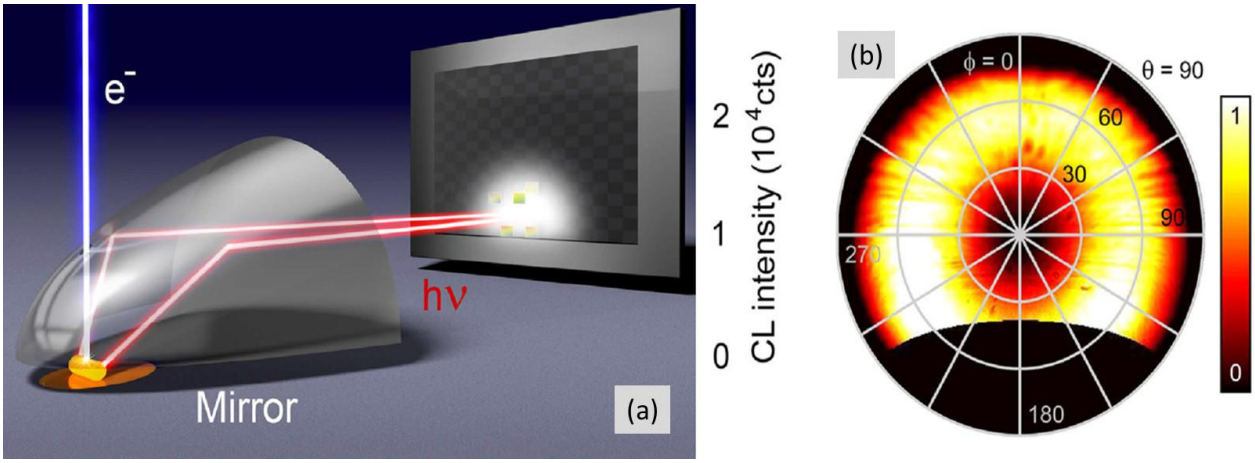

Figure 2. 2. a) Schematic representation of angle resolved Cl detection system. b) Angular pattern extracted from raw data. Reproduced from [126] with permission from AIP Publishing, copyright 2017.

2.4.2 Advanced Time Resolved CL

The relevance of time dynamics and statistics of light emission studies is that it can reveal information on the quality, photonic environment and quantum mechanical properties of a material. [ref] With CL it is possible to study such dynamics with high spatial resolution. It has shown that Hanbury Brown and Twiss (HBT) interferometer can be used to study the emission statistics. Using this method $g^{(2)}$ correlation function which describes the emission statistics and in turn photon (anti)bunching can be measured. [ref Coenen 66-70] Moreover, the life time of emission can be extracted from the line shapes in the $g^{(2)}$ function. [124] This approach has the advantage that it can be used in a regular electron microscope with a continuous beam. On the disadvantage side, $g^{(2)}$ approach is a time consuming method and hence it could damage the sample under study.

The more general approach to the lifetime measurement is the use of ultrafast pulsed electron microscope. Two approaches exist there to create an ultrafast electron source (1) electrostatic blanking and (2) photon electron excitation with pulsed laser system. [135,136] In the electrostatic blanking, the application of a fast electric field deflects the electron beam from its normal trajectory. It has been reported that using the electron beam blanking a pulse duration as short as 90 ps has been achieved in the CL experiments. [137] Another method of the beam blanking is using a RF/microwave cavity. [138] [74] The photoelectron generation process in the

CL microscopy has been realized by irradiating the electron gun with an ultrafast laser pulse. It's important to note that along with an ultrafast electron source, ultrafast light detectors are also needed for these measurements. The time resolved CL imaging has been used for the investigation of effects of nanostructuring, [139] strain, [140] and defects [141] on the carrier dynamics.

3 Experimental Methods

As described in chapter 1, the functional properties of CeO_2 are a result of the oxygen vacancies (V_O) created in the material. Several methods can be employed to create and control the defect concentration in CeO_2. Since CeO_2 exchanges oxygen with the atmosphere, by Ce^{3+}/Ce^{4+} transformation, the concentration of oxygen vacancies can be manipulated with the processing atmosphere. Moreover, upon doping with aliovalent cations (for example La^{3+}) the concentration of Ce^{3+} is suppressed, while the formation of the oxygen vacancies accounts for electro-neutrality.

3.1 Sample Preparation

3.1.1 Sintering in Different Atmosphere

The anti-Frenkel (AF) defects in CeO_2 can be created by exposing them to atmosphere with low partial pressure of oxygen (pO_2). The defect equilibrium in Kröger -Vink notation can be written as follows:

$$2Ce_{Ce}^{\times} + 4O_O^{\times} \rightleftharpoons 2Ce_{Ce}' + 3O_O^{\times} + V_O^{\bullet\bullet} + \frac{1}{2}O_2(\mathrm{g}) \tag{3.1}$$

Assuming no interaction between defects, the equilibrium constant of reaction (3.1) is:

$$K_n = [\mathrm{V_O^{\bullet\bullet}}][\mathrm{Ce'_{Ce}}]^2 \, pO_2^{1/2} \tag{3.2}$$

Where pO_2 is the oxygen partial pressure. Therefore, V_O can be readily changed by changing pO_2.

The carrier electron concentration $[Ce'_{Ce}]$ for CeO_2 can be calculated as follows:

For $[Ce'_{Ce}] = 2[V_O^{\bullet\bullet}]$ equation (3.2) becomes

$$[Ce'_{Ce}]^3 = 2K_n \, pO_2^{-1/2} \tag{3.3}$$

$$[Ce'_{Ce}] = (2K_n)^{1/3} \, pO_2^{-1/6} \tag{3.4}$$

The carrier concentration for doped ceria is calculated by the following equation; in this case $[V_O^{\bullet\bullet}]$ can be assumed to be constant and determined by the impurity cations in the lattice, [142]

From equation (3.2)

$$[Ce'_{Ce}]^2 = (K_n / [V_O^{\bullet\bullet}])\, pO_2^{-1/2} \tag{3.5}$$

$$[Ce'_{Ce}] = (K_n / [V_O^{\bullet\bullet}])^{1/2}\, pO_2^{-1/4} \tag{3.6}$$

Thermodynamic studies of this defect reaction using thermogravimetry, coulometric titration and electrical conductivity have been carried out. The dependence of x to $pO_2^{-1/n}$ can be seen in different intervals of pO_2. For small values of x, n value of 5 has been reported. It is found that n increases rapidly with x, up to approximately n=30. [143–145] n value of 6 in equation (3.1) was predicted by a theory of non-interacting defects. It is often difficult to find this dependence because of stoichiometric changes caused by impurities. [146]

Figure 3.1 shows the oxygen deficiency x as a function of $pO_2^{1/n}$ from literature. Extensive studies have been performed (Figure 3.2) to measure the relationship between the stoichiometry and pO_2 for pure and doped ceria. [147–151] The explanations are based on different types of defects following the law of mass action and interactions between defects.

Additionally, the free energy for formation of a given non-stoichiometric ceria, ΔG_{O_2} is used to extract parameters ΔH_{O_2} (partial free enthalpy of formation) and ΔS_{O_2} (the partial entropy of formation). This is done as follows:

$$\Delta G_{O_2} = RT \ln pO_2 \tag{3.7}$$

Where pO_2 is the oxygen partial pressure. Since

$$\Delta G_{O_2} = \Delta H_{O_2} - T\Delta S_{O_2} \tag{3.8}$$

$$\ln pO_2 = \frac{\Delta H_{O_2}}{RT} - \frac{\Delta S_{O_2}}{R} \tag{3.9}$$

From this equation it is clear that both ΔH_{O_2} and ΔS_{O_2} can be derived from plots such as depicted in Figure 3.1 and 3.2.

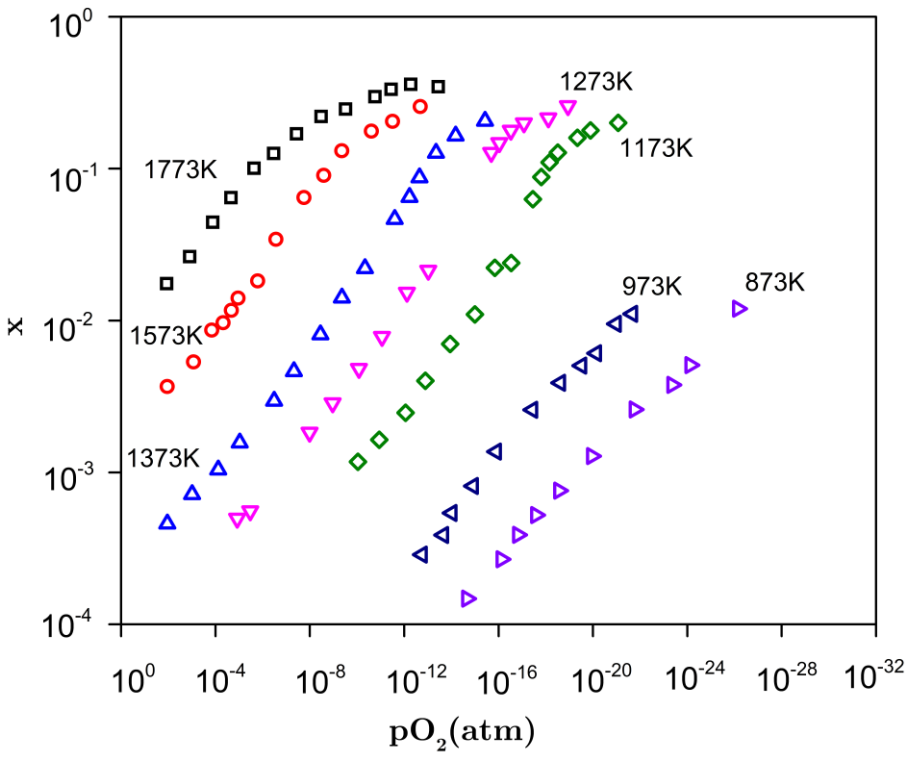

Figure 3. 1. Dependence of oxygen partial pressure (pO_2) and oxygen deficiency (x) from literature. Adapted from [152] with permission from Elsevier copyright 2000.

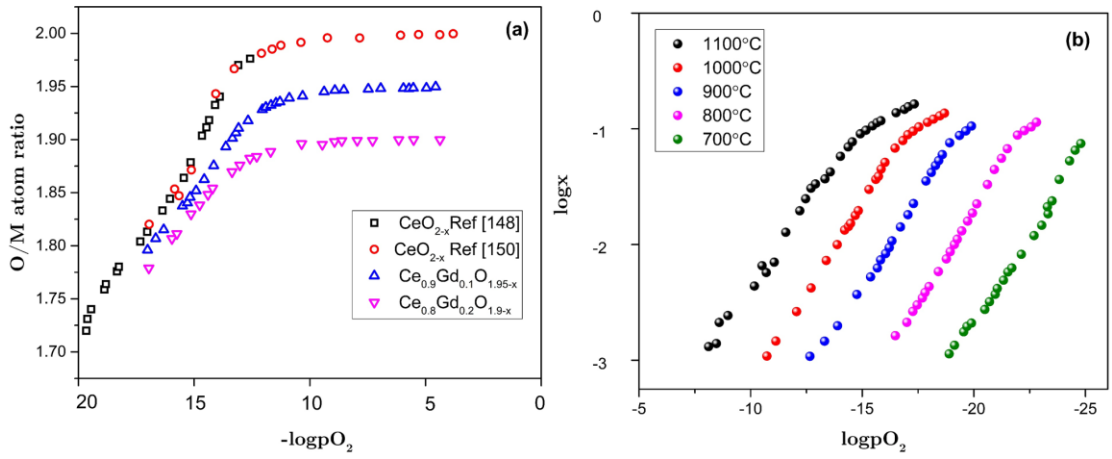

Figure 3. 2. a) Relationship between oxygen to metal atom ratio (O/M) and pO_2 at 1000°C for CeO_2, $Ce_{0.9}Gd_{0.1}O_{1.95-x}$ b) log x-log pO_2 relationship of $Ce_{0.9}Gd_{0.1}O_{1.95-x}$ at various temperatures. Adapted from [152] with permission from Elsevier copyright 2000.

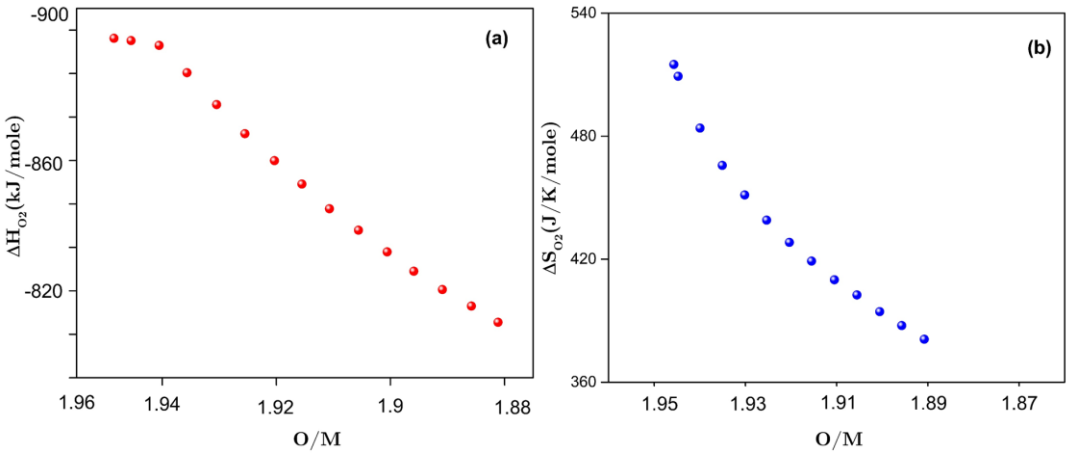

Figure 3. 3. Variation of a) ΔH_{O_2} and b) ΔS_{O_2} as a function of O/M ratio (vacancy concentration). Adapted from [152] with permission from Elsevier copyright 2000.

It was found that ΔH_{O_2} is independent of temperature and fairly depends on the vacancy concentration (Figure 3.3). Some studies based on ΔS_{O_2} values pointed out that highly doped ceria is reduced more readily than low doped and undoped ceria. However, the most of the reported data do not support this conclusion. [144,151,153]

The phase equilibria studies on CeO_2 as a function of temperature and stoichiometry have been carried out. [154–159] The observed lattice parameter expansion was explained by Vegard's law. It was proposed that non-stoichiometry can be treated as the presence of Ce_2O_3 in CeO_2 (i.e., solid solution of Ce_2O_3 in CeO_2). In that case the lattice parameter should follow Vegard's law. [160] But, Ray et al. [157] showed that Vegard's rule is validated even in the case of a two phase system (α+δ-phase composition region in the phase diagram in Figure 3.4) ruled out the assumption that CeO_{2-x} can be treated as a simple solid solution of Ce_2O_3 in CeO_2. The expansion of ceria lattice upon reduction is attributed to the presence of Ce^{3+} (1.143 Å) ions, which are bigger than Ce^{4+} (0.97 Å) ions (Shannon ionic radii are written).

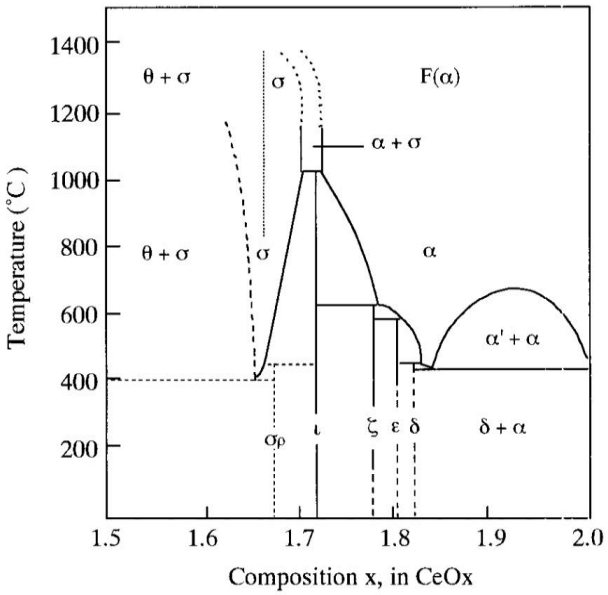

Figure 3. 4. Phase diagram of CeO_{2-x}. Reproduced from [161] with permission from Springer Nature copyright 1991.

Based on these facts in order to create varying vacancy concentration in pure CeO_2, the material is processed at high temperature in different atmospheres. The heating regime is presented in Figure 3.5. The starting material was CeO_2 form Sigma Aldrich® having particle size smaller than 50nm and purity 99.95% (with respect to other rare earth elements). Later, we confirmed the presence of Sm (0.4mg/kg) by inductively coupled plasma mass spectrometry (ICPMS). The material was pressed into a pellet of diameter 8mm. These pellets were heat treated in different atmospheres.

To have a varying partial pressure of oxygen (pO_2) we have used oxygen, air and nitrogen with pO_2 decreasing in that same order. A series of samples were sintered at 1450°C for eight hours in a tube furnace, in the different atmospheres. The rate of heating and cooling was kept constant at 8°C/min. After sintering the pellets were turned from pale yellow color to pink beige, indicating Ce^{4+} to Ce^{3+} reduction. After polishing the sintered pellets were characterized by SEM to understand the microstructure.

Irrespective of the sintering atmosphere the grain size and porosity of the material were the same. (see Chapter 4 Figure 4.1 and 4.2) Later, another series of samples are prepared by quenching them to room temperature after treatment at temperatures 600°C, 800°C, 1000°C and 1200°C for

ten hours. The quenching procedure was carried out for all different atmospheres as mentioned earlier. Since pO_2 was varied, we expected an oxygen vacancy concentration in the increasing order $V_O^{Oxygen} < V_O^{Air} < V_O^{Nitrogen}$. The quenching process resulted in creation of materials with frozen state of defects. Just as before, quenched samples were also characterized for their microstructure and made sure that all the samples (both sintered and quenched) are comparable in terms of grain size and porosity, thus enabling us to characterize them with cathodoluminescence spectroscopy.

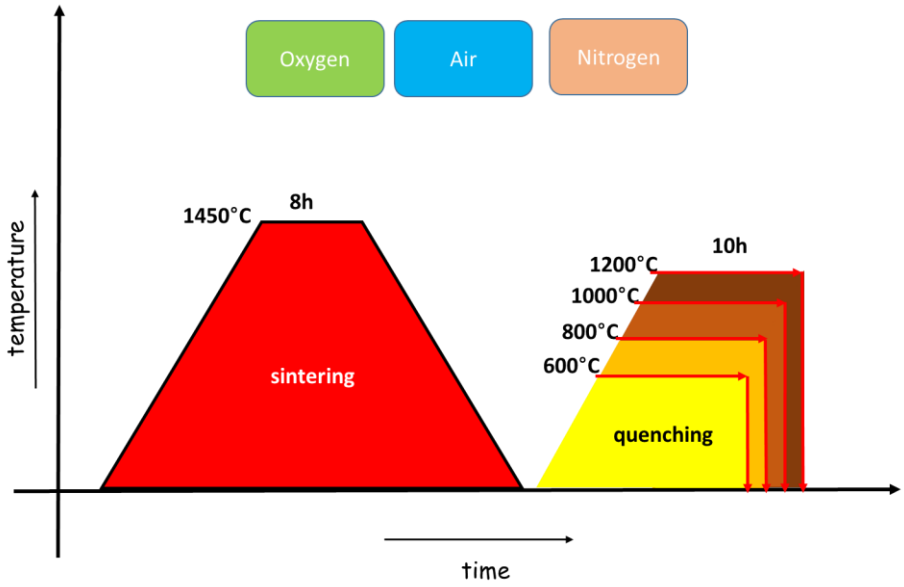

Figure 3. 5. Scheme of the heat treatment of CeO_2 in oxygen, air and nitrogen atmosphere.

3.1.2 Co-precipitation Method

Co-precipitation involves the precipitation of a new phase from a supersaturated solution. [162] It is a simple and rapid method for the synthesis of materials where control over the composition, and particle size can be achieved easily. From an environmental point of view, this method is desirable as it involves no organic solvent.

The major steps in the process of precipitation are liquid mixing, nucleation and crystal growth of primary particles, and aggregation of the primary particles. [163] Nucleation is a complex process in which cluster formation is the first step. These clusters are capable of spontaneous growth. They grow further until a critical size is reached. If the cluster size is smaller than this

critical size, they incline to dissolve. Otherwise the cluster will continue to grow. It is necessary to reach supersaturation for spontaneous crystallization to happen. [164] The nucleation rate can be described as

$$\frac{dN}{dt} = \beta \exp\left(\frac{-A}{\ln^2 s}\right) \tag{3.10}$$

Where A is the interfacial energy parameter given as

$$A = \frac{-16\pi\sigma^3 v^2}{3(kT)^3} \tag{3.11}$$

here β is a pre exponential term, σ is the solid/fluid interfacial energy, v is the solid molecular volume, T is the temperature and s is the super saturation defined as $s = \frac{c}{c_{eq}}$. [165,166]

Nucleation depends on both concentration and temperature. It is evident that nucleation is very slow below a critical supersaturation concentration. Above that the nucleation becomes exponential. [163]

The growth rate for the crystal is given as

$$k_g = a\left(c - c_{eq}\right)^n \tag{3.12}$$

where a is the growth rate constant, c concentration, c_{eq} solubility concentration. The exponent n lies between 1-2 and usually closer to 1. Since nucleation has an exponential increase with supersaturation concentration and the crystal growth is approximately linear, at high supersaturation levels the nucleation is promoted rather than the crystal growth. Hence, it favors the precipitation of highly dispersed materials. On the other hand, a dilute solution leads to the precipitation of fewer but larger crystals.

The aggregation is a process of formation of micrometer sized secondary particles from clusters of nanoscale primary particles. These aggregates are held together by physical and chemical forces. Pores are considered as voids between primary particles and porosity can be manipulated by changing the stacking. [163] The processes such as recrystallization, change in chemical or phase composition could happen during precipitation.

For co precipitation, precursors are chosen such that the counter ions would easily be decomposed to volatile products during the heat treatment. Commonly used precursors are nitrate and carbonate salts and ammonia or sodium carbonate are used as precipitating agent. Most of the time, it is carried out in aqueous media rather than organic solvents. The displacement of counter ions like carbonate and nitrate by hydroxide is facilitated by high pH and temperature. Also it is found that pH affects the final properties of the precipitates. The primary properties of the precipitates such as crystallite size, phase, and surface area are dictated by the precipitation temperature. The nucleation rate is sensitive to temperature so that rapid precipitation occurs at elevated temperature. It is also possible that at high temperature the formed crystallites would be larger compared to room temperature. [163] High concentration of metal ions in the precipitation media leads to faster precipitation, smaller particle size and higher surface area owing to the increased nucleation rate.

Doping with trivalent rare earth elements is a strategy to create and control oxygen vacancies in CeO_2. Through the control over the doping concentration we can precisely manipulate the V_O concentration. We used La as the dopant, since there is no worry of a possible mixed valence in the case of La, as it stays in the very stable 3+ oxidation state. Besides, the ionic radius of La^{3+} (1.16Å) is comparable to Ce^{3+} (1.14Å). The previous studies showed that the La-doping can maintain the fluorite structure up to the x value = 0.61(±0.11) for the stoichiometry of $Ce_{1-x}La_xO_{2-x/2}$. [Ref 49,50 thesis title] Thus, it will be a good model system to the undoped ceria and its defect structures. The observed CL intensity quenching in the case of undoped ceria (see Chapter 4) could be replicated using La-doped CeO_2 (see chapter 5). High purity $Ce(NO_3)_3.6H_2O$ (99.99%) and $La(NO_3)_3.6H_2O$ (99.99%) were used as precursors for the synthesis of $Ce_{1-x}La_xO_{2-x/2}$. After dissolving in de-ionized water and stirring for 30 minutes both precursors were mixed together and stirred for another 30 minutes. The precipitation was carried out using drop wise addition of ammonia solution. The precipitate was dried in a hot air oven for 8 hours at 100˚C. Then the ground precipitate was calcined at 550°C for 2 hours. The rate of heating and cooling was fixed at 5°C/min. Later, these samples were pelletized and sintered at a heating and cooling rate 8°C/min in oxygen atmosphere for 10 hours at 1450°C.

3.2 Structural Characterization

For the better understanding of the materials and its properties, structural characterization is of fundamental importance. I used scanning electron microscopy (SEM) for the morphological and stoichiometric characterization of the materials. The crystal structure of the material was identified using an x-ray diffraction (XRD).

3.2.1 Imaging using Scanning Electron Microscope (SEM)

A fundamental limitation of optical microscopy caused by the diffraction limit leads to discovery of the SEM. In SEM, the wave nature of electrons is exploited and the interaction between electrons and matter gives rise to useful signals such as secondary electrons, backscattered electrons and characteristic x-rays etc. These signals are quite useful to understand several characteristics of the sample for example, morphology and composition. The versatility of SEM is that it is a microscope as well as an electron probe x-ray microanalysis tool. Moreover, new functionalities are attached to SEM to meet the needs of the semiconductor industry. For instance, cathodoluminescence system in SEM helps to study optical properties of materials. The different kinds of signals coming out of a sample as a result of the primary electron beam interaction are portrayed in Figure 3.6.

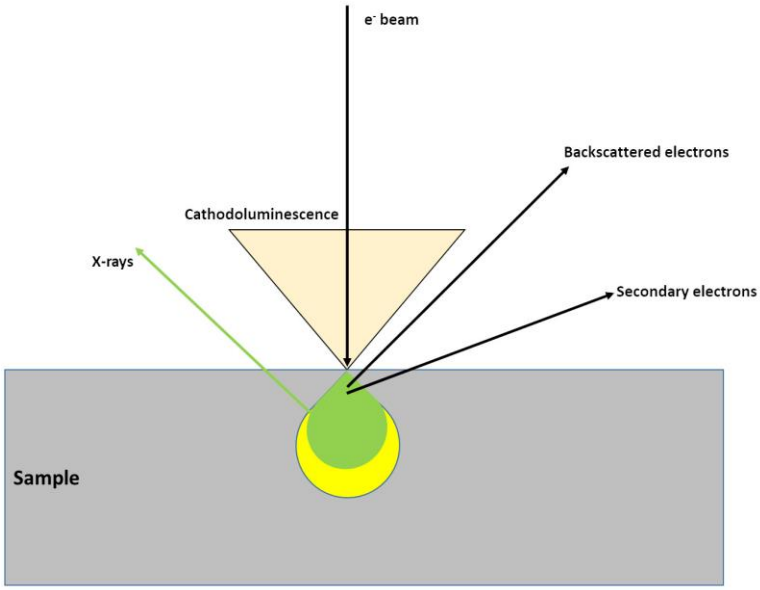

Figure 3. 6. Various signals from specimen upon interaction with primary electrons. The secondary electrons and backscattered electrons are used for imaging, while the characteristic x-rays are used for a compositional analysis.

Imaging is performed using secondary electrons and backscattered electrons. The secondary electrons (SE) that are generated from a very small depth (< 2nm) are used in the image construction and are result of inelastic scattering of the primary electrons with the specimen. Secondary electron (SE) images show the surface structure (morphology) of the sample under investigation. Surface features tilted towards the detector appear brighter because SE from these sites have greater probability of reaching the detector. This is also the reason why SE images have a three dimensional appearance.

The backscattered electrons (BSE) are a result of elastic scattering and have energies closer to primary electrons. So BSE and SE can be distinguished from their kinetic energies. The depth, from which BSE come, extends from tens or hundreds of nanometers depending on the primary beam energy. A number of BSE is proportional to the atomic number (Z), hence different elements in the samples can be identified along with information on crystallography and morphology.

3.2.2 Chemical Analysis using Energy Dispersive X-Ray Spectroscopy (EDS)

As shown in Figure 3.6, the characteristic x-rays are generated from the sample upon interaction with the primary electrons. These x-rays originate from microns deep within the sample and are used for the identification of elements present in the specimen and quantitative analysis of the concentration ratios of elements. The EDS detector is a semiconductor diode. When a characteristic x-ray penetrates through the detector it generates electron-hole pairs and results in electrical conduction. The number of electron-hole pairs created is proportional to the photon energy and hence the characteristic x-rays can be distinguished. The quantification of the elemental ratios in a sample is done by measuring the area under the peak of characteristic x-rays and subtracting the contribution from background.

SEM had a pivotal role in the studies presented here as a characterization tool and a spectroscopic tool to study the optical properties. The capability of SEM in this regard (Cathodoluminecsence) will be discussed in the section 3.3.1.

3.2.3 Structural Analysis using X-Ray Diffraction (XRD)

The crystal structure of a sample is deduced from XRD. XRD is a powerful characterization technique since it allows the identification of different phases of the same material, for example rutile and anatase forms of TiO_2. When x-rays impinge on materials, it will be diffracted and the diffraction intensity decreases with increasing angle of incidence. Even for powdered samples the diffracted x-rays will interfere constructively when the optical path difference between first and second x-rays (Figure 3.7) is an integral multiple of x-ray wavelength. Therefore, x-rays are observed only in certain directions that are dictated by Bragg's law:

$$2d \sin\theta = n\lambda \tag{3.13}$$

Where λ is the x-ray wavelength, θ is the incident angle and d is the lattice spacing.

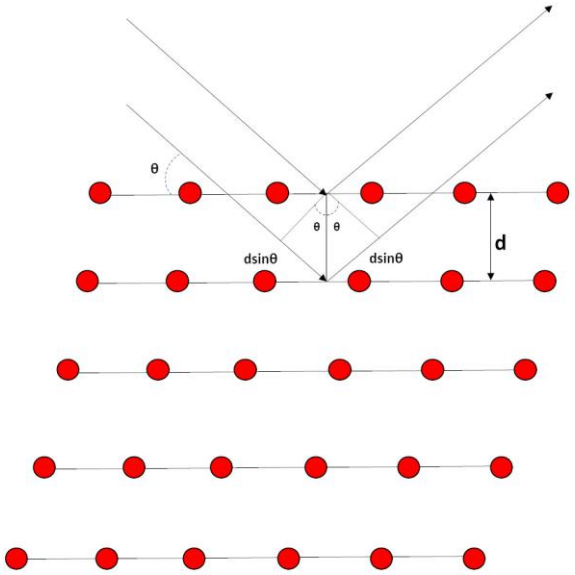

Figure 3. 7. Bragg's law. The diffracted x-rays show constructive interference when the path difference between them is equal to an integer number of wavelength (λ).

To have a detailed understanding of the crystal structure, a Rietveld analysis is performed. The refinement of the structure parameters provides information on a percentage of compounds in a sample, crystallite size, strain and crystalline to amorphous ratio in the sample. The Rietveld method is a profile fitting procedure and it produces precise peak positions, widths, heights and areas with statistically valid estimates. Experimental data are fitted empirically with a series of equations for both diffraction peaks and the background. The diffraction peak is fitted by a profile function, which is a mixture of Gaussian and Lorentzian shapes that are characteristic of diffraction data. The background function is usually a polynomial that helps to separate peak tail intensities from background. The Rietveld analysis produces a refined crystal structure model for all phases in the sample.

Thus, after the structural characterization and phase purity analysis the samples are studied using several spectroscopic techniques to unravel the defect structure. The stress is given to understand the correlation between local structure distortion and spectroscopic properties, an area of study often given little attention in literature.

3.3 Spectroscopic Investigation of Defects

As outlined in the introduction the defect structure of a material can be understood employing cathodoluminescence spectroscopy (CLS). Besides, other sophisticated spectroscopic techniques such as an X-ray absorption spectroscopy (XAS) can reveal the fundamental structure of defects in materials. Based on these structural information, CLS can be interpreted for their CL origin and more physical insight into CL behavior can be revealed. It is interesting to note that the impedance spectroscopy can be employed in this direction as it has the capability to show defect association in materials. Principles of these techniques are outlined in the following sections and their use in the study of CeO_2 defect structure will be explained.

3.3.1 Cathodoluminescence Spectroscopy

The history of cathodoluminescence dates back to the demonstration by Sir William Crookes in 1879, when he showed that calcium sulphide produces bright light when exposed to electrons in vacuum. The applications of the CL have been outlined in chapter 2. Here I intend to give a detailed description of the principle of cathodoluminescence and instrumentation. Also, advancement in the field will be discussed briefly in the end. The early works on CL were based on measurements of light properties such as energy and intensity. Starting from 2000s, developments in approaches and instrumentation for CL heralded exploitation of a wide range of photon properties including momentum, rest mass, polarization, spin, parity and quantum nature. [126]

Cathodoluminescence makes use of photons generated as a result of an interaction of electrons with materials (minerals, semiconductors and other luminescent solids). CL has been an attractive tool since it offers a contactless method for the characterization of materials with a high spatial resolution. To contrast with photon excitation, the electron beam excitation leads to emission by all the luminescence mechanisms present in the material. [90,92] Another advantage of CL is its ability to obtain depth resolved information. Also, it should be noted that the electron beam excitation generates way more electron-hole pairs than optical excitation.

When electron interacts with a solid it undergoes elastic and inelastic scattering. According to the Rutherford model, for the case of elastic scattering, the total relativistic Rutherford scattering cross section is given by,

$$\sigma = (5.21\times10^{-21})\left(\frac{Z}{E}\right)^2 \frac{4\pi}{\delta(\delta+1)}\left(\frac{E+m_0c^2}{E+2m_0c^2}\right)^2 \tag{3.14}$$

Where Z is the atomic number of the scattering atom, E is the energy of electrons in keV, and δ is a screening parameter:

$$\delta = (3.4\times10^{-3})\frac{Z^{0.67}}{E} \tag{3.15}$$

The probability for elastic scatting in the angular range 0 to θ can be derived from equation for σ. [167]

$$\cos\theta = 1-\frac{2\delta R}{1+\delta-R} \tag{3.16}$$

Where R is uniformly distributed random number $(0 \le R \le 1)$. The relativistic correction to the cross section is significant only for energies greater than 50keV.

The inelastic scattering is described by the Bethe expression as follows:

The rate of energy loss per distance S travelled in the solid

$$\frac{dE}{dS} = -2\pi e^4 N_A \frac{\rho Z}{EA}\ln\left(\frac{1.166E}{J}\right) \tag{3.17}$$

Where e is the electronic charge, N_A is Avogadro's number, ρ is the density, A is the atomic weight, E is the mean electron energy, and J is the mean ionization potential.

The average energy loss per interaction

$$J = (9.76\,\mathrm{Z} + 58.5\,\mathrm{Z}^{-0.19})10^{-3}(\mathrm{keV}) \tag{3.18}$$

The cathodoluminescence is a result of inelastic scattering process. The range of penetration of electron in a material is a function of beam energy E_b,

$$R_e = (k/\rho) E_b^{\alpha} \tag{3.19}$$

Where ρ is the density of the material, k and α depend on the atomic number and energy E_b . [168]

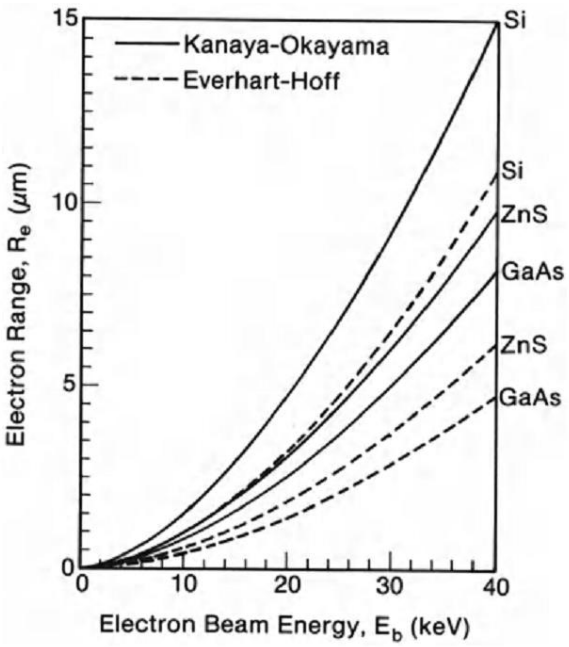

Figure 3. 8. Comparison of Everhart-Hoff and Kanaya-Okayama models for the generation volume in different materials as a function of beam energy E_b. [90]

So, the generation volume (excitation volume) in a material is calculated, according to Everhart and Hoff,

$$R_e = (0.0398/\rho) E_b^{1.75} (\mu m) \tag{3.20}$$

ρ is in g/cm^3 and E_b is in keV. [90] This result is valid only for electron energy range 5-25keV and atomic numbers 10<Z<15. For a wider range Kanaya and Okayama relation must be used, which is

$$R_e = (0.0276A/\rho Z^{0.889}) E_b^{1.67} (\mu m) \tag{3.21}$$

where A is the atomic weight in g/mol, ρ is in g/cm^3 and E_b is in keV and Z is the atomic number. A comparison of Everhart-Hoff and Kanaya-Okayama models is shown in Figure 3.8.

The shape of the generation volume depends on the atomic number. For low atomic numbers (Z) the shape is like a pear, for 15<Z<40 it is spherical in shape, for larger atomic numbers it resembles a hemisphere. [92]

The generation rate of electron-hole pairs is given by,

$$G = \frac{V_b I_b (1-\gamma)}{eE_i} = \frac{V_b I_b \, \mathrm{Q}(1-\gamma)}{eE_g} \tag{3.22}$$

Where V_b is the electron beam voltage; I_b is the beam current; e is the electronic charge; E_i is the ionization energy (ie the energy requires fot the generation of an electron-hole pair); E_g is the semiconductor band gap; Q, is the quantum efficiency for electron-hole pair generation; and γ is the fractional electron beam energy loss due to backscattered electrons. Everhart and Hoff proposed a universal depth dose function $g(y)$, which represents the number of electron-hole pairs generated by one electron of energy E per unit depth per unit time. [90] The CL resolution is determined by electron probe size, the size of generation volume, and the minority carrier diffusion length.

The photons in the ultraviolet, visible, and near infrared region of the spectrum constitute the CL signal in SEM. These photons are a result of transitions between conduction and valence bands and levels in the band gap of the materials. Notably, many of the signals are due to impurities and defects in the materials under investigation. CL describes the radiative emission processes and the CL intensity (i.e., the number of photons emitted per unit time) is derived from the overall recombination rate $(\Delta \mathrm{n(r)}/\tau)$. Assuming a linear dependence of CL intensity on the stationary excess carrier density the total CL intensity is expressed as,

$$L_{CL}(\mathrm{r}) = \int f \frac{\Delta n(\mathrm{r})}{\tau_{rr}} d^3 r \tag{3.23}$$

Where f is a function containing correction parameters for CL detection system, τ_{rr} is the radiative recombination lifetime and $\Delta \mathrm{n(r)}$ is the excess minority carrier density.

For a detailed derivation refer to Jacobi and Holt. [90] In summary, the CL intensity can be expressed as:

$$LCL = f_D f_A f_R \eta \frac{GI_b}{e} \tag{3.24}$$

Where f_D is a constant factor that takes into account parameters of CL detection system, the photomultiplier quantum efficiency, transmissive efficiency of the monochromator and the signal amplifier. Here, f_A and f_R are factors that account for absorption and internal reflection losses.

It is essential to have an efficient light collection, transmission, and detection system associated with any CL instrumentation. The schematic of a CL detection system is shown in Figure 3.9. Various kinds of information, micrographs or spectra, can be recorded according to our needs. The monochromatic micrographs can be obtained by keeping a constant monochromator setting and a scanning electron beam condition. The spectral information is derived, if the monochromator is stepped through the range of wavelengths and the electron beam is stationary or scans a small area. Bypassing the monochromator grating produces the panchromatic (integral) CL signal.

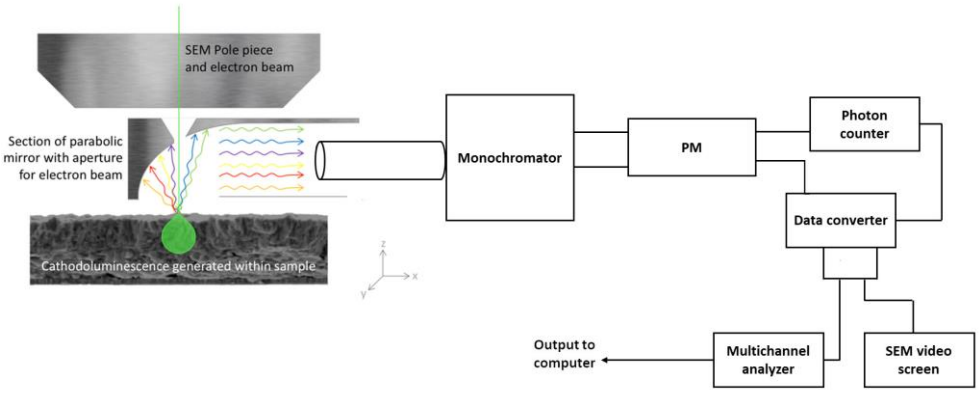

Figure 3. 9. The schematic of a CL detection system. Adapted from. [90]

Various techniques exist for the light collection including reflective optics, refractive optics, and metallic light pipes. Our CL system uses a parabolic mirror for the collection of light and a fiber optic guide for transmission of the signals. There are various kinds of collectors employed in the

CL collection systems, like semi-ellipsoidal mirrors. [169] As depicted in the Figure 3.9, the electron beam incidents on the sample and generates the light which is focused by the mirror and transmitted via a fiber optic bundle to the entrance slit of the monochromator. Then, it is fed to a photomultiplier tube (PMT). The PMT output is a train of pulses corresponding to the incident photons. The output from the photon counter is then fed through a video amplifier to a display to produce CL images or to a computer. [92] The spectral response of detection system must be calibrated properly as the detection correction significantly changes the CL intensity, the shape of the band, and the value of the peak position. [170,171]

For the simultaneous detection of all wavelengths in a CL spectrum, a silicon intensified target (SIT), vidicon camera and an optical multichannel analyzer (OMA) are used. [172,173] The other variation of CL includes transmission CL and emission CL infrared panchromatic microscopy [174,175] and CL in scanning transmission electron microscopes (STEM) [176,177]. In the infrared range a Fourier transform spectrometry coupled with Michelson interferometry has been employed. In this method an interferogram of the CL emission is produced and it is then converted into the CL spectrum by Fourier transform of these data. [98,178]

A temperature dependence is observed in the case of CL emission bands. As the temperature decreases it is found that the band intensity increases and the bands become much sharper (because thermal broadening is reduced). Time resolved CL was used in the semiconductor industry for calculations of both the minority carrier lifetime and the surface recombination velocity. [103] The interpretation of CL emission is not trivial, since it involves the effect of defects, temperature, stress and surface morpholopgy. However, the bandgap related emission is easy to interpret. Since there is a lack of a generally applicable theory for the variety of luminescence centers and radiative recombination mechanisms, the interpretation of broad CL bands is difficult.

The development in the ways in which emitted light is collected and analyzed have radically changed the impact of CL as an analytical tool and broadened its applications. Advancements in CL instrumentation made it possible that a wide range of photon properties other than energy and intensity can be accessed. Those developments can enhance the contribution of CL across a series of materials—semiconductors, plasmonic structures, biological materials, geological materials and nanostructures. [126]

3.3.2 X-ray Absorption Spectroscopy (XAS)

High brilliance synchrotron x-rays are used in x-ray absorption spectroscopy (XAS) to understand element specific information about local atomic and electronic structure of materials. In XAS, x-rays excite core electrons from the low energy bound states in the atoms. This liberated photoelectron wave is scattered by the surrounding atoms and create interference between outgoing and scattered parts of wave function. These interferences cause an energy dependent variation in x-ray absorption probability, which is proportional to x-ray absorption coefficient. [179,180] In this technique, the intensity of the transmitted x-ray (I_t) beam is measured as a function of x-ray energy (E). Simultaneous measurement of incident beam intensity (I_0) is performed along with I_t measurement. According to Beer-Lambert law, the x-ray absorption coefficient $\mu(E)$ is given by,

$$\mu \cdot d = \ln \frac{I_0}{I_t} \tag{3.25}$$

Where d is the sample thickness. A XAS spectrum for CeO_2 powder (Sigma Aldrich®) is shown in Figure 3.10. The sudden increase in absorption coefficient is called an absorption edge, it depends on the atomic number of the absorbing atom.

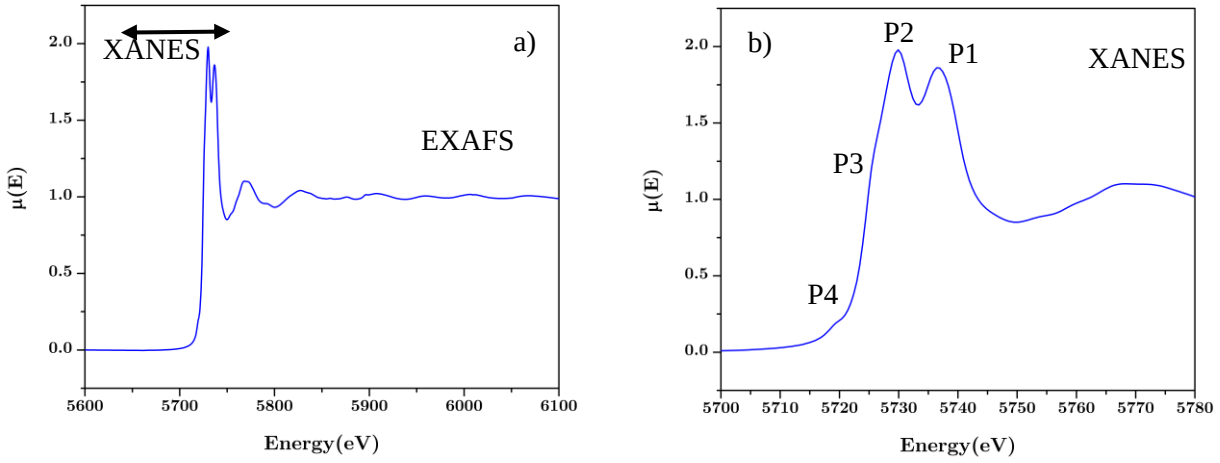

Figure 3. 10. X-ray absorption spectrum for CeO_2 at the Ce-L_3 Edge. $\mu(E)$ is the absorption coefficient.

Depending on the principal quantum number n of the state from which the excitation is occurred, the absorption edges are labelled as K, L or M. The edge K corresponds to 1s state, L

corresponds to 2s, $2p_{1/2}$, and $2p_{3/2}$ states (L_1, L_2, L_3 respectively), and M corresponds to 3s, $3p_{1/2}$, $3p_{3/2}$, $3d_{3/2}$, and $3d_{5/2}$ states (M_1, M_2, M_3, M_4 and M_5 respectively). [181] Both L_3 and K-edge of Ce can be measured with synchrotron x-ray sources. Since Ce L_3- edge EXAFS is limited to about 400 eV above the edge (due to Ce L_2- edge), Ce K-edge has to be measured for EXAFS.

The x-ray absorption spectrum (Figure 3.10) can be divided into two regions: the x-ray absorption near edge structure (XANES) and the extended x-ray absorption fine structure (EXAFS). XANES give valence state information so that a quantification of Ce^{3+} and Ce^{4+} is possible in the case of CeO_2. The peak positions and relative intensities in XANES reveal the local geometry, the number and degree of order in the neighbors about the central atom being investigated. [78,79,182] The XANES region includes features starting from 40 eV below the absorption edge and extend up to 50 eV above the edge. From the literature it is found that the peaks P1 and P2 in CeO_2 XANES (Figure 3.10) result from many body final states (i.e., mixing of $4f^0$ and $4f^1L$ final configurations where L represents a hole in the delocalized O2p band). [179] The peak denoted as P3 is a result of crystal field splitting of 5d states. While the pre-edge feature P4 is a result of multiple scattering. The average valence state of Ce atom (i.e., the relative amount of Ce^{3+} and Ce^{4+} species) is determined from a linear combination fit analysis of Ce L_{II} -edge XANES spectra. For this purpose, we should have proper reference compounds with known valence states, similar symmetry, same kind of neighbor atoms in nearest coordination shell, and arranged in a similar local structure. [183] We have used CeO_2 nanopowder as reference for Ce^{4+}, and $CeVO_4$ was used as a reference for Ce^{3+}.

The EXAFS region delivers information about the nearest neighbor environment. This includes information about the coordination numbers, interatomic distances and their disorder. The region in the XAS spectrum that extends about 1000-1500 eV above the absorption edge constitutes the EXAFS. The origin of EXAFS is the interference of x-ray radiation by the outgoing photoelectron waves and those scattered back to the absorbing atom by its neighbors. [180,184,185] Stern et al. [186] recognized that the modulation observed in the x-ray absorption spectrum is related to the radial distribution of neighboring atoms around the central absorbing atom. It is important to note that the information from the EXAFS is element specific and local, because of the short photoelectron mean free path and bond length disorder increases from the absorber and diminishes at higher order coordination shells. [187–189] Extraction of

information regarding the local atomic and electronic environment from EXAFS data involves multiple steps.

Ce L_{III} -edge x-ray absorption spectra of CeO_2 was measured in transmission detection mode at the XAFS beamline of the ELETTRA synchrotron radiation facility in Trieste, Italy. A Si (111) double crystal monochromator was used with energy resolution of about 0.6 eV at 6 keV.The CeO_2 samples were prepared in the form of homogeneous pellets, pressed from micronized powder mixed with boron nitride (BN), with the total absorption thickness of about 1 above the Ce L_{III} -edge, and placed in the monochromatic beam between first two ionization detectors. The exact energy calibration was established with simultaneous absorption measurement on the nanopowder CeO_2 reference sample placed between the second and the third ionization chamber. The quantitative analysis of XANES spectra was performed with the Demeter (IFEFFIT) program package. [190]

We performed the Ce and La K-edge EXAFS at PETRAIII beamline at DESY in Hamburg (Germany). The spectra were measured at room temperature in transmission detection mode. The samples for EXAFS analysis were prepared in the form of homogeneous pellets, pressed from micronized CeO_2-based powder mixed with boron nitride (BN) powder, with the total absorption thickness μ_d of about 2.5 above the Ce K-edge (40444 eV). A Si (311) double crystal monochromator was used with energy resolution of about 3 eV at 40 keV. Demeter (IFEFFIT) program package was used for the quantitative analysis of EXAFS spectra. [190] Further details of the experiments are given in Chapter 4 and 5.

3.3.3 Impedance Spectroscopy

Knowing the impedance, capacitance and dielectric response of the materials we can have insight into the physical and chemical properties of materials. The desired response is often monitored as a function of frequency. In the impedance spectroscopy, the input signal (V_{ac}) is varied with the frequency and the resulting change in current (I_{ac}) is measured. Figure 3.11 shows relaxation processes in materials as a function of frequency. It can be seen that the molecular polarization and dipolar rearrangement occur in the frequency range 10^3 to 10^{12} Hz. The relaxation processes are reflected in the frequency dependence of permittivity of the materials. [191]

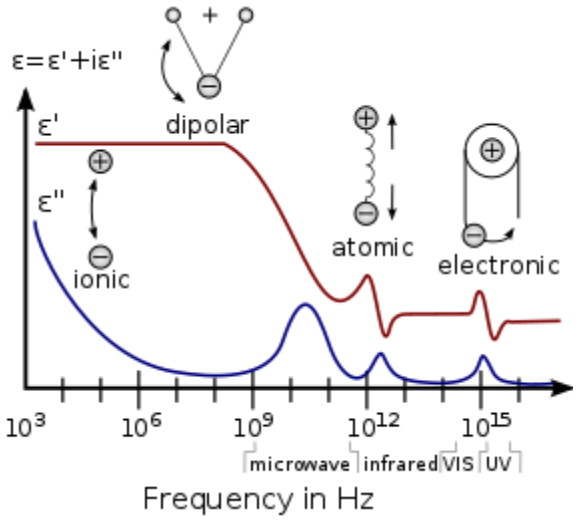

Figure 3. 11. The dependence of real and imaginary part of permittivity with frequency. [192]

As mentioned above, in the impedance spectroscopy, the current response I_{ac} of a material is measured as a function of applied voltage V_{ac}. The current (I_{ac}) and voltage (V_{ac}) can be expressed as

$$V(\mathrm{t}) = \mathrm{V}_0 \sin(\omega \mathrm{t}) = \mathrm{V}_0 e^{i\omega t} \tag{3.26}$$

$$I(\mathrm{t}) = I_0 \sin(\omega t + \phi) = \mathrm{I}_0 e^{i(\omega t+\phi)} \tag{3.27}$$

Where V_0 and I_0 are the amplitude of voltage and current respectively. ω is the angular frequency ($\omega = 2\pi f$), ϕ is the phase angle and t is the time. The impedance (the complex resistance of the material) is given by,

$$Z(\mathrm{t}) = \frac{V(t)}{I(t)} = Z_0 e^{-i\phi} \text{ where } Z_0 = \frac{V_0}{I_0} \tag{3.28}$$

There are different ways to represent input and output signals. The frequency and time domain representations are shown in Figure 3.12 (a).

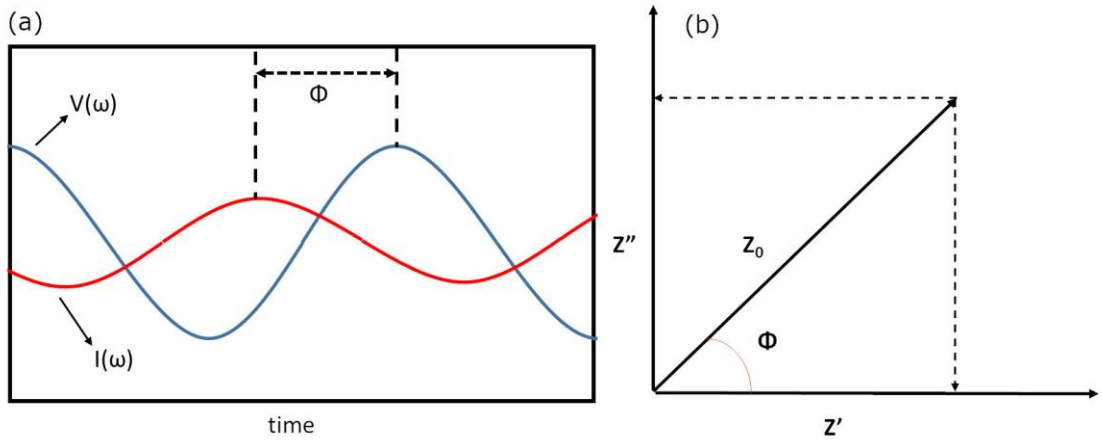

Figure 3. 12. (a) Time domain representation of input V(t) and output I(t). (b) Impedance Z is represented in frequency domain Here $Z_0 = \frac{V_0}{I_0}$ and ϕ is phase angle . [191]

In the complex plane (Figure 3.12 (b)) Z is expressed as,

$$Z = Z' - iZ'' \tag{3.29}$$

Where Z' and Z'' are the real and imaginary components of Z.

The magnitude of Z is given by

$$Z = \sqrt{Z'^2 + Z''^2} \tag{3.30}$$

Physically, Z' corresponds to the resistance R, and Z'' is the reactance X.

They can be described as,

$$Z' = R = Z_0 \cos(-\phi) = Z_0 \cos(\phi) \tag{3.31}$$

$$Z'' = X = Z_0 \sin(-\phi) = -Z_0 \sin(\phi) \tag{3.32}$$

Here I used impedance spectroscopy as a tool to understand the variation in defect concentration as a result of sintering described in section 4.3. As from the impedance measurement we can extract complex capacitance and hence the dielectric permittivity ε' (real part of permittivity) and ε'' (imaginary part of permittivity). The relative number of dipoles present in the system and its polarizability can be correlated with the concentration of oxygen vacancies in CeO_2. Besides,

the presence of small polarons can be deduced from of the dependence of ε'' with frequency. This is the topic of discussion in Chapter 4.

4 Oxygen-Vacancy Related Cathodoluminescence Quenching and Polarons in CeO_2

4.1 Introduction

Because of its fundamental ability to accommodate a large number of defects without destabilizing the crystal structure, cerium oxide (ceria, CeO_2) has become a technologically important material that finds its use in many areas. Perhaps the most widespread of which is its application in automobile exhausts as a catalyst [193] due to its ability to absorb and release oxygen under oxidizing and reducing conditions. From a crystallographic point of view this means that the ceria crystal structure can tolerate a high density of oxygen vacancies as well as reduced cerium ions, Ce^{3+}. The density of these defects is associated with the external oxygen partial pressure.

Other important properties of CeO_2, such as a high dielectric constant and good epitaxy on Si substrate, make it a potential material for future microelectronic applications. In particular, epitaxial CeO_2 films are considered to be very promising candidates for high quality and highly stable insulating thin films. [194] There have been extensive studies on defects in ceria, which focused on their formation by doping, treatment in reductive or oxidative atmosphere, [195,196] and the dependence on a crystal size [197,198] and atomic surface structures. [199,200]

Despite its ability to unravel the defect structures of crystals, cathodoluminescence spectroscopy has found little use in the study of CeO_2 emissions related to oxygen vacancies. CL spectroscopy is highly sensitive to relatively low defect concentrations, and can be used to determine carrier recombination pathways that involve those defects. This makes it a technique of choice for studies of the defect structures in bulk as well as nanostructures. [201] Previously, it has been shown that CL can be used as a direct tool for studying the oxygen vacancy concentration in the vicinity of oxide surfaces. [202] CL is also able to provide information on mechanical stresses originating from oxygen vacancies. [89]

The emissions associated with oxygen vacancies in ZrO_2-related materials, as well as Al_2O_3 and TiO_2, have been studied by spectrally and spatially resolved CL spectroscopy. [88,203] It has

been reported that the CL intensity for Y-doped ZrO_2 decreases with an increase in the concentration of oxygen vacancies. In this study, Boffelli et al. [89] proposed two hypotheses to explain the observed intensity quenching. The first hypothesis, called the "strained lattice hypothesis", states that since the efficiency of the CL intensity is directly related to Zr-O bond stretching and the increased concentration of oxygen vacancies redistributes the highly localized lattice strain, the CL emission intensity lowers with the higher vacancy concentration. The second, the "charge trap hypothesis", states that the decrease in the CL intensity under the electron excitation occurs due to the fact that the oxygen vacancies act as charge traps and thereby decrease the number of available electrons; the more the vacancy sites, the lower the CL intensity.

The presence of charged vacancies is put forth to explain many of the experimental observations. The possibility of formation of oxygen vacancy complexes has been proposed and experimentally observed. In the case of doped ceria, a conductivity maximum has been observed as a function of dopant concentration. [204] Initially, it was explained by the presence of a minimum in the activation enthalpy as the dopant concentration increases. Later this was rejected by Faber et.al. [205] who argued that the lattice relaxations around the dopant ions will screen any columbic effects arising from the dopant. They ascribe the presence of the minimum to changes in the energy of the oxygen sites in the vicinity of the dopant. Altogether, it is proposed that the presence of this minimum in the concentration dependence of the activation enthalpy can be taken as an indicator of defect association, which limits the conductivity of doped ceria [206].

The objective of this work is to demonstrate the CL behavior of CeO_2 and its dependence on oxygen vacancy concentration. We report that the intrinsic oxygen vacancies in CeO_2 cause CL intensity quenching when only above a critical concentration. It is shown that a careful understanding of CL emissions of CeO_2 could help to comprehend the interaction between vacancy centers. We examine the possibility of oxygen vacancies association with electron polarons and their consequence on the occurrence of differing charge states of the intrinsic point defects in CeO_2. The ability of the CL technique to explore different charge states of intrinsic point defects is demonstrated.

4.2 Methods

High purity CeO_2 nanopowders (Sigma Aldrich®, 99.95% pure, size < 50nm) were sintered at 1450°C for 8 hours in air (C-A), oxygen (C-O) and nitrogen (C-N). In the second step, all the three samples were subjected to quenching after a 10h annealing at different temperatures to achieve a frozen state with differing defect concentrations. The systematic change in defect concentration was verified by electrical impedance analysis.

A Rigaku MiniFlex diffractometer was used for the XRD measurements. Ni filtered Cu K_α radiation, steps of 0.05^o with collection time of 1s per step were used to acquire the data. XRD was analyzed by an X'Pert HighScore software.

Microstructural images and CL spectra were taken by a field-emission gun scanning electron microscope (SEM JEOLJSM 7100 TTLS (FEG)). For the CL measurements, the same experimental conditions were applied for all samples to avoid introducing additional variables. The acceleration voltage and the beam current were set for all experiments at 25 keV and 2nA, respectively. The CL spectra were acquired in the wavelength region 300 nm to 800 nm. The reported CL spectra have been corrected by grating response and detector response in the wavelength region 350nm to 750nm. The microscope was equipped with a CL device (GATAN MonoCL4) consisting of a parabolic mirror and a bundle of optical fibers, used to collect and to focus the electron-stimulated luminescence emitted by the sample into a monochromator with 2nm spectral resolution.

The dielectric properties of the samples (pellets) were studied using a frequency response analyzer (Agilent LCR E4980A). The impedance curves were obtained over a frequency range from 100 Hz to 2 MHz, using a two-probe measurement with copper tape electrodes in a capacitor geometry.

X-ray absorption spectra in the energy range of Ce L_3-edge (5724 eV) of the high purity CeO_2 nanopowder samples, before sintering and sintered at 1450°C for 8 hours in air (C-A), oxygen (C-O) and nitrogen (C-N), and crystalline $CeVO_4$ as a reference for Ce^{3+} were measured in transmission detection mode at the XAFS beamline of the ELETTRA synchrotron radiation facility in Trieste, Italy. A Si (111) double crystal monochromator was used with energy resolution of about 0.6 eV at 6 keV. Higher harmonics were eliminated by detuning of the

second monochromator crystal to 60% of the maximum in the rocking curve. The intensity of the monochromatic X-ray beam was measured by three 30 cm long consecutive ionization detectors filled with optimal gas mixtures for a given energy range: 350 mbar N_2 and 1650 mbar He (first); 1900 mbar N_2 and 100 mbar He (second); 230 mbar Ar, 1000 mbar N_2 and 670 mbar He (third).

The CeO_2 samples were prepared in the form of homogeneous pellets, pressed from micronized powder mixed with micronized boron nitride (BN), with the total absorption thickness of about 1 above the Ce L_3-edge, and placed in the monochromatic beam between first two ionization detectors. The absorption spectra were measured in the energy region from -150 eV to +400 eV relative to the Ce L_3-edge. Scans were stopped at Ce L_2-edge (6165 eV). Equidistant energy steps of 0.3 eV were used in the XANES region, while for the EXAFS region equidistant k steps of 0.03 $Å^{-1}$ were adopted, with an integration time of 2 s/step. The exact energy calibration was established with simultaneous absorption measurement on the nanopowder CeO_2 reference sample placed between the second and the third ionization chamber. Absolute energy reproducibility of the measured spectra was ±0.03 eV. The quantitative analysis of XANES spectra was performed with the Demeter (IFEFFIT) program package [190].

4.3 Results and Discussion

Samples C-O, C-A, and C-N, have been sintered in oxygen, air, and nitrogen atmospheres respectively, with the scope of obtaining CeO_2 samples having an increasing concentration of oxygen vacancies due to processing in higher to lower oxygen partial pressure atmospheres.

Scanning electron microscopy showed no detectable difference in the microstructures of the investigated samples. The level of porosity and grain size are the same for all the samples. XRD analysis showed the presence of pure CeO_2 phase with no traces of Ce_2O_3. A typical microstructure and XRD are shown in Figure 4.1 for the sample C-N. Figure 4.2 shows a comparison of the microstructure for C-O and C-A samples.

The relative amounts of Ce^{4+}, and Ce^{3+} species in the catalyst after sintering in different atmospheres were determined from the Ce L_3-edge XANES spectra (Figure 4.3). Different local environments of the Ce cation result in different L_3-edge profiles in the XANES spectra, and the energy position of the absorption edge is correlated with the valence state of the absorbing atom

in the sample. With increasing oxidation state the absorption edge is shifted to higher energies.

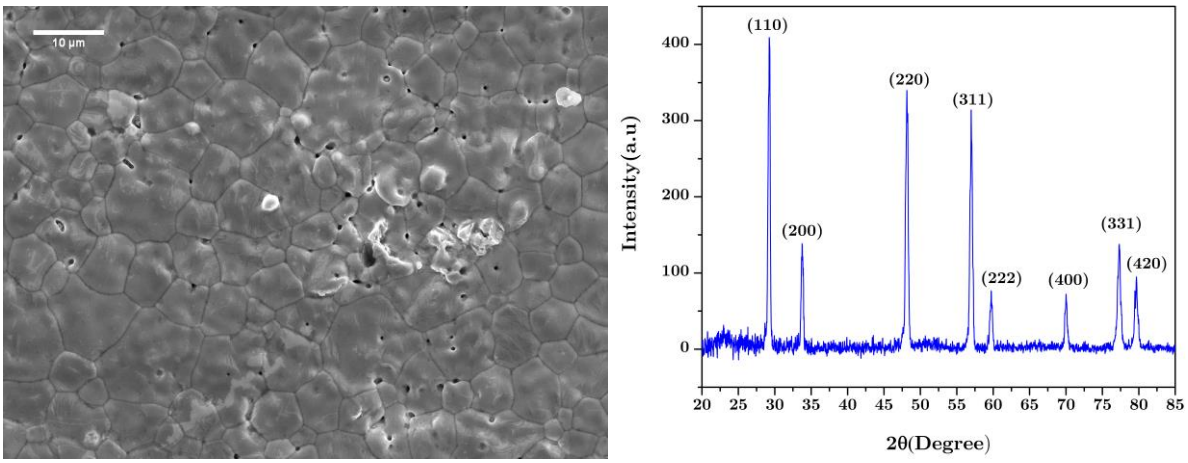

Figure 4. 1. SEM micrograph (left) and XRD (right) acquired from the C-N sample. All sample preparations showed similar structure with no variation in porosity or grain size.

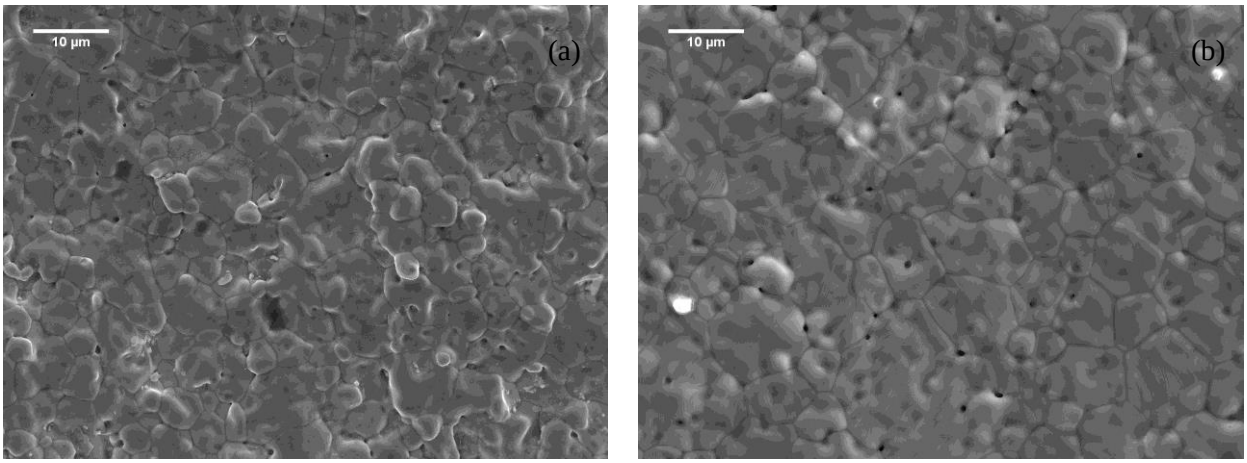

Figure 4. 2. SEM micrograph for samples (a) sintered in oxygen (C-O) and (b) air (C-A). The average grain size for both samples was about 8 µm. This was similar to the sample sintered in nitrogen (C-N).

In case of Ce^{3+} cations a characteristic peak is present at 5726 eV, while Ce^{4+} cations can be identified by two characteristic peaks, at 5730 eV and 5736 eV [207–209]. A detailed comparison of the three XANES spectra show that the spectra of C-O and C-A sample are identical within noise level, while the spectrum of C-N sample sintered in nitrogen exhibits some differences in the pre-edge region at 5726 eV, which can be ascribed to a presence of small amount of Ce^{3+} in the crystal structure of CeO_2. Relative amounts of Ce^{3+} species is quantitatively determined by a linear combination fit analysis [190,209]. The XANES spectrum

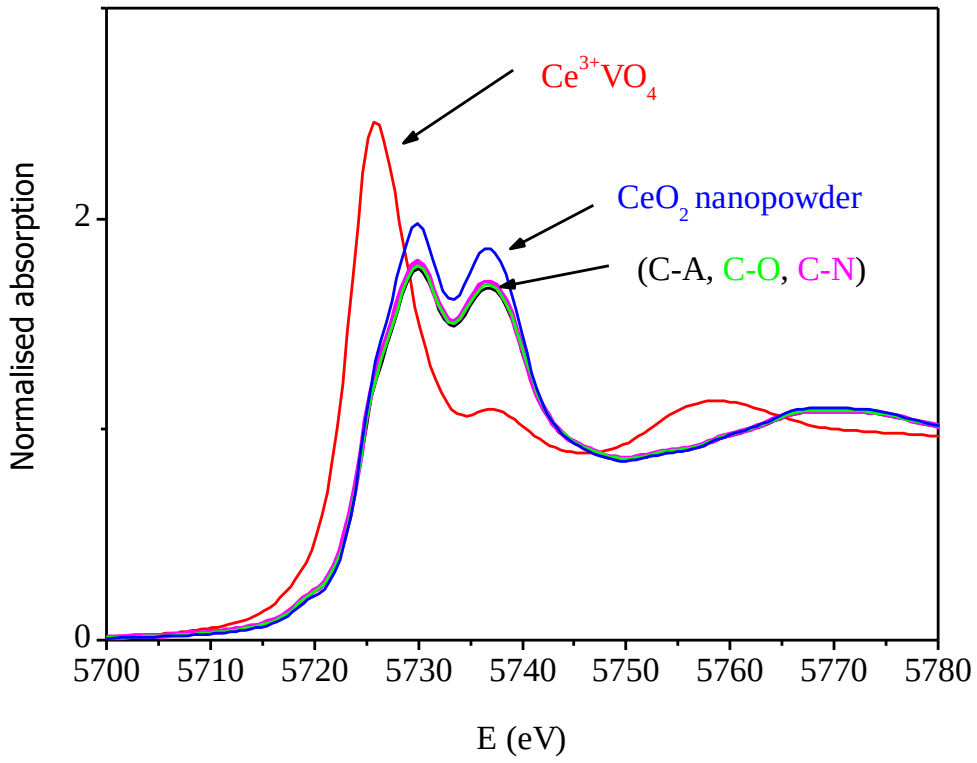

Figure 4. 3. Normalized Ce L_3-edge XANES spectra of the CeO_2 nanopowder samples, sintered at 1450°C for 8 hours in air (C-A) (black line), oxygen (C-O) (green line), and nitrogen (C-N) (magenta line), together with the spectra of corresponding Ce reference compounds (crystalline unsintered CeO_2 nanopowder as reference for Ce^{4+}, and crystalline $CeVO_4$ as reference for Ce^{3+}).

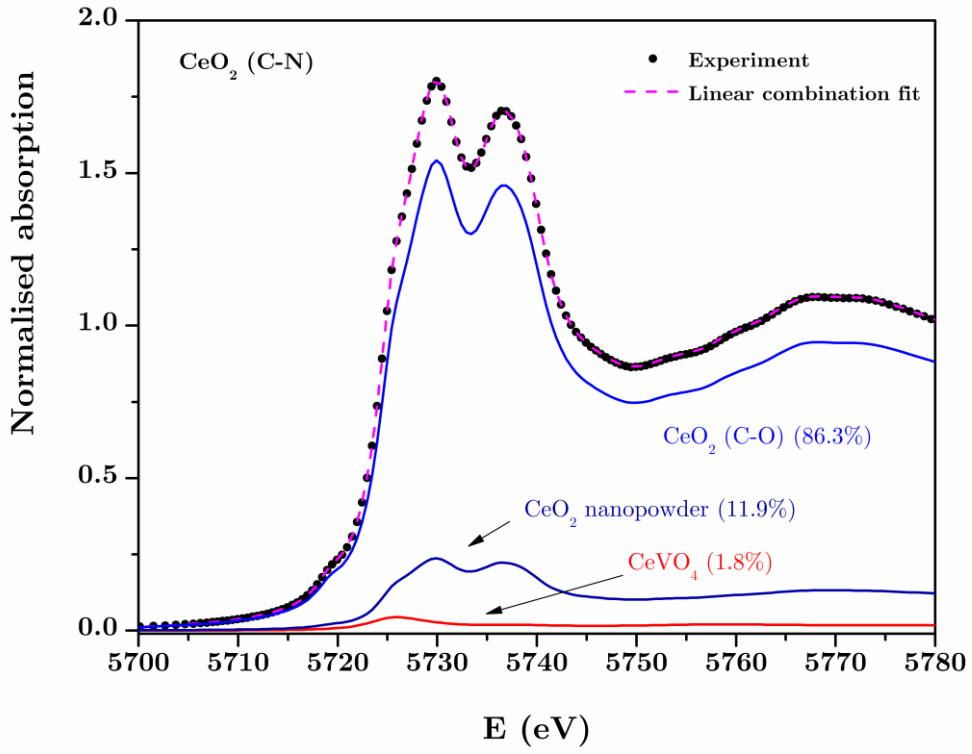

Figure 4. 4. Ce L3-edge XANES spectrum of the CeO_2 nanopowder sample sintered in nitrogen (C-N). Dots are experiment data; dashed magenta line is the best fit from a linear combination of reference Ce L_3-edge XANES profiles (86.3% CeO_2 nanopowder sintered in oxygen (C-O) as reference for Ce^{4+} (blue), 11.9% crystalline unsintered CeO_2 nanopowder as reference for Ce^{4+} (dark blue), and 1.8% crystalline $CeVO_4$ as reference for Ce^{3+} (red).

of the CeO_2 sintered in nitrogen (C-N) can be completely described by a linear combination of three reference XANES profiles (Figure 4.4): the spectrum of CeO_2 nanopowder sintered in oxygen (C-O) (86.3%), the spectrum of crystalline unsintered CeO_2 nanopowder (11.9%) as references for Ce^{4+}, and the spectrum of $CeVO_4$ as reference for Ce^{3+} (1.8%). Statistical uncertainty for the relative amount of Ce^{3+} is ±0.1%. Evidentially the presence of Ce^{3+} cations in the C-O, and C-A samples, sintered in oxygen and in air respectively, are below detection limit of the method (< 0.2%).

Figure 4.6a) shows the representative CL spectra acquired under identical conditions on CeO_2 samples, sintered in different atmospheres. CL spectra of the different samples showed a pronounced variation in their intensities. All the three spectra are composed of a broad band, centered at approximately 550 nm (2.25 eV), along with two additional narrow peaks at 575 nm (2.15 eV) and 617 nm (2.00 eV).

The narrow peaks in the spectra were recognized as emissions from impurities. It is known from photoluminescence (PL) studies that Sm^{3+} gives emissions corresponding to the transitions $^4G_{5/2}$ to $^6H_{5/2}$ and $^4G_{5/2}$ to $^6H_{7/2}$ within the range 550 nm (2.25 eV) to 800 nm (1.54 eV). [210] The presence of 0.4 mg/kg of Sm impurity has been confirmed in our starting CeO_2 powder by an inductively coupled plasma mass spectrometry (ICPMS). Correspondingly, the narrow emission lines are assigned to the Sm impurity similarly as in Balestrieri et al. [210] The Sm^{3+} concentration is constant throughout all the samples because all samples used the same starting CeO_2 powder.

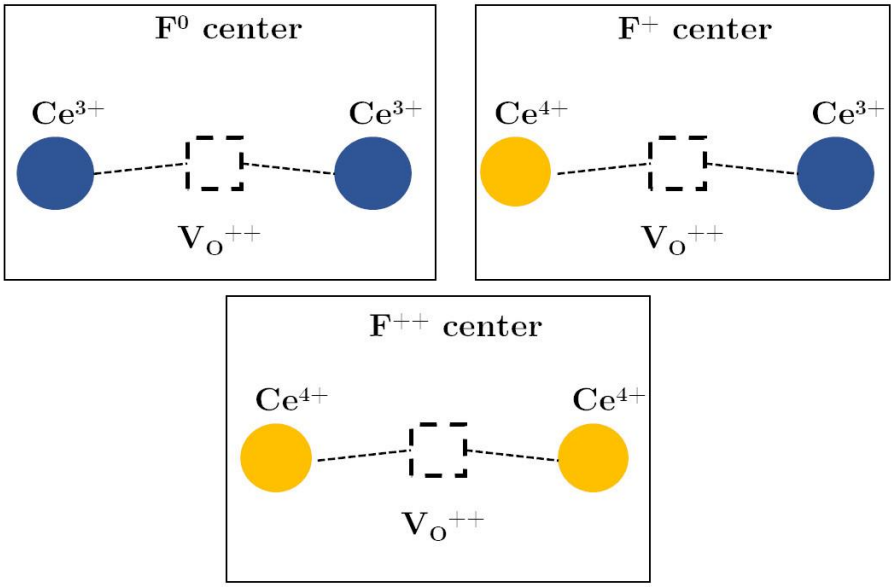

Figure 4. 5. A schematic illustration of the different electronic configurations of oxygen vacancies in CeO_2 and their respective F centers (note that charge neutrality is not shown). Adapted and reproduced from [211] with permission from Elsevier 2020.

Calculations [47] predict that, for CeO_2 with a neutral oxygen vacancy ($V_O^{\times}$) the electronic density of states (DOS) has two gap states between the O2p and the Ce4f bands, lying well inside the band gap. Since the two band gaps of CeO_2 are beyond the observed emission lines, it is reasonable to conclude that the emission centered at 550 nm originates from the defect energy levels within the band gap which can act like electron traps. The oxygen vacancies, $V_O^{\times}$, and their surrounding Ce ionic species can be described as F-centers in CeO_{2-x} as described by Costantini et al. [211]

The definition of F centers in CeO_{2-x} differs from the usual F^0, F^+, and F^{++} centers in MgO or Al_2O_3. The reason is that unlike Ce cations, Mg and Al cations cannot change their oxidation state. In their description, Costantini et al. [211] define three different types of Ce-V_O-Ce trimers corresponding to the three charge states of F centers (see Figure 4.5). Unlike the classical description of F centers, they proposed three different possible electronic configurations of neutral oxygen vacancy, in terms of Ce^{4+}- V_O^X- Ce^{4+} cluster. Considering the electro neutrality, the different electronic configurations of this cluster leads to three types of Ce^{3+} distances from the oxygen vacancy. As shown in the schematic (Figure 4.5) the F^0 configuration [Ce^{3+}- V_O^{++}- Ce^{3+}] will have two Ce^{3+} ions adjacent to oxygen vacancy. The F^+ configuration [Ce^{3+}- V_O^{++}- Ce^{4+}] will have a Ce^{3+} ion close to the vacancy, but the other Ce^{3+} ion at a larger distance from the vacancy. For the F^{++} configuration [Ce^{4+}- V_O^{++}- Ce^{4+}] two Ce^{3+} ions will be positioned at a larger distance from the vacancy. The oxygen vacancies cannot be dissociated from Ce^{3+} or Ce^{4+} ions, as a result of charge compensation process.

It has been shown [47] that the gap states of $V_O^{\times}$ lay at 1.75 eV whereas the gap state of $V_O^{\bullet}$ lies near the mid gap at about 2.25 eV. Several PL studies on CeO_2 reported bands in the region 2.07-2.35 eV and ascribed these to electron transitions from the excited state (F^{0*}) of the neutral oxygen vacancies to the corresponding ground state (F^0). [212,213] The other defect types that give rise to energy states within the band gap are cerium vacancy (V_{Ce}) at 2.75eV, interstitial cerium (I_{Ce}) at 1.85 eV and Frenkel defect at 1.02 eV. Since the formation energies for these defects are very high compared to V_O they should not contribute to the CL emission due to their low concentration. [47]

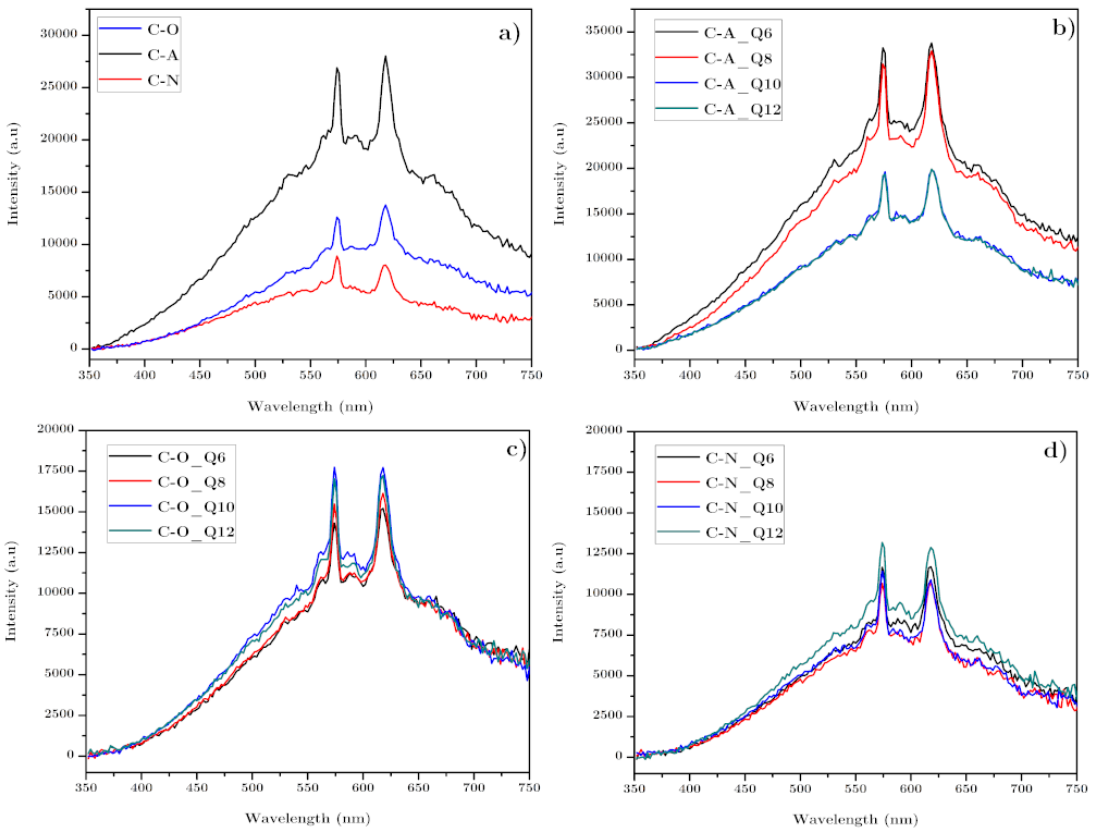

Figure 4. 6. a) CL spectra collected for CeO_2 samples sintered in air (C-A), oxygen (C-O) and nitrogen (C-N) atmosphere. CL spectra for samples thermally quenched from different temperatures in (b) air, (c) oxygen and (d) nitrogen atmosphere. Q6, Q8, Q10 and Q12 stands for thermal quenching at 600°C, 800°C, 1000°C and 1200°C, respectively. The C-A samples show a higher overall CL intensity and higher temperature dependence in vacancy formation.

A discernible variation in the CL intensity (see Figure 4.6 (a)) revealed the influence of defect concentration on the emissions of CeO_2. Conventional wisdom suggests that we should observe a linear relationship between the CL intensity and concentration of defects i.e. the emission intensity should increase with the defect concentration. [89,90,214,215] Surprisingly the intensity of the C-O sample lies in between the C-N and C-A samples. Accordingly we anticipated that, as the concentration of V_O increases, the CL intensity increases up to some critical concentration, where it then reaches a maximum and decreases.

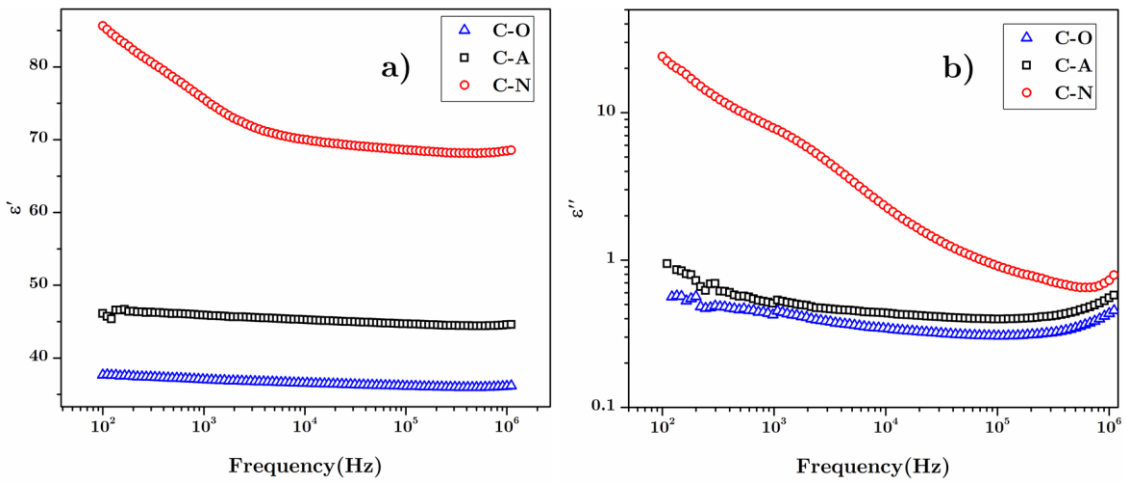

Figure 4. 7. Room temperature frequency dependence of (a) real part of dielectric constant, ε′ and (b) imaginary part of dielectric constant, ε″ for CeO_2 samples sintered in air, oxygen and nitrogen atmosphere, showing an increase in dielectric constant with decreasing oxygen partial pressure of the processing atmosphere.

Figure 4.7 shows the room temperature frequency dependence of the dielectric constant (ε′) and dielectric loss (ε″) measured from 100 Hz to 2 MHz. The values of ε′ and ε″ are extracted from impedance analysis. The existence of a polaron state can be seen mainly from the dielectric loss (ε”) at high frequencies due to hopping conduction with a classical power-law dependence on frequency. For the sample sintered in nitrogen both real (ε′) and imaginary (ε″) parts of dielectric constant show a decrease with increasing frequency. This can be explained on the basis of Maxwell-Wagner model. The higher value of ε′ at lower frequencies could be due to interfacial/ space charge polarization resulting from inhomogeneous dielectric structure (porosity and grain structure). At low frequencies charge gets accumulated at grain boundaries resulting in the formation of charged layers which make large contributions to dielectric constant. The charge piles up at grain boundaries is hindered at high frequencies, as the direction of motion of charge carriers is reversed before reaching the grain boundaries. Hence the dielectric constant decreases at high frequencies. Additionally, the formation of defects can contribute to increase in interstitial polarization and in turn leads to a high value of dielectric constant. [216] The same idea can be applied to dielectric loss (ε″). As described above charge accumulates at the grain boundaries in the low frequency region. Due to high resistivity of grain boundaries, just as in the case of ferrites, more energy is required for electron exchange resulting in high value of energy

loss. As the frequency increases, energy requirement for electron hopping is reduced and hence the dielectric loss is reduced. [216,217]

The dielectric constant increases significantly with increasing oxygen vacancies from C-O to C-N. The greater polarizability of a crystal with structural point defects as compared to an ideal defect-free crystal can be explained mainly by the high polarizability of the two electrons trapped in the vacant sites and the reduction in bond stiffness. According to the literature [218], V_O reduces the bond stiffness of some bonds which increases bond deformation. Since the bonds with reduced stiffness in the defective oxides deform more readily under an electric field, this also means that they are more readily polarized. This substantiates that the Vo concentration increases in the order C-O<C-A<C-N. Moreover, from the XANES analysis we have seen that for the C-O and C-A samples, the presence of Ce^{3+} cations was below the detection limit for the method whereas in C-N sample the amount of Ce^{3+} ions was estimated at 1.8%.

To further investigate the dependence of the defect concentration on the CL intensity, we performed a series of experiments where we thermally quenched the samples at different temperatures and in different atmospheres, the results of which are depicted in Figure 4.6 (b-d). For the C-A sample it was found that the CL intensity decreases with the increase in the quenching temperature (Figure 4.6 (b)) while for C-O (Figure 4.6 (c)) and C-N (Figure 4.6 (d)) the intensity stays nearly constant. The observed variations in the CL intensity can be explained by the fact that processing CeO_2 in different atmospheres sets different initial oxygen vacancy concentrations, which are later varied as a function of quenching temperature. In the C-O samples, the oxidation potential of the oxygen atmosphere limits the creation of oxygen vacancies and this effect strongly dominates over any thermal variation, thus quenching temperature has little effect on the vacancy concentration. However, in the C-A samples, the oxygen partial pressure is significantly lower and the thermal quenching temperature can lead to a considerable variation of the defect concentration and thus the CL intensity. In contrast, the quenched C-N samples all show very similar emission intensities due to similar vacancy concentrations. This can be explained with the fact that for high vacancy concentration the formation energy of new vacancies within the bulk progressively increases. [219,220] Therefore, there are not significantly more vacancies created at the higher temperatures and no significant variation in the CL intensity is seen.

A detailed understanding of the relative concentration of the different charge states of F centers associated to oxygen vacancies for the different CeO_2 samples has been obtained by curve fitting analysis of CL spectra as reported in Figure 4.6 (a). For the deconvolution of the spectral lines, a set of eight Gaussian bands were used and the results are reported in Figure 4.8 (a-c). Note that the wavelength dispersion is presented in the energy scale (eV), so that a meaningful comparison of the spectral weights of the components becomes possible.

Five sharp peaks are found at 2.00, 2.10, 2.16, 2.20, and 2.35 eV while three much broader peaks are located at 1.87, 2.11 and 2.70 eV referred to as P1, P2, and P3 respectively. The sharp peaks are the clear signature of the Sm trace impurity in the purchased CeO_2 powder as discussed above.

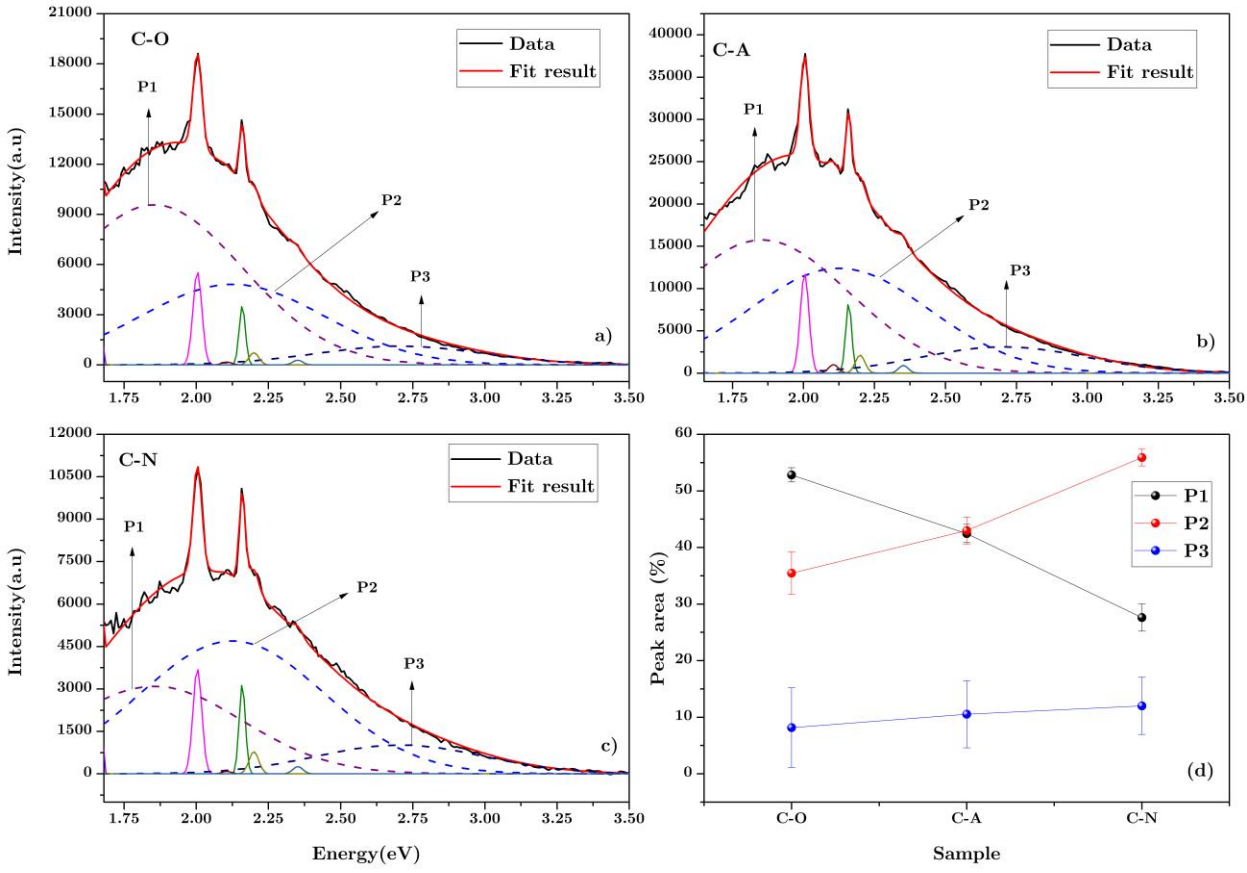

Figure 4. 8.(a-c). Gaussian deconvolution of the CL spectra collected from the CeO_2 samples sintered in oxygen, air and nitrogen respectively; (d) Peak area percentage, i.e. ratio of P1 (purple), P2 (blue), P3 (dark blue) peak area to their overall sum for each of CL spectra.

From Figure 4.8 d) it is clear that as the oxygen partial pressure decreases and thus the vacancy concentration increases, the component P2 grows at the expense of P1 whereas the P3 component stays relatively constant.

The band observed at 1.87 eV (P1) can result from the radiative emission of the transition from the F^+ state to the valence band. [212] This is supported by the fact that the electrons from the valence band cannot be excited to the F^0 ground state whereas the $4f^1$ band is positioned at only 1.2-1.5 eV above the valence band. [221,222] According to the calculations [47], $V_O^{\bullet}$ (F^+) is should never be the most stable charge state yet it shows a strong CL emission. One proposed mechanism for this discrepancy would be disproportionation according to the reaction

$$2V_O^{\bullet} \rightarrow V_O^{\times} + V_O^{\bullet\bullet} \tag{4.1}$$

leaving a neutral ($V_O^{\times}$) and a +2-charge state ($V_O^{\bullet\bullet}$). However, the experimental results do not support this mechanism because we have not observed any evidence of $V_O^{\bullet\bullet}$ expected at 3 eV [212]. Additionally some studies [211,223] have dismissed this P1 peak as being a product of element impurity, but the clear trend we observe in this peak as a function of oxygen partial pressure indicates that this is unlikely to be the case. For this reason, we propose different mechanism that is in full accordance with the experimental results presented and the calculations reported in the literature. [50,224,225]

It has been reported [226,227] that association between polarons and charged oxygen vacancies occur to resemble neutral and singly charged oxygen vacancies as follows:

$$V_O^{\bullet\bullet} + Ce'_{Ce} \rightarrow (V_O^{\bullet\bullet} - Ce'_{Ce})^{\bullet} \tag{4.2}$$

$$V_O^{\bullet\bullet} + 2Ce'_{Ce} \rightarrow (Ce'_{Ce} - V_O^{\bullet\bullet} - Ce'_{Ce})^{\times} \tag{4.3}$$

According to Zacherle et al. [50] at high oxygen partial pressures, doubly charged oxygen vacancies $V_O^{\bullet\bullet}$ are the dominant vacancy species. Considering the energy of formation of various charged defects, the next possible candidate is $(V_O^{\bullet\bullet} - Ce'_{Ce})^{\bullet}$ which resembles single charged oxygen vacancy. Castleton et al. [59] showed that the energy level for $(V_O^{\bullet\bullet} - Ce'_{Ce})^{\bullet}$ is present at ~1.7−2.0 eV. Since there is no distinction between $(V_O^{\bullet\bullet} - Ce'_{Ce})^{\bullet}$ and $(V_O)^{\bullet}$ except for the

electronic structure of the two defect species, we ascribe emission P1 to Ce^{3+} in configuration of F^{+} in Figure 4.8 (a).

Based on the calculations by Zacherle et al.[35] mentioned above, we attribute the CL band (P2) observed in the region 2.11eV to F^{0} center transition. At low oxygen partial pressures, the Ce^{3+} concentration increases and the cluster of a doubly charged oxygen vacancy with two polarons $(Ce'_{Ce} - V_O^{\bullet\bullet} - Ce'_{Ce})^{\times}$ becomes the energetically most favorable species, hence P2 emission originates from the configuration equivalent to F^{0}.

From a crystallographic point of view, the reduction of CeO_2 introduces strain in the crystal lattice due the formation of oxygen vacancies and Ce^{3+}, which has a larger ionic radius (1.01Å and 0.87Å for Ce^{3+} and Ce^{4+}, respectively). [228] The observed clustering of Ce^{3+} around the oxygen vacancies is driven by a reduction of the lattice strain and consequent reduction of free energy. With an increase in overall defect concentration, the strain increases, and the structure compensates by bringing yet another Ce^{3+} ion into the first coordination sphere around the vacancies. This explains why the increase in P2 emissions coincides with the decrease in P1 emissions.

The emission P3 in all the samples studied stays almost constant irrespective of processing atmosphere or temperature, with a slight increase as the oxygen partial pressure decreases. We ascribe this emission to F^{++} configuration which is consistent with Costantini et.al. [211] According to them, the CL emission at P3 in CeO_2 originates from Ce^{3+} ions which are not spatially adjacent to oxygen vacancies. As the F^{++} configuration describes oxygen vacancies surrounded by Ce^{4+} ions, their presence would imply the vacancy electron localized on a Ce^{3+} ion at an undistorted site further from the vacancy.

Therefore, we conclude that the observed trend in variation of bands can be explained as follows: at high oxygen partial pressure Ce^{3+} ions are readily found in F^{+} configuration, and the band P1 is the dominant emission in C-O sample. As reduction induces more vacancies and thus more Ce^{3+} ions into the crystal structure, the configuration F^{0} is favored, hence P2 becomes dominant in the C-N samples. An illustration of the radiative electronic transitions on CeO_2 samples is reported in Figure 4.9.

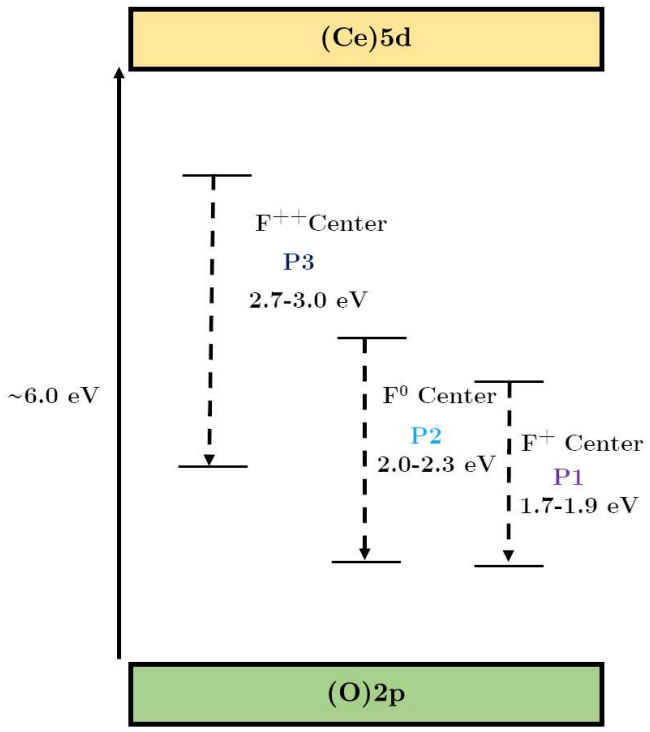

Figure 4. 9. Illustration of the radiative electronic transitions in CeO_2 with their corresponding CL peaks and F-centers.

The increase in oxygen vacancy concentration will lead to a change in the crystal field around the vacancy centers, in turn, resulting in the energy levels that favor emission in the infra-red region of the spectrum (beyond our experimental capability). Effectively, it could be manifested as CL intensity quenching. Moreover, it is possible that the increase in V_O concentration can facilitate energy transfer between the centers of luminescence as the separation between the centers decreases. When the sample is irradiated with an electron beam, the energy is transferred between the donors before it is absorbed by one center which acts as a non-radiative sink. [45] Since the polaron-vacancy association is plausible, it is likely to open up non-radiative decay paths through energy transfer between F centers. As the concentration increases beyond a critical value, energy transfer becomes efficient and leads to intensity quenching.

4.4 Conclusion

The oxygen vacancy related CL emission from pure CeO_2 heat-treated in different atmospheres was presented here. The relative concentration of different charge states of F centers depends on the oxygen partial pressure during sintering. We found that for low oxygen pressure, F^0 centers prevail over F^+ centers in CeO_2, while for high oxygen pressure F^+ centers are more dominant than F^0 centers. The dielectric polarizability of the CeO_2 crystal increases with decreasing oxygen partial pressure in the atmosphere of the heat-treatment, which confirms the continuous increase in defect concentration with decreasing oxygen partial pressure. However, the CL emission intensity does not follow this trend. Instead of a continuous increase, the CL emission reaches a maximum and starts decreasing with the increase in vacancy concentration. The polarons and associates of polarons with oxygen vacancies, such as $(Ce'_{Ce} - V_O^{\bullet\bullet} - Ce'_{Ce})^{\times}$, are demonstrated as the cause of the observed CL intensity quenching at higher oxygen vacancy concentrations. The demonstrated ability of CL spectroscopy to distinguish between various charge states of oxygen vacancies is useful for defect engineered property enhancements of CeO_2 related solid solutions.

5 Defect Induced Local Structure Distortion and Cathodoluminescence Quenching in Ceria

5.1 Introduction

Understanding the defect structure of CeO_2 is of fundamental importance with regards to its applications. The use of pure and doped CeO_2 is widespread, spanning all technologically relevant areas including energy production and conversion, three-way catalysts, [229,230] supercapacitors, [231,232] resistive switching devices for computation and data storage, [233,234] and bio medical applications. [41,235] All the functionalities associated with CeO_2 come from the fact that its defect chemistry can be readily modified by exposure to high temperature and low oxygen partial pressures or by extrinsic doping. The literature on correlation between the CeO_2 material chemistry and its functional properties are abundant. [236–238] Mostly, the transport properties are correlated with the material's chemistry and long range order (crystal structure). Often neglected the importance of local structure distortions induced by defects and its influence on macroscopic properties, such as electrical and optical properties.

Nonetheless, there are studies focused towards this direction employing techniques such as x-ray absorption fine structure spectroscopy (XAFS), Raman spectroscopy and Nuclear Magnetic Resonance (NMR) spectroscopy. [79,82] Element specific nature of XAFS helps to reveal the local structure around selected atoms and it can detect aperiodic distortions. [179] Thus, it is an apt tool to study defect associates (interaction between Ce^{3+}/ dopant ions and oxygen anions and vacancies) and lattice distortions. Many effects found in CeO_2 and its solid solutions as a resistance to radiation damage, [239] dependency of ionic conductivity on a dopant ionic radius [240] and phase transformations due to vacancy ordering [241–243] are explained as a result of the interaction between the cations and the oxygen vacancies. Ohashi et.al., [244] studied local structure around Ce and Gd in $Ce_{1-x}Gd_xO_{2-x/2}$ (x = 0–0.30) by EXAFS. They proposed the formation of defect associate consisting of two Gd^{3+} ions and one oxygen vacancy from the observed trend of decrease in the Gd-O interatomic distances. This defect association is pointed out as the reason for a decrease in the ionic conductivity in heavily doped $Ce_{1-x}Gd_xO_{2-x/2}$.

A number of studies showed the similar observation of M-O (M= Rare earth trivalent dopant) contraction and explained this trend on the basis of cluster formation of oxygen vacancy and

dopants. [182,245–250] The study of local structure of $Ce_{0.8}Gd_{0.2}O_{1.9}$ nanocrystalline films, by Kossoy et.al., [251] showed the importance of local structural distortion towards macroscopic properties (chemical strain effect). Giannici et.al., [250] traced out the importance of local structure distortion on transport properties in doped ceria. They attributed the positive influence of Sm doping on oxide ion conductivity to its ability to repel oxygen vacancies from Sm^{3+} and local disorder around the dopant. A comprehensive review on this topic can be found in references by Coduri et al. [237] and Schmitt et al. [179]

The cathodoluminescence (CL) spectroscopy has been employed as a tool to study point defects in Y doped ZrO_2 and mechanical stress originating from oxygen vacancies in silica glass. The importance of surroundings of vacancy sites to the emission has been described therein. Considering this ability of CL, it is possible to extract insight from the emission spectra about the neighborhood of emission centers. Previously, we showed that the CL behavior of pure CeO_2 is not trivial. With an increase in oxygen vacancy concentration the CL emission increases in intensity, reaches a maximum and then starts decreasing. The observed quenching was explained on the basis of association between polarons and oxygen vacancies. [252] Here we attempt to present a detailed picture of CL behavior of La doped CeO_2 and its relation to local structure distortions. Since La is always in 3+ oxidation state and have an ionic radius similar to Ce^{4+}, La doped CeO_2 will be a good approximation to the undoped ceria and its defect structures. Furthermore, this way we can precisely control the oxygen vacancy concentration and explore the CeO_2 lattice with much higher V_O concentration.

Here we attempted to upgrade the observation of CL quenching for higher oxygen vacancy concentrations as seen in undoped reduced CeO_2 and provide an explanation based on polaron and vacancy associates. We used K-Edge EXAFS analysis for both Ce and La cations to elucidate the local structure around the cations. Particularly, we used K-Edge EXAFS analysis for both Ce and La, so that the local structure is determined with better accuracy. The Ce L_3-Edge EXAFS analysis is accompanied by limitations due to a short data range and a small energy separation between L_2 and L_3-edges. Moreover, a multi-electron excitation [253] and final state mixed valence behavior [254] pose another threat to L_3-EXAFS analysis. [255] Our results point out that the non-radiative recombination pathways in CeO_2 emission depends on the geometry of defect associates. The CL analysis as a facile method to understand the defect structures in CeO_2

is demonstrated and the emission dependence on local structure distortions and defect associates is elucidated.

5.2 Methods

The $Ce_{1-x}La_xO_{2-x/2}$ powdered materials were synthesized by using a chemical co-precipitation technique. [256–258] High purity $Ce(NO_3)_3.6H_2O$ (99.99%) and $La(NO_3)_3.6H_2O$ (99.99%), purchased from Sigma Aldrich, were used as precursors without any further purification. The requisite amount of precursors was dissolved in distilled water separately to obtain a final concentration of 0.2M. Afterward, both the precursors were mixed and stirred in a beaker to get a homogeneous clear solution. The solution was precipitated with dropwise addition of aqueous ammonia until the solution pH reached ~8. The chosen pH ~ 8 is reported previously in literature as best for co-precipitation technique[1], validation for such a choice was proved through thermal and phase analyses. In the attained yellow solution, precipitates were quite visible and filtered out with centrifugation followed by washing with distilled water and ethanol. Finally, the precipitates were dried at 100^{o}C and calcined at 550°C for 2 hours in an air atmosphere to attain mixed oxide nanoparticles. The rate of heating and cooling was fixed at 5°C/min. Later these samples were pelletized and sintered at a heating and cooling rate of 8°C/min in an oxygen atmosphere for 10 hours at 1450°C.

A Rigaku MiniFlex diffractometer was used for the XRD measurements. Ni filtered Cu K_α radiation, steps of 0.05^o with collection time of 1s per step were used to acquire the data. XRD was analyzed by an X'Pert HighScore software.

Microstructural images and CL spectra were taken by a field-emission gun scanning electron microscope (SEM JEOLJSM 7100 TTLS). For the CL measurements, the same experimental conditions were applied for all samples to avoid introducing additional variables. The acceleration voltage and the beam current were set for all experiments at 25 keV and 2nA, respectively. The CL spectra were acquired in the wavelength region 300 nm to 800 nm. The reported CL spectra have been corrected by grating response and detector response in the wavelength region 350nm to 750nm. The microscope was equipped with a CL device (GATAN MonoCL4) consisting of a parabolic mirror and a bundle of optical fibers, used to collect and to

focus the electron-stimulated luminescence emitted by the sample into a monochromator with 2nm spectral resolution.

A Gaussian deconvolution procedure is required to reveal the true nature of the emission spectra of the La-doped CeO_2. The fitting procedure is carried out with a Levenberg-Marquadt algorithm implementation of the lmfit package. [259]

We performed the Ce and La K-edge EXAFS measurements on a set of the high purity La dopped CeO_2 nanopowder samples with different concentrations of La in the range form 0.5 mol% to 30 mol%, sintered at 1450°C for 8 hours in oxygen. The spectra were measured at room temperature in transmission detection mode. The samples for EXAFS analysis were prepared in the form of homogeneous pellets, pressed from micronized CeO_2-based powder mixed with boron nitride (BN) powder, with the total absorption thickness (μd) of about 2.5 above the Ce K-edge (40444 eV) or La K-edge (38 899 eV).

A Si (311) double crystal monochromator was used with energy resolution of about 3 eV at 40 keV. The beam size on the sample was 1.5 mm horizontally and 0.2 mm vertically. Higher-order harmonics were effectively eliminated by a flat mirror. The intensity of the monochromatic X-ray beam was measured by three consecutive ionization detectors, filled with appropriate krypton and argon gas mixtures to obtain 15% absorption in the first and 70% in the second and third detector. The absorption spectra were measured in the energy region from -150 eV to +1000 eV relative to the investigated K-edge in continuous fast (3 min) scans and re-binned to equidistant energy steps of 0.5 eV in the XANES region and equidistant k steps of 0.05 $Å^{-1}$ in EXAFS region. We performed three to five repetitions of the same scan to improve signal to noise ratio. The exact energy calibration was established with simultaneous absorption measurement on a CeO_2 pellet placed between second and third ionization detector. Absolute energy reproducibility of the measured spectra was ±0.05 eV. The quantitative analysis of EXAFS spectra was performed with the Demeter (IFEFFIT) program package. [190]

5.3 Results and Discussion

Figure 5.1 shows the XRD patterns for $Ce_{1-x}La_xO_{2-x/2}$. All materials crystallize in the fluorite structure (Fm-3m) as described in ICSD #88759. According to Horlait et al. [260] the fluorite

structure of $Ce_{1-x}La_xO_{2-x/2}$ is retained up to x=0.6. The XRD patterns confirmed that all the compositions are single phase. No new peaks emerged, instead lattice expansion is evident as the peaks are shifted to lower 2θ direction. The larger size of La^{3+} cations (1.16Å) replacing smaller Ce^{4+} (0.97 Å) led to the expansion of the lattice. The evolution of the lattice parameter as a function of doping level is shown in Figure 5.2.

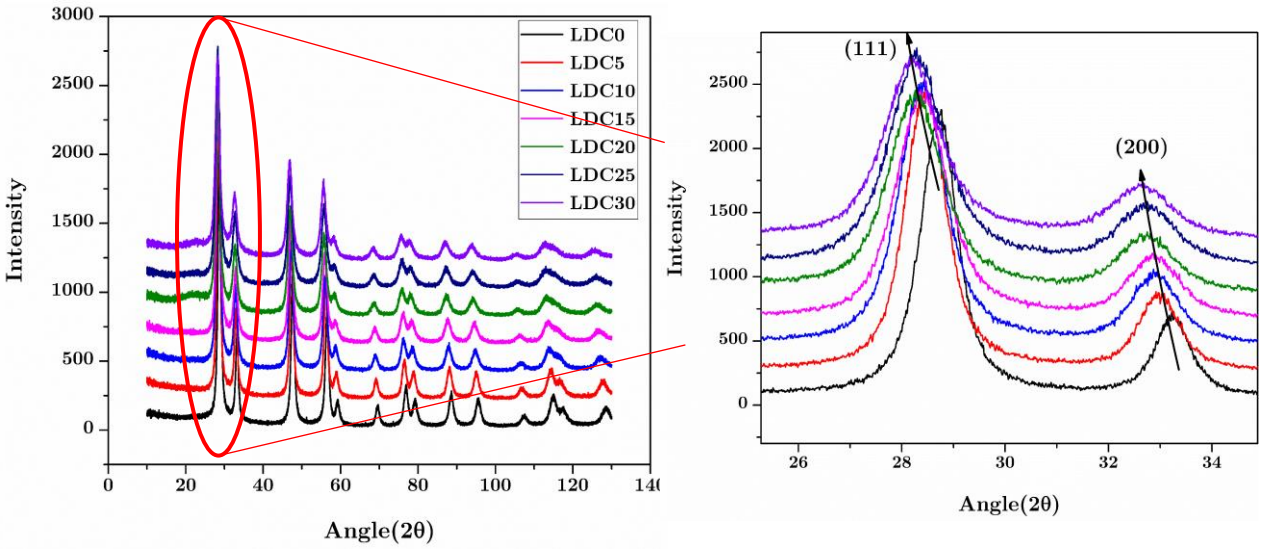

Figure 5. 1. XRD patterns obtained for $Ce_{1-x}La_xO_{2-x/2}$. The lattice expansion is shown on the right panel.

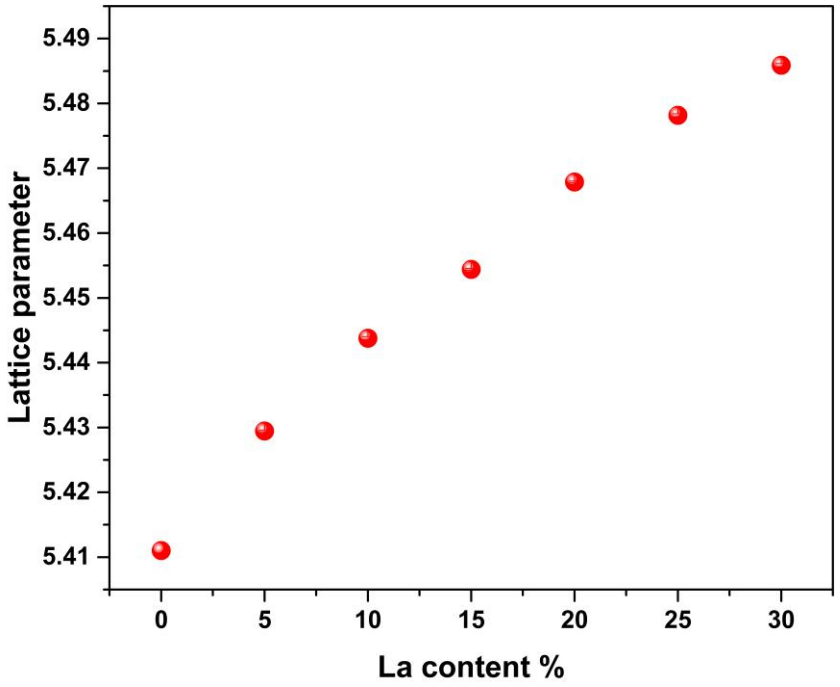

Figure 5. 2. Lattice parameter of LDC samples as a function of La content. Uncertainty from Rietveld refinement is about 10^{-4} Å.

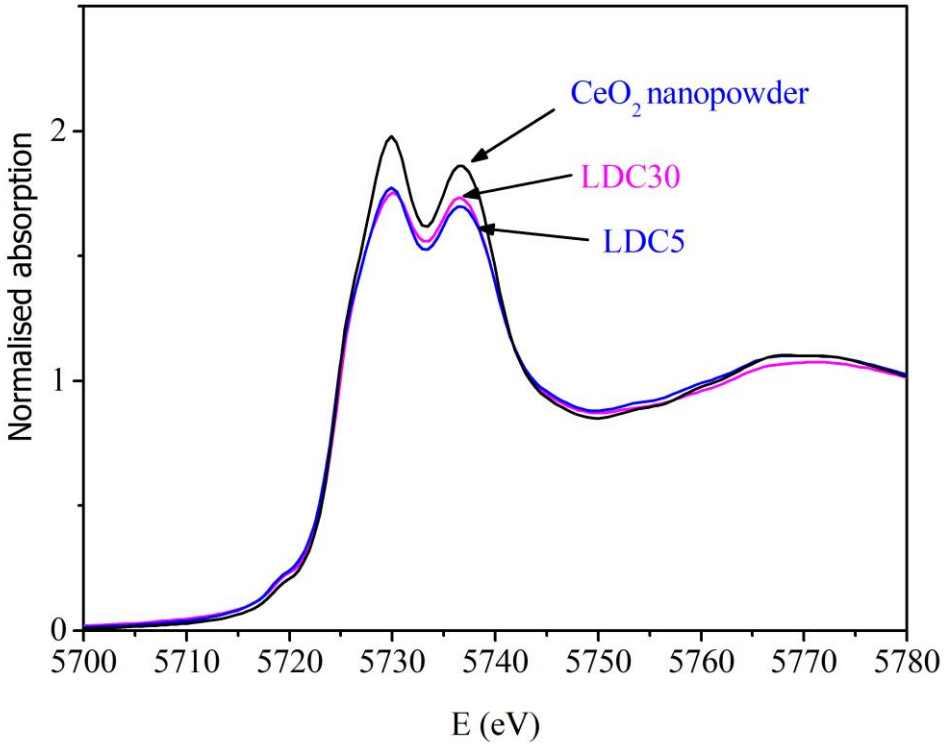

Figure 5. 3. Ce L_3-edge XANES spectra for pure CeO_2 and LDC5 and LDC30.

Ce L_3-edge XANES spectra are shown in Figure 5.3 for the pure and La-doped CeO_2. The relative amount of Ce^{4+} and Ce^{3+} were determined from the XANES spectra. A characteristic peak at 5726 eV reveals the presence of Ce^{3+}, while the presence of Ce^{4+} can be detected from two characteristic peaks at 5730 eV and 5736 eV. Pure CeO_2 and LDC showed these two characteristic Ce^{4+}peaks. But, the intensity is lower for LDC samples compared to pure CeO_2, which could be an indication of oxygen vacancies. [261] A detailed comparison of the XANES spectra showed tiny differences in the pre-edge region at 5726 eV between the LDC and pure CeO_2samples.This can be attributed to the presence of small amount of Ce^{3+}. A linear combination analysis is performed for the quantification of Ce^{3+}. It is found that the concentration of Ce^{3+} in LDC5 is 2.4(1) %, while for LDC30 it was beyond the detection limit of the method (< 0.2%).

The Ce and La K-edge EXAFS analysis was used to determine an average local structure around the Ce and La cations in the undoped and La-doped CeO_2 with different La loadings in the range from 5 to 30 %. We investigated the effect of doping on the changes in local structure around the Ce and La cations. In the Fourier transform magnitude of the EXAFS spectra the contributions of photoelectron scattering on the nearest shells of neighbours around the Ce (Figure. 5.4) and La atoms (Figure. 5.5) are observed in the R range up to about 4 Å. In all La-doped CeO_2, the average local structure around the Ce or La cations are very similar to that observed around the Ce cations in the undoped crystalline CeO_2. The peak in the R range between 1 Å and 2.2 Å can be attributed to photoelectron backscattering on the nearest oxygen neighbours around the Ce or La atoms. The strong peak in the R range between 3 Å and 4 Å represents contributions from more distant Ce or La coordination shells characteristic for the CeO_2 crystal structure. More detailed qualitative comparisons of the FT spectra reveal the difference in average Ce and La neighbourhoods between the samples with different La loadings. The intensity of both peaks in the FT spectra decreases with higher La loading and smaller shifts in position of the two peaks are visible.

The quantitative EXAFS analysis is performed to precisely determine the differences in the local structure around the Ce and La cations as a function of La doping. As indicated by the qualitative comparison of EXAFS spectra and by the XRD data of these samples, we can expect that the Ce and La cations occupy same crystallographic sites in the crystal structure of CeO_2, and the

observed differences can be attributed to small local distortions and different occupancies of neighbour shells around both atoms at these sites.

The Ce and La EXAFS models are based on the XRD data of the crystalline CeO_2 with the fluorite cubic structure (*Fm-3m*) and the lattice parameter 5.411 Å. [243] In this crystal structure, the Ce atoms are coordinated with 8 oxygen neighbours at 2.343 Å in the first coordination shell and 12 Ce neighbours at 3.826 Å and 24 oxygen neighbours at 4.487 Å in the second and third coordination shells. The La atoms, located on Ce sites in the CeO_2 crystal structure, have the same coordination as the Ce atoms.

Structural parameters of the average local Ce and La neighbourhood (type and average number of neighbours, the radii and Debye-Waller factor of neighbour shells) are quantitatively resolved from the EXAFS spectra by comparing the measured EXAFS signal with an EXAFS model signal, constructed *ab initio* with the FEFF6 program code. [262] The atomic species of neighbours are identified in the fit by their specific scattering factor and phase shift. However, it should be pointed out that with the EXAFS analysis it is not possible to distinguish between neighbours that differ only for 1 in atomic number, i.e. we cannot distinguish between Ce and La neighbours since their scattering factor and phase shifts are too similar.

The contributions of the three nearest shells of neighbours are included in the EXAFS models. In addition, a distortion of the nearest oxygen shell and the Ce shell of neighbours is allowed during the fit by introducing two distances to the nearest oxygen neighbours and two distances to Ce neighbours. In total, 5 single scattering paths and all multiple scattering paths in the R range up to 4.0 Å are included in the fit. Three variable parameters for each shell of neighbours are introduced in the model: the relative shell coordination number (N_{rel}), the distance (R) and the Debye-Waller factor (σ^2). In addition, a common shift of energy origin ΔE_o is also allowed to vary. The amplitude-reduction factor S_0^2 is kept fixed at the value of 0.99.

The Ce K-edge EXAFS spectrum of the reference CeO_2 sample is used to calibrate the basic model without distortions. A very good fit is obtained in the *k*-range of 3.8–13 $Å^{-1}$ and R range of 1.3 to 4.3 Å. Contributions of nearest three shells of neighbours are detected in the EXAFS spectrum: 8 Ce neighbours at 2.33 Å, 12 Ce neighbours at 3.84 Å and a weak contribution of 24 oxygen atoms at 4.49 Å.

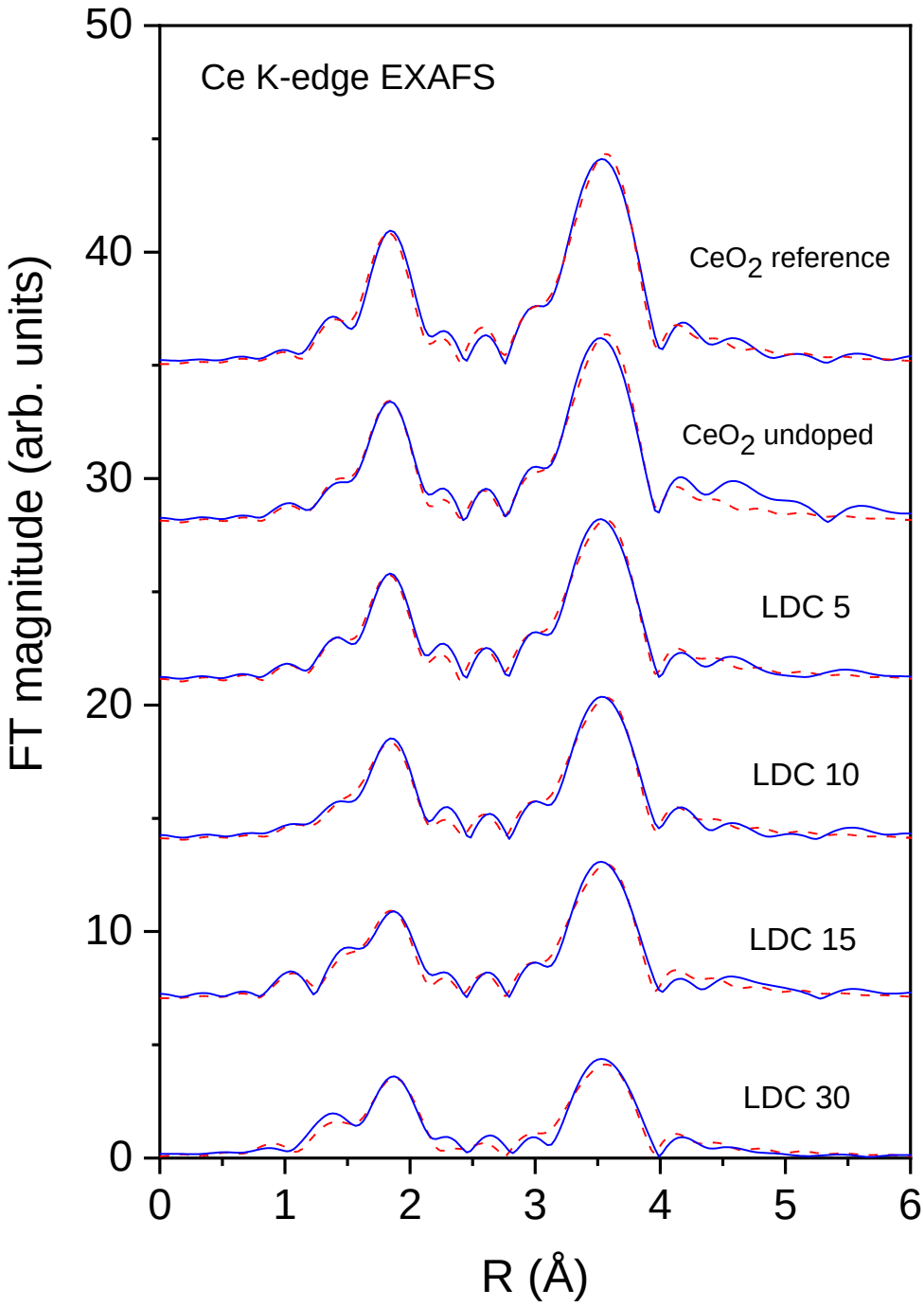

Figure 5. 4. Fourier transform magnitude of k^3-weighted Ce K-edge EXAFS spectra of the undoped and La dopped CeO_2 nano powder samples with different concentrations of La in the range form 5 mol % to 30 mol%. Spectrum of standard CeO_2 crystalline sample with fluorite cubic structure (F m -3 m) with lattice parameter 5.423 Å is shown for comparison. Experiment – (blue solid line); EXAFS model -- (red line), calculated in the k range of 3.8–13 $Å^{-1}$ and R range of 1.3 to 4.3 Å.

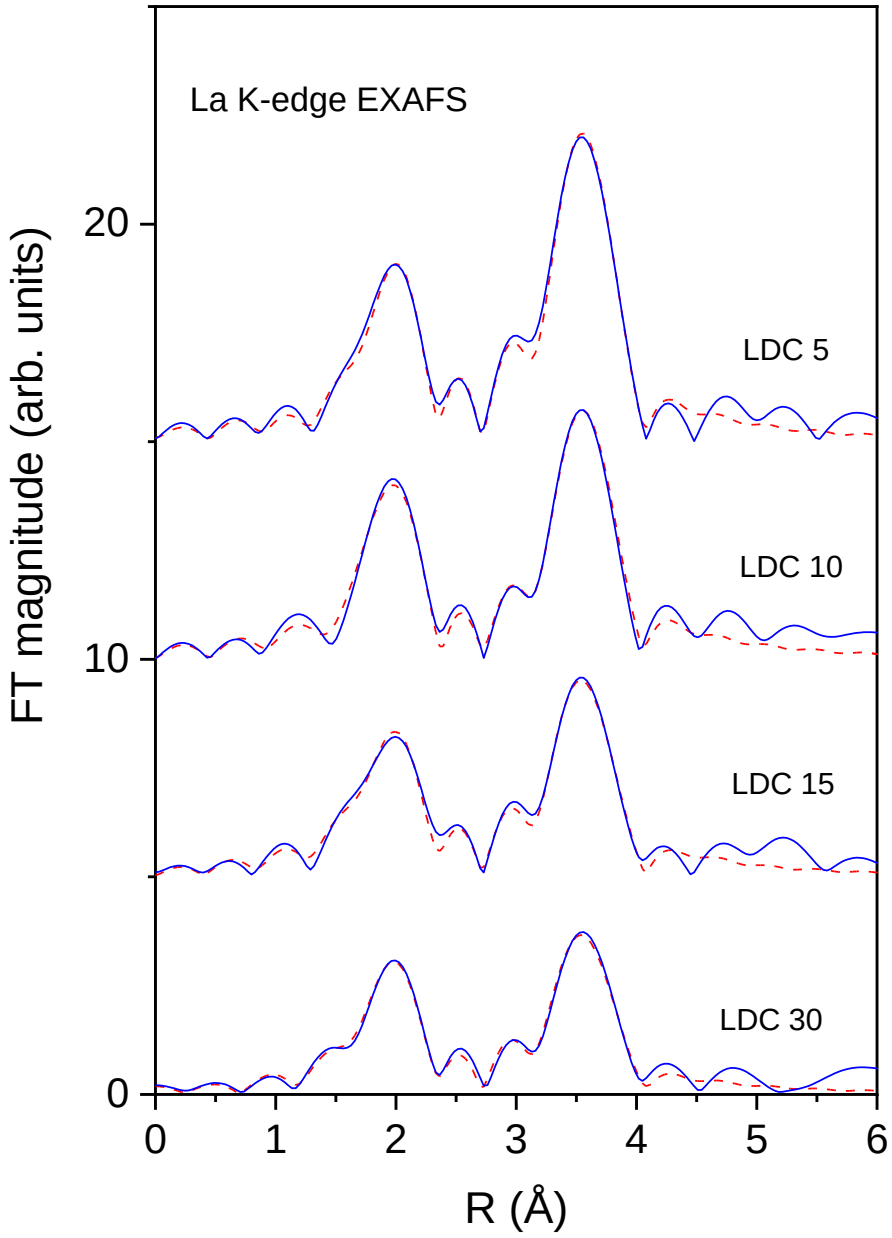

Figure 5. 5. Fourier transform magnitude of k^3-weighted La K-edge EXAFS spectra of the La dopped CeO_2 nano powder samples with different concentrations of La in the range form 5 mol % to 30 mol%. Experiment – (blue solid line); EXAFS model -- (red line), calculated in the k range of 4.5–12 $Å^{-1}$ and R range of 1.3 to 4.5 Å.

Table 1. Parameters of the nearest coordination shells around Ce cations in the undoped and La doped CeO_2 samples: Coordination number of neighbour atoms in crystalline sample (N), average relative occupancy of neighbour atoms (N_{rel}), distance (R), and Debye-Waller factor (σ^2). Uncertainty of the last digit is given in parentheses. A best fit is obtained with the amplitude reduction factor S_0^2=0.99 and the shift of the energy origin ΔE_o = -1 eV. The R-factor (quality of fit parameter) is listed in the last column.

Ce neighbor	$N*N_{rel}$	R(Å)	σ^2(Å^2)	R-factor
		Standard CeO_2 crystalline sample		
O	8 * 1.1(1)	2.331(6)	0.008(1)	
Ce	12 * 0.9(1)	3.839(4)	0.0042(4)	0.00023
O	24 * 0.9(1)	4.49(2)	0.007(2)	
		Undoped CeO_2		
O	8 * 1.1(1)	2.331(6)	0.008(1)	
Ce	12 * 0.76(9)	3.839(4)	0.0042(4)	0.00023
O	24 * 0.76(9)	4.49(2)	0.007(2)	
		5 mol% La doped CeO_2		
O	8 * 0.05(1)	2.19(3)	0.008(1)	
O	8 * 0.95(8)	2.33(1)	0.008(1)	
Ce	12 * 0.02(4)	3.66(2)	0.0038(4)	0.00020
Ce	12 * 0.61(7)	3.84(1)	0.0038(4)	
O	24 * 0.61(7)	4.49(2)	0.007(2)	

Table 1. (Contd.)

Ce neighbor	$N*N_{rel}$	R(Å)	$\sigma^2(Å^2)$	R-factor
		10 mol% La doped CeO_2		
O	8 * 0.13(1)	2.18(3)	0.007(1)	
O	8 * 0.87(8)	2.33(1)	0.007(1)	
Ce	12 * 0.06(4)	3.67(2)	0.0038(4)	0.00037
Ce	12 * 0.58(7)	3.84(1)	0.0038(4)	
O	24 * 0.58(7)	4.49(2)	0.007(2)	
		15 mol% La doped CeO_2		
O	8 * 0.35(1)	2.22(3)	0.005(1)	
O	8 * 0.65(8)	2.36(1)	0.005(1)	
Ce	12 * 0.05(4)	3.67(2)	0.0036(4)	0.00046
Ce	12 * 0.53(7)	3.84(1)	0.0036(4)	
O	24 * 0.53(7)	4.49(2)	0.007(2)	
		30 mol% La doped CeO_2		
O	8 * 0.27(1)	2.17(6)	0.006(1)	
O	8 * 0.73(8)	2.33(1)	0.006(1)	
Ce	12 * 0.06(4)	3.68(2)	0.004(1)	0.00148
Ce	12 * 0.39(7)	3.84(1)	0.004(1)	
O	24 * 0.39(7)	4.49(2)	0.007(2)	

To detect small differences in local structure around Ce and La cations as a function of La doping and to minimise uncertainties of the fitting parameters due to high correlations between them in the fit of individual spectra, parallel fits of Ce EXAFS spectra and separate parallel fits of La EXAFS spectra were performed. For the fits some parameters were constrained to common values. For Ce EXAFS spectra the fitting range in the *k*-interval was 3.8 $Å^{-1}$ –13 $Å^{-1}$ and in the R range from 1.3 Å to 4.3 Å. For La EXAFS spectra the fitting range was 4.5–12 $Å^{-1}$ in k space and 1.3 to 4.5 Å in R space. Very good fits were obtained for all spectra (Figure 5.4 and 5.5). A complete list of the best fit parameters is presented in Tables 1 and 2. The uncertainties of the best fit parameters N_{rel} and σ^2 of more distant coordination shells are relatively large due to correlations between these parameters.

Ce EXAFS results of the undoped CeO_2 samples are consistent with the XRD crystalline data and EXAFS results for bulk CeO_2. No distortion of first or second coordination shell is detected. The Ce-O and Ce-Ce distances and Debye-Waller factors of these coordination shells are same as in the reference CeO_2 crystalline material. The occupancy of the nearest oxygen shell is full. No oxygen vacancies are detected in the first coordination shell within error bars. The relative coordination numbers of Ce and O atoms in the second and third coordination shell are 20% lower than in the bulk CeO_2, which can be attributed to small size of CeO_2 nanoparticles in the undoped CeO_2 sample or presence of vacancies on the Ce neighbor sites. The signal of oxygen in the third coordination shell is very weak, so it is difficult to prove eventual oxygen vacancies in the third shell. (Number of oxygen in the third shell in the fit is bound to number of Ce neighbours in second shell).

In all La-doped CeO_2 samples, the Ce EXAFS results show a distortion of first oxygen shell and also more distant Ce coordination shell around Ce atoms (Table 1). Besides the Ce-O distance of 2.33 Å that were also found in the bulk CeO_2 crystal, a small relative amount of oxygen neighbours is found at a shorter Ce-O distance of 2.19 Å. In the second coordination sphere we detected the Ce neighbours at 3.84 Å, as in CeO_2 reference, and a small relative amount of Ce atoms at a shorter distance of 3.67 Å. A relative number of oxygen at shorter distance in the first shell and the Ce neighbours in the second shell correlates with amount of La atoms in the structure: at larger La doping, the fraction of oxygen and Ce neighbours at shorter distance

increases. Besides that, the total occupancy of the Ce coordination shell decreases with the higher La doping. At 30% La doping (LDC 30) there are only about 45% Ce neighbours present.

The La EXAFS results show that the La cations are occupying the Ce crystallographic positions in the CeO_2 crystal. The La-O and La-Ce distances are almost identical to the Ce-O and Ce-Ce distances in the bulk CeO_2 crystal structure. There are no distortions of local neighbourhood of La cations. The total occupancy of the Ce coordination shell around the La cations decreases with higher La doping in the same way as around Ce atoms. At 30% La doping (LDC30) there are only about 40% Ce neighbours present in the second coordination shell of La. In addition, a small decrease (10% – 20%) of oxygen neighbours around La cations is indicated at highest La loadings.

The reduced relative coordination numbers of Ce atoms in the second coordination shell can be attributed to a small size of CeO_2 nanoparticles in the La-doped CeO_2 samples. On the other hand, the decreased number of oxygen neighbours in the first coordination shell around La atoms can be ascribed to oxygen vacancies around La cations at high La doping.

Table 2. Parameters of the nearest coordination shells around La cations in the La doped CeO_2 samples: Coordination number of neighbour atoms in crystalline CeO_2 sample (N), average relative occupancy of neighbor atoms (N_{rel}), distance (R), and Debye-Waller factor (σ^2). Uncertainty of the last digit is given in parentheses. A best fit is obtained with the amplitude reduction factor S_0^2=0.99 and the shift of the energy origin ΔE_o = -4 eV. The R-factor (quality of fit parameter) is listed in the last column.

La neighbor	$N*N_{rel}$	R(Å)	σ^2(Å^2)	R-factor
		5 mol% La doped CeO_2		
O	8 * 1.0(1)	2.46(1)	0.010(1)	
Ce	12 * 0.78(5)	3.87(1)	0.006(4)	0.0010
O	24 * 0.78(5)	4.54(2)	0.009(2)	
		10 mol% La doped CeO_2		
O	8 * 1.0(1)	2.46(1)	0.007(1)	
Ce	12 * 0.63(5)	3.87(1)	0.006(4)	0.0003
O	24 * 0.63(5)	4.54(2)	0.009(2)	
		15 mol% La doped CeO_2		
O	8 * 0.9(1)	2.46(1)	0.010(1)	
Ce	12 * 0.49(4)	3.87(1)	0.006(4)	0.0012
O	24 * 0.49(4)	4.54(2)	0.009(2)	
		30 mol% La doped CeO_2		
O	8 * 0.8(1)	2.46(1)	0.010(1)	
Ce	12 * 0.40(4)	3.87(1)	0.006(4)	0.0010
O	24 * 0.40(4)	4.54(2)	0.009(2)	

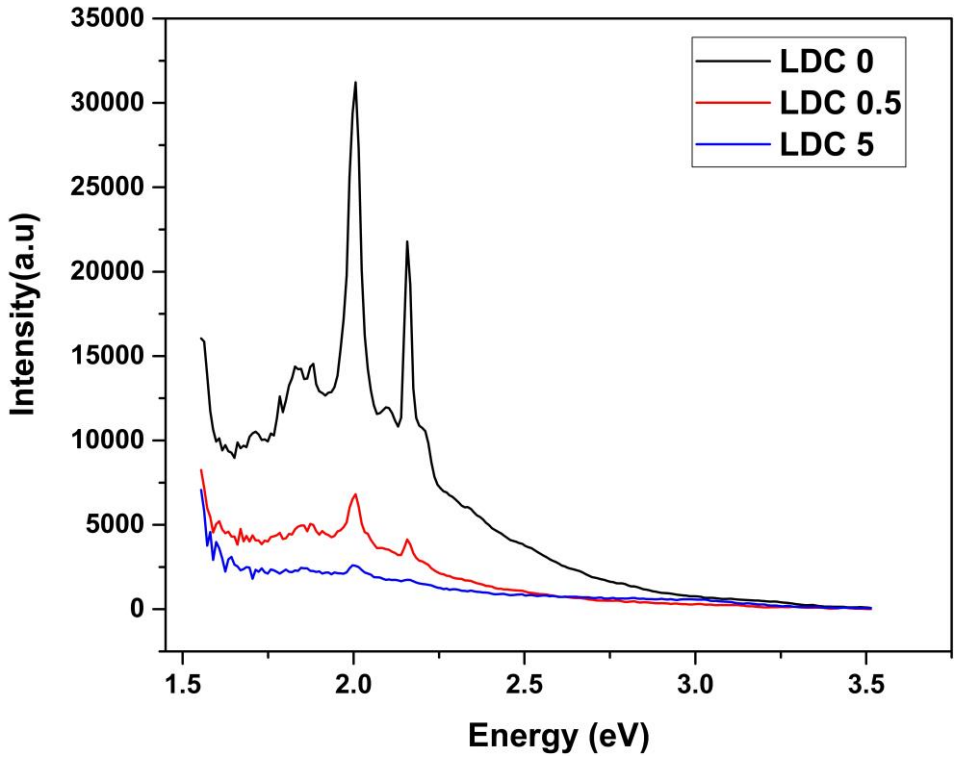

Figure 5. 6. Cathodoluminescence emission of pure CeO_2 and La doped CeO_2 (LDC). Emission intensity quenching as a function of dopant concentration is evident.

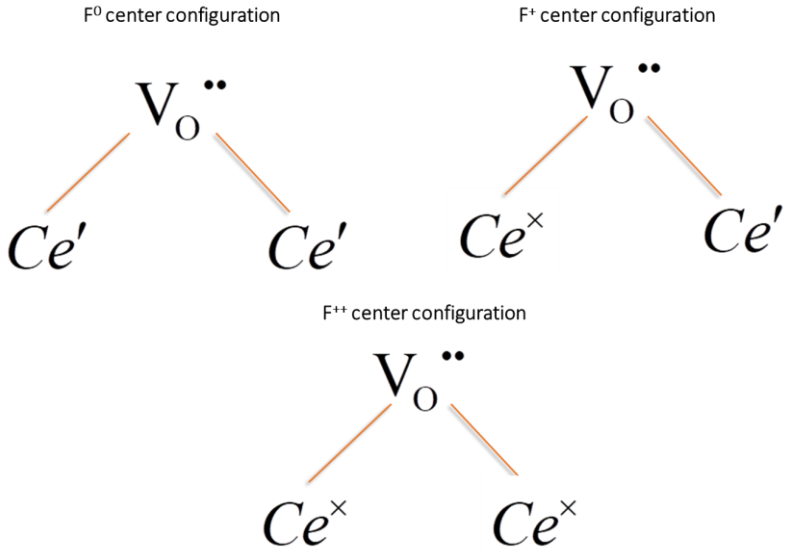

Figure 5. 7. F center configurations involving Ce^{3+} (Ce'), Ce^{4+} $(Ce^{\times})$ and doubly charged oxygen vacancy $(V_O^{\bullet\bullet})$. Note that the Ce^{3+} ions further from $V_O^{\bullet\bullet}$ in F^{++} configuration is not shown.

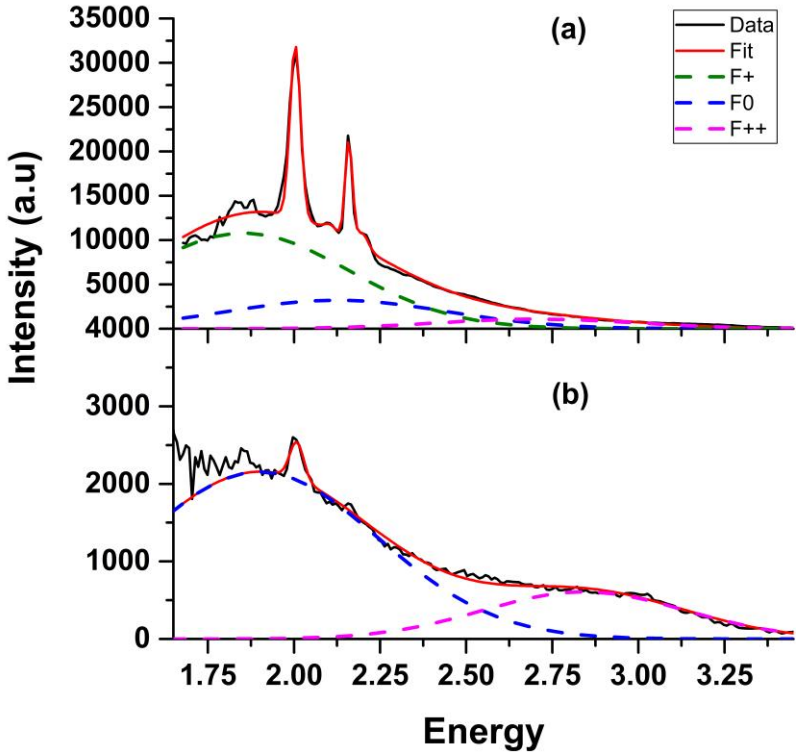

Figure 5. 8. CL spectra and Gaussian fitting of pure (a) CeO_2 and (b) LDC5 samples. The sub bands corresponding to F^+ (green), F^0 (blue) and F^{++} (magenta) centers are shown. The relative population of F centers are calculated from the ratio of integrated area of sub bands to the overall area under the curve for each sample. As the concentration of La increases F^0 becomes the dominant luminescence center.

The CL emission of pure and La-doped CeO_2 measured at room temperature is depicted in Figure 5.4. Spectral deconvolution for pure CeO_2 using Gaussian profiles requires broad peaks centered at 1.7-1.9, 2.0-2.3, 2.7-3.0 eV and sharp peaks at 2, and 2.15 eV (Figure 5.8 (a)). The La-doped CeO_2 spectra are deconvoluted by bands centered at ~1.9-2.0, and 2.8-3.0 eV (Figure 5.8 (b)).

According to Costantini et al. [211] the CL emission in CeO_2 (visible region) originates from Ce^{3+} and oxygen vacancies in different configurations (see Figure 5.7). They identified these different Ce^{3+} configurations as different F centers analogous to classical oxygen vacancy (V_O) centers. Based on this, we have assigned the CL emission from pure CeO_2, the broad bands

centered at ~1.7-1.9, 2.0-2.3, and 2.7-3.0 eV, to Ce^{3+} and oxygen vacancies forming F centers. [252] Two additional narrow peaks at ~2.00 and 2.15 eV were assigned to Sm^{3+} impurities similarly as in Balestrieri et al. [210] It is known from the photoluminescence (PL) studies that Sm^{3+} gives emissions corresponding to the transitions $^4G_{5/2}$ to $^6H_{5/2}$ and $^4G_{5/2}$ to $^6H_{7/2}$ within the range 550 nm (2.25 eV) to 800 nm (1.54 eV). The presence of 0.4 mg/kg of Sm impurity has been confirmed in our starting $Ce(NO_3)_3$ precursor by an inductively coupled plasma mass spectrometry (ICPMS).

It was shown that such a description of the F centers in CeO_2 is adequate to explain the CL behavior as a function of oxygen vacancy concentration. We showed that in pure CeO_2 the relative concentration (population) of F^+ and F^0 centers vary as a function of oxygen partial pressure during sintering. Based on the calculations [50,59] we demonstrated that for a high oxygen partial pressure, the F^+ centers are found to be prevalent, whereas a low oxygen partial pressure favored the F^0 centers. It was confirmed that the dominance of F^+ centers give rise to the high intensity CL emission of pure CeO_2. On the other hand, the prevalence of F^0 centers (as a result of reduction) results in the CL emission intensity quenching.

As shown in Figure 5.6 the CL measurements of the CeO_2 samples with a different concentration of La showed that the emission intensity decreases as a function of the concentration. Interestingly, also the emission of Sm impurities is quenched. With addition of 5 mol% La (LDC5), the intensity drops to a minimum and after that it slightly changes in intensity (LDC 10 through LDC 30). In order to understand the variation of F center population as a result of La doping the CL spectra are deconvoluted using Gaussian sub bands (Figure 5.8 (a, b)). The description of the emission bands observed at ~2eV and ~3 eV varies in literature. Based on PL data some assign the 2 eV band to the F^0 centers [263] while others attribute it to $5d^1 \rightarrow 4f^1$ transitions of Ce^{3+} ions in ceria. [212] Here we adopt the description of the F centers in ceria proposed by Costantini et al. [211] According to them, the band at ~2eV and ~3eV are assigned to the F^0 and F^{++} centers, respectively. From the Gaussian deconvolution we see that in the case of pure CeO_2 (LDC0) F^+ centers were the dominant species. But for LDC 5 (Figure 5.8 (b)) it was found that F^0 is the prominent component. Since F^0 configuration is not as favorable as F^+ centers towards CL emission in CeO_2, the emission intensity is quenched upon La doping. This

goes in line with our finding of CL intensity quenching in the case of reduced ceria as described above.

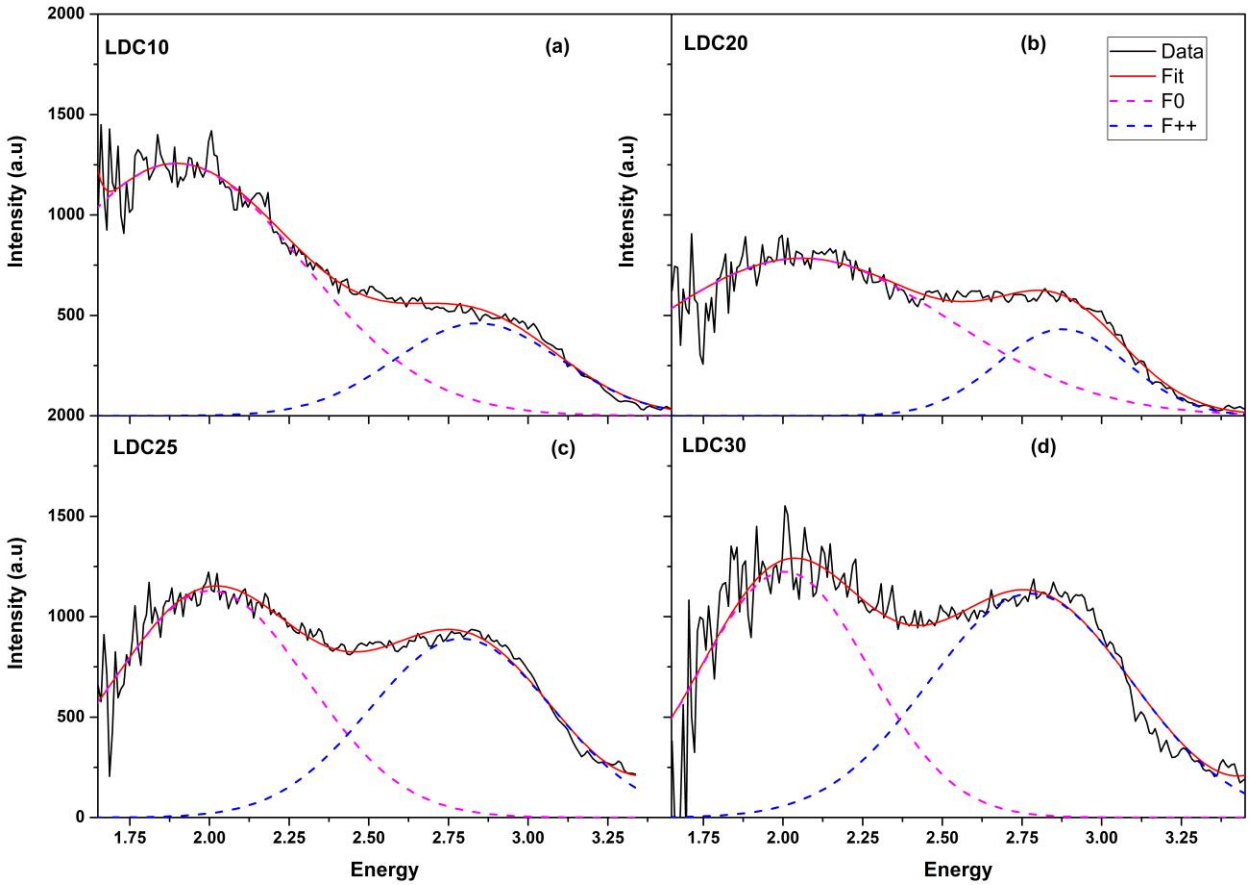

Figure 5. 9. Gaussian deconvolution of Cathodoluminescence spectra for (a) LDC10, (b) LDC20, (c) LDC 25 and (d) LDC 30. The principal components related to oxygen vacancies at around 1.9 eV and 3.0 eV are identified as F^0 and F^{++} centers respectively.

Further analysis on the spectral morphology of LDC samples (Figure 5.9 (a-d)) revealed the subtle variation of F center population. For this purpose, we considered the ratio of F^0 to F^{++} sub band areas ($A = F^0/F^{++}$). This is plotted in Figure 5.10 as a function of La doping. From this we see that the share of F^0 population declines with increase in La content. It is quite intuitive to understand this trend, because at higher La doping the Ce^{3+} in the F^0 configuration could be replaced by La^{3+} ions. Thus F^0 population should decrease with increasing La concentration. The

formation/presence of Ce^{3+} upon La doping was reported in literature [264,265] and our XANES analysis showed that LDC 5 has 2.4% Ce^{3+} ions present in it. But for LDC 30 Ce^{3+} concentration was beyond the detection limit of the technique (<0.2%). According to Rocha et al. [266] doping CeO_2 with lanthanum can result in La f-states induced Ce^{3+} to Ce^{4+} oxidation due to the Fermi level shifting. Moreover, Loche et al. [267] also showed that Ce^{3+} becomes undetectable in 7.5 mol% La doped CeO_2. Based on these facts we suggest that at high doping of lanthanum, Ce^{3+} ions in F^0 configuration are replaced by La^{3+} and hence the decline of the CL ratio A. This is supported by the local structure analysis by EXAFS around La described in the previous section. The quenching of Sm^{3+}emission found for increased La doping, could be facilitated by resonant energy transfer between the identical centers of luminescence. When the sample is irradiated with an electron beam, the energy is transferred between the donors before it is absorbed by one center which acts as a non-radiative sink. [45]

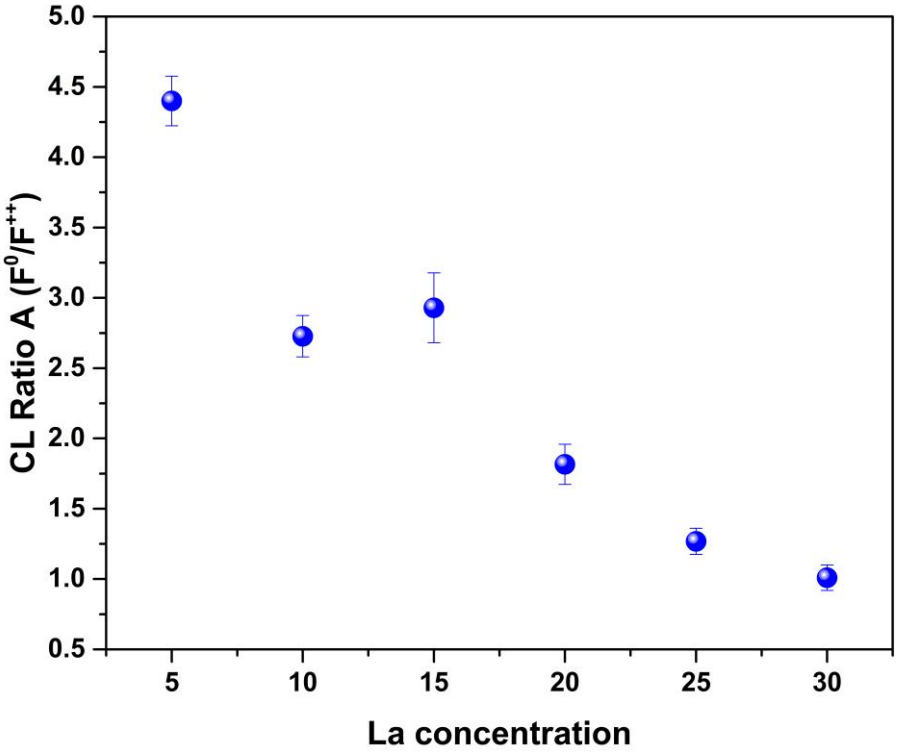

Figure 5. 10. The CL ratio A (F^0/F^{++}) as a function of La doping, where A is defined as the ratio of sub band areas corresponding to F^0 and F^{++} centers.

The local structure distortion as the result of La doping can be identified from the Ce-O and La-O bond lengths obtained from the EXAFS analysis (Table 1 and 2). If we compare the Ce-O distances in La-doped and undoped CeO_2, we see that a main part of O neighbors in doped CeO_2 remains at the same distance as in undoped CeO_2 (2.331(6) Å), and there is a small fraction of O neighbours that are at shorter distance 2.19(3) Å. This indicates the local distortion of CeO_2 crystal structure due to the La dopants. Some Ce sites are also distorted (not all) that is why the average numbers of neighbors are not integer numbers. With higher La doping, it is seen that the number of oxygen atoms at the shorter distance increases (also there are more distorted Ce sites). A general consensus [1,268] from the EXAFS analysis on trivalent (M^{3+}) rare earth doped ceria solid solutions is that for larger dopants ($R_{Shannon} \geq 105pm$) the interatomic distances are as follows: Ce-O < M^{3+}-O whereas, Ce-Ce > M^{3+}-Ce. The interpretation is that the fluorite symmetry is broken on the local scale and the strong distortion is found in the neighborhood of dopant ions. This contraction of bond lengths was explained by the contraction of 6 oxygen atoms in the next nearest neighbor (2NN) shell of the vacancy. [269] Later Koettgen et al. [270] correlated the decrease in average coordination number around Ce or M^{3+}-dopant with the decrease in the distances between oxygen and cation atoms. The local distortions are substantial in the first shell than the second shell.

Yashima et al. [271] proposed an ion packing model associated with defect clustering to describe local structures of zirconia solid solutions. According to them, the state of ion packing should depend on the local configurations of cation and anion vacancies. Also Dexpert-Ghys et al. [272] suggested that the coordination number (CN) of cations is controlled by the number of oxygen vacancies. Later Gianicci et al. [250] adopted this model to describe the defect clustering in rare earth doped CeO_2. They used statistical lattice simulations to calculate the average coordination number around Ce and M (rare earth) atoms in the first and second coordination shell and correlated these with the occurrence of vacancy and cation clusters (Figure 5.11). They also used the distances such as, M-O and Ce-O to describe the defects association with respect to ion packing model. They suggested that the marked contraction of Ce-O distance is an indication of vacancies being pushed away from the M^{3+} dopants, whereas a nominal contraction of the Ce-O bond indicates clustering of vacancies and dopants.

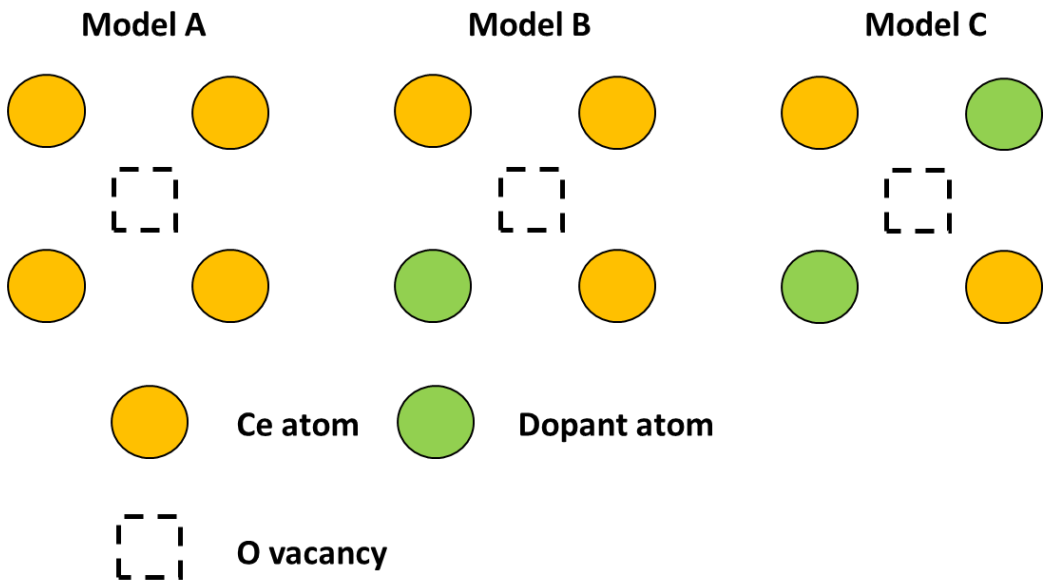

Figure 5. 11. Schematic of cation and vacancy association models described in [271]. The schematic is adapted from [250].

In accordance with literature mentioned above we found that the Ce-O distances shrink as well as the coordination number around Ce is reduced. According to Skorodumova et al. [48] the formation of oxygen vacancy is facilitated by the presence of two Ce^{3+} atoms and the most favorable position of these two Ce^{3+} atoms in the CeO_2 matrix is next to the oxygen vacancy. Zacherle et al. [50] showed that formation energy for the associate of doubly charged oxygen vacancy with two polarons i.e., [Ce^{3+}- V_O^{++}- Ce^{3+}] is lower than the neutral oxygen vacancy ($V_O^{\times}$). Moreover, by comparing the structural relaxation after oxygen vacancy formation it is found that the Ce^{3+} atoms stay closer to the vacancy than the Ce^{4+} atoms. [49,75] Besides, based on the calculations from Giannici et al., [250] at 5% M^{3+} doping, the configuration of dopants and vacancies are found to favor model A (80%) over model B (20%) shown in Figure 5.11. Therefore, we suggest that for LDC 5 the local structure around vacancy is an association between Ce^{3+} and V_O^{++} giving rise to the cluster [Ce^{3+}- V_O^{++}- Ce^{3+}], i.e., F^0 configuration. The Ce^{3+} in F^0 configuration is not favorable for CL emission in CeO_2, doping CeO_2 with La lead to

prevalence of trimers [Ce^{3+}- V_O^{++}- Ce^{3+}] instead of [Ce^{3+}- V_O^{++}- Ce^{4+}] from the vantage point of CL emission. This is the reason for CL emission quenching as a result of lanthanum doping.

The decline in F^0 population (Figure 5.10) among the LDC samples (LDC 10 through LDC 30) can be explained by the fact that at high doping level clustering of dopants and vacancies will be facilitated. Therefore, in that case oxygen vacancies stay close to La, the vacancy cluster [La^{3+}- V_O^{++}- La^{3+}] may become predominant. [248,273] Our EXAFS analysis showed that the association between oxygen vacancies and La^{3+} is negligible at 5% doping, with a progressive increase in clustering at 30% doping. Thus increasing concentration of La^{3+} causes defect clustering as well as Ce^{3+} to Ce^{4+} oxidation [266,267] and results in the decline of F^0 center population as shown in Figure 5.10.

5.4 Conclusion

The influence of local structure on the CL emission of pure and La-doped CeO_2 is demonstrated in this study. We validated that the CL emission results from various structural configurations around Ce^{3+} and oxygen vacancies, which can be described as F centers in CeO_2. The CL emission is favored by F^+ center configuration i.e., [Ce^{3+}- V_O^{++}- Ce^{4+}] cluster. The observed luminescence quenching in highly doped ceria was associated to the high oxygen vacancy concentration causing the dominance of F^0 centers ([Ce^{3+}- V_O^{++}- Ce^{3+}]) over F^+ centers. We found that the relative number of oxygen ions at a shorter distance in the first shell and Ce neighbors in the second shell around the Ce cation increases upon La doping. The decrease in the coordination number in the first shell around La atoms at high La doping indicates on the association between La^{3+} and oxygen vacancy. Local distortion of CeO_2 upon the La-doping and oxidation of Ce^{3+} species to Ce^{4+} explained the relative change in population of F centers. The non-radiative decay, as a result of oxygen vacancies demonstrated here, emphasizes the need to consider defect structure and interactions while designing optical materials for their efficiency and device performance.

6 Summary and Outlook

This work investigated the optical properties related to oxygen vacancies in the undoped reduced and doped ceria by means of the cathodoluminescence (CL) spectroscopy. In order to elucidate the mechanism that causes and controls the cathodoluminescence emission, a bridge between macroscopic optical properties and defect-induced local distortions is drawn. The pivotal role of short range associates involving oxygen vacancies and cations in the emission was demonstrated.

The local structure around the cations was determined using the Extended X-ray Absorption Fine Structure spectroscopy. A qualitative estimation of the defect concentration was carried out using impedance spectroscopy. By employing a Gaussian deconvolution procedure, the insights into cathodoluminescence spectra were attained.

Variation in a concentration of oxygen vacancies was achieved by sintering ceria under different oxygen partial pressure. The impedance spectroscopy confirmed a steady increase in the oxygen vacancy concentration with decreasing oxygen partial pressure. The Ce^{3+} ions in the reduced ceria lead to cathodoluminescence emission. As a function of oxygen vacancy concentration the CL emission intensity increases, reaches a maximum and then decreases. Adopting a F center description involving Ce^{3+}/Ce^{4+} and oxygen vacancies (V_O), the trend in cathodoluminescence emission was rationalized.

A Gaussian deconvolution procedure, applied to the emission spectra, showed that the CL emission was favored by F^+ center configuration of Ce^{3+} and oxygen vacancy associates. The dominance of F^0 center population is detrimental to CL emission. The high intensity CL emission for ceria sintered under high oxygen partial pressure is caused by the dominance of F^+ centers. The increased F^0 population leads to CL emission quenching for the samples sintered under low oxygen partial pressure. The different F centers formed in the reduced ceria as a result of association between polaron and oxygen vacancies. A relative population of F centers varies with respect to Ce^{3+} concentration in the lattice and the accompanying strain relaxation.

The F center luminescence in ceria is strongly influenced by local distortion and defect associates. To enlighten this fact, the La-doped ceria was investigated for local structure deformation and CL emission properties. The CL emission intensity quenched as a function of an

increasing La content in ceria. The CL spectral analysis confirmed that F^0 centers are responsible for the luminescence quenching, whereas F^+ centers favor the high intensity CL emission.

The local structure around both Ce and La cations was investigated by the K-Edge EXAFS. Despite preserving the fluorite structure on the whole, the La-doping in ceria leads to local structure distortions. The relative concentration of Ce^{3+}/Ce^{4+} is determined by a linear combination fitting of XANES spectra. These combined analyses corroborated the F center luminescence quenching in ceria. The potential of the CL spectroscopy to unravel local distortions arising from defects and association of these defects is illustrated.

The CL spectroscopy can be exploited for developing functional materials by virtue of defect engineering. The demonstrated ability of CL to recognize local structural distortion and formation of defect associates, which is often neglected in literature, could be correlated with other macroscopic properties such as a conductivity and strain.

7 Scientific Contributions

7.1 Original Scientific Papers

- Thanveer Thajudheen, Alex G. Dixon, Sandra Gardonio, Iztok Arčon, and Matjaž Valant, Oxygen Vacancy-Related Cathodoluminescence Quenching and Polarons in CeO_2, The Journal of Physical Chemistry C **2020** 124 (37), 19929-19936 DOI: 10.1021/acs.jpcc.0c04631
- Thanveer Thajudheen, Akansha Mehta, Uroš Luin, Sandra Gardonio, Iztok Arčon, and Matjaž Valant, Defect Induced Local Structure Distortion and Cathodoluminescence Quenching in Ceria. (to be submitted)

7.2 Conference Contributions:

- Thanveer Thajudheen, Alex G. Dixon, Sandra Gardonio, Iztok Arčon, and Matjaž Valant, Oxygen Vacancy-Related Cathodoluminescence Quenching and Polarons in CeO_2, 26^{th} Annual Meeting of the Slovenian Chemical Society, Portorož, 16-18 September 2020.
- Thanveer Thajudheen, Matjaž Valant, Cathodoluminescence Study of Defects in CeO_2, 3^{rd} Slovene Microscopy Symposium, Ankaran, 16-17 May 2019.

Bibliography

[1] R. Schmitt, A. Nenning, O. Kraynis, R. Korobko, A. I. Frenkel, I. Lubomirsky, S. M. Haile, and J. L. M. Rupp, Chem. Soc. Rev. **49**, 554 (2020).

[2] G. Kim, Ind. \& Eng. Chem. Prod. Res. Dev. **21**, 267 (1982).

[3] R. K. Usmen, R. W. McCabe, G. W. Graham, W. H. Weber, C. R. Peters, and H. S. Gandhi, in *Int. Fuels Lubr. Meet. Expo.* (SAE International, 1992).

[4] T. Montini, M. Melchionna, M. Monai, and P. Fornasiero, Chem. Rev. **116**, 5987 (2016).

[5] J. Ka\vspar, P. Fornasiero, G. Balducci, R. D. Monte, N. Hickey, and V. Sergo, Inorganica Chim. Acta **349**, 217 (2003).

[6] R. Di Monte, P. Fornasiero, J. Kašpar, M. Graziani, J. M. Gatica, S. Bernal, and A. Gómez-Herrero, Chem. Commun. 2167 (2000).

[7] R. Di Monte, P. Fornasiero, S. Desinan, J. Kašpar, J. M. Gatica, J. J. Calvino, and E. Fonda, Chem. Mater. **16**, 4273 (2004).

[8] M. Mogensen, J. Electrochem. Soc. **141**, 2122 (1994).

[9] O. A. Marina, C. Bagger, S. Primdahl, and M. Mogensen, Solid State Ionics **123**, 199 (1999).

[10] E. P. Murray, T. Tsai, and S. A. Barnett, Nature **400**, 649 (1999).

[11] Y.-H. Lee, H. Sumi, H. Muroyama, T. Matsui, and K. Eguchi, J. Electrochem. Soc. **160**, F579 (2013).

[12] L. Fan, C. Wang, M. Chen, and B. Zhu, J. Power Sources **234**, 154 (2013).

[13] H. Inaba and H. Tagawa, Solid State Ionics **83**, 1 (1996).

[14] B. Zhu, J. Power Sources **114**, 1 (2003).

[15] X. Wang, Y. Ma, S. Li, A.-H. Kashyout, B. Zhu, and M. Muhammed, J. Power Sources

196, 2754 (2011).

[16] A. S. V Ferreira, C. M. C. Soares, F. M. H. L. R. Figueiredo, and F. M. B. Marques, Int. J. Hydrogen Energy **36**, 3704 (2011).

[17] V. Jain, S. Bobade, D. Gulwade, and P. Gopalan, Ionics (Kiel). **16**, 487 (2010).

[18] X. Li, G. Xiao, and K. Huang, J. Electrochem. Soc. **158**, B225 (2011).

[19] M. Benamira, A. Ringuedé, V. Albin, R.-N. Vannier, L. Hildebrandt, C. Lagergren, and M. Cassir, J. Power Sources **196**, 5546 (2011).

[20] B. Zhu, X. Liu, and T. Schober, Electrochem. Commun. **6**, 378 (2004).

[21] R. Raza, G. Abbas, X. Wang, Y. Ma, and B. Zhu, Solid State Ionics **188**, 58 (2011).

[22] R. Raza, G. Abbas, S. K. Imran, I. Patel, and B. Zhu, J. Fuel Cell Sci. Technol. **8**, (2011).

[23] J. Hu, S. Tosto, Z. Guo, and Y. Wang, J. Power Sources **154**, 106 (2006).

[24] X. R. Liu, B. Zhu, J. R. Xu, J. C. Sun, and Z. Q. Mao, in *High-Performance Ceram. III* (Trans Tech Publications Ltd, 2004), pp. 425–430.

[25] P. Ji, J. Zhang, F. Chen, and M. Anpo, Appl. Catal. B Environ. **85**, 148 (2009).

[26] T. Feng, X. Wang, and G. Feng, Mater. Lett. **100**, 36 (2013).

[27] F. Chen, Y. Cao, and D. Jia, Appl. Surf. Sci. **257**, 9226 (2011).

[28] N. Sabari Arul, D. Mangalaraj, T. W. Kim, P. C. Chen, N. Ponpandian, P. Meena, and Y. Masuda, J. Mater. Sci. Mater. Electron. **24**, 1644 (2013).

[29] S. H. S. Chan, T. Yeong Wu, J. C. Juan, and C. Y. Teh, J. Chem. Technol. \& Biotechnol. **86**, 1130 (2011).

[30] G. R. Bamwenda, T. Uesigi, Y. Abe, K. Sayama, and H. Arakawa, Appl. Catal. A Gen. **205**, 117 (2001).

[31] A. Primo, T. Marino, A. Corma, R. Molinari, and H. García, J. Am. Chem. Soc. **133**, 6930 (2011).

[32] Y. Li, Q. Sun, M. Kong, W. Shi, J. Huang, J. Tang, and X. Zhao, J. Phys. Chem. C **115**,

14050 (2011).

[33] M. M. Khan, S. A. Ansari, D. Pradhan, D. H. Han, J. Lee, and M. H. Cho, Ind. Eng. Chem. Res. **53**, 9754 (2014).

[34] A. D. Liyanage, S. D. Perera, K. Tan, Y. Chabal, and K. J. Balkus, ACS Catal. **4**, 577 (2014).

[35] G. Li, D. Zhang, and J. C. Yu, Phys. Chem. Chem. Phys. **11**, 3775 (2009).

[36] M. Li, S. Zhang, L. Lv, M. Wang, W. Zhang, and B. Pan, Chem. Eng. J. **229**, 118 (2013).

[37] N. Aman, P. K. Satapathy, T. Mishra, M. Mahato, and N. N. Das, Mater. Res. Bull. **47**, 179 (2012).

[38] C. Xu and X. Qu, NPG Asia Mater. **6**, e90 (2014).

[39] J. Niu, A. Azfer, L. M. Rogers, X. Wang, and P. E. Kolattukudy, Cardiovasc. Res. **73**, 549 (2007).

[40] D. Schubert, R. Dargusch, J. Raitano, and S.-W. Chan, Biochem. Biophys. Res. Commun. **342**, 86 (2006).

[41] R. W. Tarnuzzer, J. Colon, S. Patil, and S. Seal, Nano Lett. **5**, 2573 (2005).

[42] J. Chen, S. Patil, S. Seal, and J. F. McGinnis, Nat. Nanotechnol. **1**, 142 (2006).

[43] W. A. Dollase, *Solid State Chemistry and Its Applications by A. R. West* (1985).

[44] H. Föll, (2019).

[45] L. E. B. D. J. J. García Solé, An Introd. to Opt. Spectrosc. Inorg. Solids 1 (2005).

[46] K. Momma and F. Izumi, J. Appl. Crystallogr. **41**, 653 (2008).

[47] B. Huang, R. Gillen, and J. Robertson, J. Phys. Chem. C **118**, 24248 (2014).

[48] N. V. Skorodumova, S. I. Simak, B. I. Lundqvist, I. A. Abrikosov, and B. Johansson, Phys. Rev. Lett. **89**, 166601/1 (2002).

[49] P. R. L. Keating, D. O. Scanlon, B. J. Morgan, N. M. Galea, and G. W. Watson, J. Phys. Chem. C **116**, 2443 (2012).

[50] T. Zacherle, A. Schriever, R. A. De Souza, and M. Martin, Phys. Rev. B - Condens. Matter Mater. Phys. **87**, 134104 (2013).

[51] V. Fernandes, R. J. O. Mossanek, P. Schio, J. J. Klein, A. J. A. de Oliveira, W. A. Ortiz, N. Mattoso, J. Varalda, W. H. Schreiner, M. Abbate, and D. H. Mosca, Phys. Rev. B **80**, 35202 (2009).

[52] M. Venkatesan, C. B. Fitzgerald, and J. M. D. Coey, Nature **430**, 630 (2004).

[53] S. Lany and A. Zunger, Phys. Rev. B **80**, 85202 (2009).

[54] B. J. Morgan and G. W. Watson, Phys. Rev. B **80**, 233102 (2009).

[55] M. Nolan and G. W. Watson, J. Chem. Phys. **125**, 144701 (2006).

[56] D. O. Scanlon, A. Walsh, B. J. Morgan, M. Nolan, J. Fearon, and G. W. Watson, J. Phys. Chem. C **111**, 7971 (2007).

[57] B. J. Morgan and G. W. Watson, J. Phys. Chem. C **114**, 2321 (2010).

[58] M. Nolan, J. E. Fearon, and G. W. Watson, Solid State Ionics **177**, 3069 (2006).

[59] C. W. M. Castleton, A. Lee, and J. Kullgren, J. Phys. Chem. C **123**, 5164 (2019).

[60] H. L. Tuller and A. S. Nowick, J. Electrochem. Soc. **126**, 209 (1979).

[61] T. G. STRATTON and H. L. TULLER, J. Chem. Soc. Trans. Ii **83**, 1143 (1987).

[62] H. L. Tuller and A. S. Nowick, J. Electrochem. Soc. **126**, 209 (1979).

[63] J. von. Rudolph, Z. Naturforsch. Tl. A **14**, 727 (1959).

[64] E. M. Greener J. M. Wimmer and W. M. Hirthe, Proc. Conf. Rare Earths, Fourth Conf. Phoenix, Arizona **14**, 538 (1964).

[65] R. N. Blumenthal, P. W. Lee, and R. J. Panlener, J. Electrochem. Soc. **118**, 123 (1971).

[66] B. C. H. Steele and J. M. Floyd, Proc. Br. Ceram. Soc. **19**, 55 (1971).

[67] S. Basu, P. S. Devi, and H. S. Maiti, J. Mater. Res. **19**, 3162 (2004).

[68] Y.-P. Fu, C.-W. Tseng, and P.-C. Peng, J. Eur. Ceram. Soc. **28**, 85 (2008).

[69] V. Esposito, M. Zunic, and E. Traversa, Solid State Ionics **180**, 1069 (2009).

[70] S. Kuharuangrong, J. Power Sources **171**, 506 (2007).

[71] B. Rambabu, S. Ghosh, and H. Jena, J. Mater. Sci. **41**, 7530 (2006).

[72] S. Sen, H. J. Avila-Paredes, and S. Kim, J. Mater. Chem. **18**, 3915 (2008).

[73] B. Zhu, X. Liu, Z. Zhu, and R. Ljungberg, Int. J. Hydrogen Energy **33**, 3385 (2008).

[74] S. Zha, C. Xia, and G. Meng, J. Power Sources **115**, 44 (2003).

[75] B. Huang, R. Gillen, and J. Robertson, J. Phys. Chem. C **118**, 24248 (2014).

[76] Y. Jiang, J. B. Adams, M. van Schilfgaarde, R. Sharma, and P. A. Crozier, Appl. Phys. Lett. **87**, 141917 (2005).

[77] T. Zacherle, A. Schriever, R. A. De Souza, and M. Martin, Phys. Rev. B - Condens. Matter Mater. Phys. **87**, 1 (2013).

[78] R. Korobko, A. Patlolla, A. Kossoy, E. Wachtel, H. L. Tuller, A. I. Frenkel, and I. Lubomirsky, Adv. Mater. **24**, 5857 (2012).

[79] R. Korobko, A. Lerner, Y. Li, E. Wachtel, A. I. Frenkel, and I. Lubomirsky, Appl. Phys. Lett. **106**, 42904 (2015).

[80] M. Hadad, H. Ashraf, G. Mohanty, C. Sandu, and P. Muralt, Acta Mater. **118**, 1 (2016).

[81] A. Kossoy, A. I. Frenkel, Y. Feldman, E. Wachtel, A. Milner, and I. Lubomirsky, Solid State Ionics **181**, 1473 (2010).

[82] R. Gerhardt, W.-K. Lee, and A. S. Nowick, J. Phys. Chem. Solids **48**, 563 (1987).

[83] T. Thamaraiselvi and S. Rajeswari, Trends Biomater. Artif. Organs **18**, 9 (2004).

[84] G. Pezzotti and K. Yamamoto, J. Mech. Behav. Biomed. **31**, 3 (2014).

[85] Y.-I. Kim, P. M. Woodward, K. Z. Baba-Kishi, and C. W. Tai, Chem. Mater. **16**, 1267 (2004).

[86] T. L. Nguyen, K. Kobayashi, T. Honda, Y. Iimura, K. Kato, A. Neghisi, K. Nozaki, F. Tappero, K. Sasaki, and H. Shirahama, Solid State Ionics **174**, 163 (2004).

[87] A. Fuertes, Dalton. Trans. **39**, 5942 (2010).

[88] K. Fukatsu, A. Leto, W. Zhu, N. Sugano, and G. Pezzotti, Acta Biomater. **8**, 1639 (2012).

[89] M. Boffelli, W. Zhu, M. Back, G. Sponchia, T. Francese, P. Riello, A. Benedetti, and G. Pezzotti, J. Phys. Chem. A **118**, 9828 (2014).

[90] B. G. Yacobi and D. B. Holt, *Cathodoluminescence Microscopy of Inorganic Solids*, 1st ed. (Springer US, 1990).

[91] V. A. T., Philips Tech. Rev. **38**, 41 (1978).

[92] B. G. Yacobi and D. B. Holt, J. Appl. Phys. **59**, R1 (1986).

[93] M. S., J. Phys. **44**, C4 (1983).

[94] T. H., Philos. Mag. B **49**, 371 (1984).

[95] D. B. Holt, Microsc. Semicond. Mater. 165 (1981).

[96] P. M. Petroff, C. Weisbuch, R. Dingle, A. C. Gossard, and W. Wiegmann, Appl. Phys. Lett. **38**, 965 (1981).

[97] D. G. J., J. Phys. D **17**, L133 (1984).

[98] S. Myhajlenko, Electron Microsc. Anal. 111 (1984).

[99] G. Pezzotti, M. C. Munisso, A. A. Porporati, and K. Lessnau, Biomaterials **31**, 6901 (2010).

[100] J. Zhang, S. Walsh, C. Brooks, D. G. Schlom, and L. J. Brillson, J. Vac. Sci. \& Technol. B Microelectron. Nanom. Struct. Process. Meas. Phenom. **26**, 1466 (2008).

[101] A. Leto, A. A. Porporati, W. Zhu, M. Green, and G. Pezzotti, J. Appl. Phys. **101**, 93514 (2007).

[102] G. Pezzotti and A. Leto, Phys. Rev. Lett. **103**, 175501 (2009).

[103] M. Hastenrath and E. Kubalek, Scan. Electron Microsc. 157 (1982).

[104] S. A., J. Microsc. **118**, 297 (1980).

[105] K. Thonke, I. Tischer, M. Hocker, M. Schirra, K. Fujan, M. Wiedenmann, R. Schneider, M. Frey, and M. Feneberg, {IOP} Conf. Ser. Mater. Sci. Eng. **55**, 12018 (2014).

[106] P. R. Edwards and R. W. Martin, Semicond. Sci. Technol. **26**, 64005 (2011).

[107] A. Leto and G. Pezzotti, Phys. Status Solidi **208**, 1119 (2011).

[108] B. J. M. Brenny, T. Coenen, and A. Polman, J. Appl. Phys. **115**, 244307 (2014).

[109] M. A. Gubko, W. Husinsky, and A. A. Ionin, Laser Phys. Lett **11**, 65301 (2014).

[110] V. Myroshnychenko, J. Nelayah, G. Adamo, N. Geuquet, J. Rodr\'\iguez-Fernández, I. Pastoriza-Santos, K. F. MacDonald, L. Henrard, L. M. Liz-Marzán, N. I. Zheludev, and others, Nano Lett. **12**, 4172 (2012).

[111] M. W. Knight, L. Liu, Y. Wang, L. Brown, S. Mukherjee, N. S. King, H. O. Everitt, P. Nordlander, and N. J. Halas, Nano Lett. **12**, 6000 (2012).

[112] X. L. Zhu, Y. Ma, J. S. Zhang, J. Xu, X. F. Wu, Y. Zhang, X. B. Han, Q. Fu, Z. M. Liao, L. Chen, and others, Phys. Rev. Lett. **105**, 127402 (2010).

[113] M. Kuttge, F. J. G. de Abajo, and A. Polman, Opt. Express **17**, 10385 (2009).

[114] R. Sapienza, T. Coenen, J. Renger, M. Kuttge, N. F. Van Hulst, and A. Polman, Nat. Mater. **11**, 781 (2012).

[115] T. Suzuki and N. Yamamoto, Opt. Express **17**, 23664 (2009).

[116] K. Takeuchi and N. Yamamoto, Opt. Express **19**, 12365 (2011).

[117] P. Kok, W. J. Munro, K. Nemoto, T. C. Ralph, J. P. Dowling, and G. J. Milburn, Rev. Mod. Phys. **79**, 135 (2007).

[118] A. Gruber, A. Dräbenstedt, C. Tietz, L. Fleury, J. Wrachtrup, and C. von Borczyskowski, Science (80-.). **276**, 2012 (1997).

[119] N. Mizuochi, T. Makino, H. Kato, D. Takeuchi, M. Ogura, H. Okushi, M. Nothaft, P. Neumann, A. Gali, F. Jelezko, J. Wrachtrup, and S. Yamasaki, Nat. Photonics **6**, 299 (2012).

[120] J. McKeever, A. Boca, A. D. Boozer, R. Miller, J. R. Buck, A. Kuzmich, and H. J. Kimble, Science (80-.). **303**, 1992 (2004).

[121] L. H. G. Tizei and M. Kociak, Phys. Rev. Lett. **110**, 1 (2013).

[122] R. HANBURY BROWN and R. Q. TWISS, Nature **178**, 1046 (1956).

[123] R. Bourrellier, S. Meuret, A. Tararan, O. Stéphan, M. Kociak, L. H. G. Tizei, and A. Zobelli, Nano Lett. **16**, 4317 (2016).

[124] S. Meuret, L. H. G. Tizei, T. Auzelle, R. Songmuang, B. Daudin, B. Gayral, and M. Kociak, ACS Photonics **3**, 1157 (2016).

[125] S. Meuret, T. Coenen, H. Zeijlemaker, M. Latzel, S. Christiansen, S. Conesa-Boj, and A. Polman, Phys. Rev. B **96**, 35308 (2017).

[126] T. Coenen and N. M. Haegel, Appl. Phys. Rev. **4**, 31103 (2017).

[127] X. Ma, M. Grüßer, and R. Schuster, J. Phys. Chem. C **118**, 23247 (2014).

[128] T. Coenen, E. J. R. Vesseur, and A. Polman, ACS Nano **6**, 1742 (2012).

[129] N. Yamamoto, S. Ohtani, and F. J. de Abajo, Nano Lett. **11**, 91 (2011).

[130] H. Acar, T. Coenen, A. Polman, and L. K. Kuipers, ACS Nano **6**, 8226 (2012).

[131] T. Coenen and A. Polman, ACS Nano **8**, 7350 (2014).

[132] T. Coenen, J. Van De Groep, and A. Polman, ACS Nano **7**, 1689 (2013).

[133] T. Coenen, E. J. R. Vesseur, and A. Polman, Appl. Phys. Lett. **99**, 143103 (2011).

[134] D. T. Schoen, T. Coenen, F. J. de Abajo, M. L. Brongersma, and A. Polman, Nano Lett. **13**, 188 (2013).

[135] K. Ura, H. Fujioka, and T. Hosokawa, Microscopy **27**, 247 (1978).

[136] D. Winkler, R. Schmitt, M. Brunner, and B. Lischke, IBM J. Res. Dev. **34**, 189 (1990).

[137] R. J. Moerland, I. G. C. Weppelman, M. W. H. Garming, P. Kruit, and J. P. Hoogenboom, Opt. Express **24**, 24760 (2016).

[138] A. Lassise, P. H. A. Mutsaers, and O. J. Luiten, Rev. Sci. Instrum. **83**, 43705 (2012).

[139] M. Merano, S. Sonderegger, A. Crottini, S. Collin, P. Renucci, E. Pelucchi, A. Malko, M. H. Baier, E. Kapon, B. Deveaud, and others, Nature **438**, 479 (2005).

[140] X. Fu, G. Jacopin, M. Shahmohammadi, R. Liu, M. Benameur, J.-D. Ganiere, J. Feng, W. Guo, Z.-M. Liao, B. Deveaud, and others, ACS Nano **8**, 3412 (2014).

[141] M. Merano, S. Sonderegger, A. Crottini, S. Collin, E. Pelucchi, P. Renucci, A. Malko, M. H. Baier, E. Kapon, J. D. Ganiere, and others, Appl. Phys. B **84**, 343 (2006).

[142] Y.-P. Xiong, H. Kishimoto, K. Yamaji, M. Yoshinaga, T. Horita, M. E. Brito, and H. Yokokawa, Electrochem. Solid-State Lett. **13**, B21 (2010).

[143] R. N. Blumenthal and R. L. Hofmaier, J. Electrochem. Soc. **121**, 126 (1974).

[144] R. J. Panlener, R. N. Blumenthal, and J. E. Garnier, J. Phys. Chem. Solids **36**, 1213 (1975).

[145] O. T. Sørensen, J. Solid State Chem. **18**, 217 (1976).

[146] J. W. Dawicke and R. N. Blumenthal, J. Electrochem. Soc. **133**, 904 (1986).

[147] J. E. Garnier, R. N. Blumenthal, R. J. Panlener, and R. K. Sharma, J. Phys. Chem. Solids **37**, 368 (1976).

[148] J.-H. Park, R. N. Blumenthal, and M. A. Panhans, J. Electrochem. Soc. **135**, 855 (1988).

[149] B. Zachau-Christiansen, T. Jacobsen, and S. Skaarup, Solid State Ionics **86**–**88**, 725 (1996).

[150] S. Wang, H. Inaba, H. Tagawa, and T. Hashimoto, J. Electrochem. Soc. **144**, 4076 (1997).

[151] S. Wang, H. Inaba, H. Tagawa, M. Dokiya, and T. Hashimoto, Solid State Ionics **107**, 73 (1998).

[152] M. Mogensen, N. M. Sammes, and G. A. Tompsett, Solid State Ionics **129**, 63 (2000).

[153] S. Wang, H. Inaba, H. Tagawa, and T. Hashimoto, J. Electrochem. Soc. **144**, 4076 (1997).

[154] G. Brauer and H. Gradinger, Naturwissenschaften **38**, 559 (1951).

[155] D. J. M. Bevan, J. Inorg. Nucl. Chem. **1**, 49 (1955).

[156] G. Brauer and K. A. Gingerich, J. Inorg. Nucl. Chem. **16**, 87 (1960).

[157] S. P. Ray, A. S. Nowick, and D. E. Cox, J. Solid State Chem. **15**, 344 (1975).

[158] M. Ricken, J. Nölting, and I. Riess, J. Solid State Chem. **54**, 89 (1984).

[159] R. Körner, M. Ricken, J. Nölting, and I. Riess, J. Solid State Chem. **78**, 136 (1989).

[160] D.-J. Kim, J. Am. Ceram. Soc. **72**, 1415 (1989).

[161] L. Eyring, *Synthesis of Lanthanide and Actinide Compound* (1991).

[162] E. Curti, (1997).

[163] M. Lok, in *Synth. Solid Catal.* (John Wiley & Sons, Ltd, 2009), pp. 135–151.

[164] J. W. Mullin, in *Cryst. (Fourth Ed.*, edited by J. W. Mullin, Fourth Edi (Butterworth-Heinemann, Oxford, 2001).

[165] C. J. J. den Ouden and R. W. Thompson, J. Colloid Interface Sci. **143**, 77 (1991).

[166] M. Lok, in *Synth. Solid Catal.* (John Wiley & Sons, Ltd, 2009), pp. 135–151.

[167] P. E. C. E. F. & J. I. G. D. E. Newbury D. C. Joy, (n.d.).

[168] T. E. Everhart and P. H. Hoff, J. Appl. Phys. **42**, 5837 (1971).

[169] J. B. Steyn, P. Giles†, and D. B. Holt, J. Microsc. **107**, 107 (1976).

[170] S. Datta, B. G. Yacobi, and D. B. Holt, J. Mater. Sci. **12**, 2411 (1977).

[171] S. Datta, B. G. Yacobi, and D. B. Holt, J. Lumin. **21**, 53 (1979).

[172] K. Lohnert and E. Kubalek, Microsc. Semicond. Mater. 303 (1983).

[173] K. Lohnert and E. Kubalek, Phys. Status Solidi **83**, 307 (1984).

[174] M. Cocito, C. Papuzza, and F. Taiariol, Microsc. Semicond. Mater. 273 (1983).

[175] A. K. Chin, H. Temkin, and R. J. Roedel, Appl. Phys. Lett. **34**, 476 (1979).

[176] S. J. Pennycook, A. J. Craven, and L. M. Brown, Dev. Electron Microsc. Anal. 69 (1977).

[177] P. M. Petroff and D. V Lang, Appl. Phys. Lett. **31**, 60 (1977).

[178] S. Myhajlenko and W. K. Ke, J. Phys. E. **17**, 200 (1984).

[179] R. Schmitt, A. Nenning, O. Kraynis, R. Korobko, A. I. Frenkel, I. Lubomirsky, S. M. Haile, and J. L. M. Rupp, Chem. Soc. Rev. **49**, 554 (2020).

[180] P. P. Paufler, J. Synchrotron Radiat. **18**, 818 (2011).

[181] R. Jenkins, R. Manne, R. Robin, and C. Senemaud, X-Ray Spectrom. **20**, 149 (1991).

[182] A. Kossoy, Q. Wang, R. Korobko, V. Grover, Y. Feldman, E. Wachtel, A. K. Tyagi, A. I. Frenkel, and I. Lubomirsky, Phys. Rev. B **87**, 54101 (2013).

[183] I. Arcon, (2008).

[184] S. I. Zabinsky, J. J. Rehr, A. Ankudinov, R. C. Albers, and M. J. Eller, Phys. Rev. B **52**, 2995 (1995).

[185] P. J. Durham, J. B. Pendry, and C. H. Hodges, Comput. Phys. Commun. **25**, 193 (1982).

[186] D. E. Sayers, E. A. Stern, and F. W. Lytle, Phys. Rev. Lett. **27**, 1204 (1971).

[187] J. J. Rehr and R. C. Albers, Rev. Mod. Phys. **72**, 621 (2000).

[188] C. F. J. König, J. A. van Bokhoven, T. J. Schildhauer, and M. Nachtegaal, J. Phys. Chem. C **116**, 19857 (2012).

[189] E. D. Crozier, Nucl. Instruments Methods Phys. Res. Sect. B Beam Interact. with Mater. Atoms **133**, 134 (1997).

[190] B. Ravel and M. Newville, J. Synchrotron Radiat. **12**, 537 (2005).

[191] E. von Hauff, J. Phys. Chem. C **123**, 11329 (2019).

[192] Beau Lambert, (2012).

[193] N. V Skorodumova, R. Ahuja, S. I. Simak, I. A. Abrikosov, B. Johansson, and B. I. Lundqvist, Phys. Rev. B **64**, 115108 (2001).

[194] T. Nakazawa, T. Inoue, M. Satoh, and Y. Yamamoto, Jpn. J. Appl. Phys. **34**, 548 (1995).

[195] V. V. Pushkarev, V. I. Kovalchuk, and J. L. d'Itri, J. Phys. Chem. B **108**, 5341 (2004).

[196] Z. Wu, M. Li, J. Howe, H. M. Meyer, and S. H. Overbury, Langmuir **26**, 16595 (2010).

[197] J. E. Spanier, R. D. Robinson, F. Zhang, S.-W. Chan, and I. P. Herman, Phys. Rev. B **64**, 245407 (2001).

[198] J. Xu, J. Harmer, G. Li, T. Chapman, P. Collier, S. Longworth, and S. C. Tsang, Chem. Commun. **46**, 1887 (2010).

[199] H. Nörenberg and G. A. D. Briggs, Phys. Rev. Lett. **79**, 4222 (1997).

[200] Y. Lin, Z. Wu, J. Wen, K. R. Poeppelmeier, and L. D. Marks, Nano Lett. **14**, 191 (2014).

[201] L. J. Brillson, W. T. Ruane, H. Gao, Y. Zhang, J. Luo, H. von Wenckstern, and M. Grundmann, Mater. Sci. Semicond. Process. **57**, 197 (2017).

[202] G. Pezzotti and A. Leto, Phys. Rev. Lett. **103**, 175501 (2009).

[203] G. Pezzotti, M. C. Munisso, A. A. Porporati, and K. Lessnau, Biomaterials **31**, 6901 (2010).

[204] D. Y. Wang, D. S. Park, J. Griffith, and A. S. Nowick, Solid State Ionics **2**, 95 (1981).

[205] J. Faber, C. Geoffroy, A. Roux, A. Sylvestre, and P. Abélard, Appl. Phys. A **49**, 225 (1989).

[206] J. A. Kilner, Solid State Ionics **129**, 13 (2000).

[207] P. Zhang, Y. Ma, C. Xie, Z. Guo, X. He, E. Valsami-Jones, I. Lynch, W. Luo, L. Zheng, and Z. Zhang, Environ. Sci. Nano **6**, 60 (2019).

[208] I. Kozjek Škofic, J. Padežnik Gomilšek, B. Pihlar, A. Kodre, and N. Bukovec, Sol. Energy Mater. Sol. Cells **95**, 779 (2011).

[209] S. Wada, K. Oka, K. Watanabe, and Y. Izumi, Front. Chem. **1**, 8 (2013).

[210] M. Balestrieri, S. Colis, M. Gallart, G. Schmerber, M. Ziegler, P. Gilliot, and A. Dinia, J. Mater. Chem. C **3**, 7014 (2015).

[211] J. M. Costantini, P. Seo, K. Yasuda, A. S. I. Bhuian, T. Ogawa, and D. Gourier, J. Lumin.

226, 117379 (2020).

[212] S. Aškrabić, Z. D. Dohčević-Mitrović, V. D. Araújo, G. Ionita, M. M. de Lima, and A. Cantarero, J. Phys. D. Appl. Phys. **46**, 495306 (2013).

[213] S. Tiwari, G. Rathore, N. Patra, A. K. Yadav, D. Bhattacharya, S. N. Jha, C. M. Tseng, S. W. Liu, S. Biring, and S. Sen, J. Alloys Compd. **782**, 689 (2019).

[214] K. Smits, L. Grigorjeva, W. Łojkowski, and J. D. Fidelus, Phys. Status Solidi C **4**, 770 (2007).

[215] K. Smits, L. Grigorjeva, D. Millers, A. Sarakovskis, J. Grabis, and W. Lojkowski, J. Lumin. **131**, 2058 (2011).

[216] N. Borhan, K. Gheisari, and M. Z. Shoushtari, J. Supercond. Nov. Magn. **29**, 145 (2016).

[217] P. S. Das and G. P. Singh, J. Magn. Magn. Mater. **401**, 918 (2016).

[218] M. Youssef, K. J. Van Vliet, and B. Yildiz, Phys. Rev. Lett. **119**, 126002 (2017).

[219] G. Adachi and N. Imanaka, Chem. Rev. **98**, 1479 (1998).

[220] W. C. Chueh and S. M. Haile, Philos. Trans. R. Soc. A Math. Phys. Eng. Sci. **368**, 3269 (2010).

[221] M. A. Henderson, C. L. Perkins, M. H. Engelhard, S. Thevuthasan, and C. H. F. Peden, Surf. Sci. **526**, 1 (2003).

[222] X. Han, J. Lee, and H.-I. Yoo, Phys. Rev. B **79**, 100403 (2009).

[223] M. Figaj and K. D. Becker, Solid State Ionics **141**–**142**, 507 (2001).

[224] H. L. Tuller and A. S. Nowick, J. Phys. Chem. Solids **38**, 859 (1977).

[225] M. Nakayama, H. Ohshima, M. Nogami, and M. Martin, Phys. Chem. Chem. Phys. **14**, 6079 (2012).

[226] A. E. Hughes, J. D. Gorman, P. J. K. Patterson, and R. Carter, Surf. Interface Anal. **24**, 634 (1996).

[227] S. R. Bishop, K. L. Duncan, and E. D. Wachsman, Acta Mater. **57**, 3596 (2009).

[228] R. D. Shannon, Acta Crystallogr. Sect. A **32**, 751 (1976).

[229] J. Kašpar, P. Fornasiero, and M. Graziani, Catal. Today **50**, 285 (1999).

[230] W. C. Chueh, C. Falter, M. Abbott, D. Scipio, P. Furler, S. M. Haile, and A. Steinfeld, Science (80-.). **330**, 1797 (2010).

[231] W. C. Chueh, Y. Hao, W. Jung, and S. M. Haile, Nat. Mater. **11**, 155 (2012).

[232] W. Jung, J. O. Dereux, W. C. Chueh, Y. Hao, and S. M. Haile, Energy Environ. Sci. **5**, 8682 (2012).

[233] R. Schmitt, J. Spring, R. Korobko, and J. L. M. Rupp, ACS Nano **11**, 8881 (2017).

[234] S. Schweiger, R. Pfenninger, W. J. Bowman, U. Aschauer, and J. L. M. Rupp, Adv. Mater. **29**, 1605049 (2017).

[235] W. Lin, Y. Huang, X.-D. Zhou, and Y. Ma, Int. J. Toxicol. **25**, 451 (2006).

[236] J. Koettgen, S. Grieshammer, P. Hein, B. O. H. Grope, M. Nakayama, and M. Martin, Phys. Chem. Chem. Phys. **20**, 14291 (2018).

[237] M. Coduri, S. Checchia, M. Longhi, D. Ceresoli, and M. Scavini, Front. Chem. **6**, 526 (2018).

[238] C. Artini, Inorg. Chem. **57**, 13047 (2018).

[239] M. Tang, J. A. Valdez, K. E. Sickafus, and P. Lu, Appl. Phys. Lett. **90**, 151907 (2007).

[240] J. A. Kilner, Chem. Lett. **37**, 1012 (2008).

[241] I. Riess, R. Koerner, M. Ricken, and J. Noelting, Solid State Ionics **28**–**30**, 539 (1988).

[242] N. Stelzer, J. Nölting, and I. Riess, J. Solid State Chem. **117**, 392 (1995).

[243] E. A. Kümmerle and G. Heger, J. Solid State Chem. **147**, 485 (1999).

[244] T. Ohashi, S. Yamazaki, T. Tokunaga, Y. Arita, T. Matsui, T. Harami, and K. Kobayashi, Solid State Ionics **113**–**115**, 559 (1998).

[245] S. Yamazaki, T. Matsui, T. Ohashi, and Y. Arita, Solid State Ionics **136**–**137**, 913 (2000).

[246] S. Yamazaki, T. Matsui, T. Sato, Y. Arita, and T. Nagasaki, Solid State Ionics **154**–**155**, 113 (2002).

[247] H. Nitani, T. Nakagawa, M. Yamanouchi, T. Osuki, M. Yuya, and T. A. Yamamoto, Mater. Lett. **58**, 2076 (2004).

[248] H. Deguchi, H. Yoshida, T. Inagaki, and M. Horiuchi, Solid State Ionics **176**, 1817 (2005).

[249] Y. Wang, H. Kageyama, T. Mori, H. Yoshikawa, and J. Drennan, Solid State Ionics **177**, 1681 (2006).

[250] F. Giannici, G. Gregori, C. Aliotta, A. Longo, J. Maier, and A. Martorana, Chem. Mater. **26**, 5994 (2014).

[251] A. Kossoy, A. I. Frenkel, Q. Wang, E. Wachtel, and I. Lubomirsky, Adv. Mater. **22**, 1659 (2010).

[252] T. Thajudheen, A. G. Dixon, S. Gardonio, I. Arčon, and M. Valant, J. Phys. Chem. C **124**, 19929 (2020).

[253] J. A. Solera, J. García, and M. G. Proietti, Phys. Rev. B **51**, 2678 (1995).

[254] A. V Soldatov, T. S. Ivanchenko, S. Della Longa, A. Kotani, Y. Iwamoto, and A. Bianconi, Phys. Rev. B **50**, 5074 (1994).

[255] J.-F. Lee, M.-T. Tang, W. C. Shih, and R. S. Liu, Mater. Res. Bull. **37**, 555 (2002).

[256] K. Singh, R. Kumar, and A. Chowdhury, J. Mater. Sci. **51**, 4134 (2016).

[257] B. Reddy M., L. Katta, and G. Thrimurthulu, Chem. Mater. **22**, 467 (2010).

[258] M. Balaguer, C. Solís, and J. M. Serra, J. Phys. Chem. C **116**, 7975 (2012).

[259] M. Newville, T. Stensitzki, D. B. Allen, and A. Ingargiola, (2014).

[260] D. Horlait, L. Claparède, N. Clavier, S. Szenknect, N. Dacheux, J. Ravaux, and R. Podor, Inorg. Chem. **50**, 7150 (2011).

[261] A. Kossoy, Q. Wang, R. Korobko, V. Grover, Y. Feldman, E. Wachtel, A. K. Tyagi, A. I.

Frenkel, and I. Lubomirsky, Phys. Rev. B **87**, 54101 (2013).

[262] J. J. Rehr, R. C. Albers, and S. I. Zabinsky, Phys. Rev. Lett. **69**, 3397 (1992).

[263] P. O. Maksimchuk, V. V Seminko, I. I. Bespalova, and A. A. Masalov, Funct. Mater. **21**, 3 (2014).

[264] I. Yeriskin and M. Nolan, J. Phys. Condens. Matter **22**, 135004 (2010).

[265] N. Yang, P. Orgiani, E. Di Bartolomeo, V. Foglietti, P. Torelli, A. V Ievlev, G. Rossi, S. Licoccia, G. Balestrino, S. V Kalinin, and C. Aruta, J. Phys. Chem. C **121**, 8841 (2017).

[266] L. S. R. Rocha, F. Schipani, C. M. Aldao, L. Cabral, A. Z. Simoes, C. Macchi, G. E. Marques, M. A. Ponce, and E. Longo, J. Phys. Chem. C **124**, 997 (2020).

[267] D. Loche, L. M. Morgan, A. Casu, G. Mountjoy, C. O'Regan, A. Corrias, and A. Falqui, RSC Adv. **9**, 6745 (2019).

[268] M. Coduri, S. Checchia, M. Longhi, D. Ceresoli, and M. Scavini, Front. Chem. **6**, 526 (2018).

[269] H. Inaba, R. Sagawa, H. Hayashi, and K. Kawamura, Solid State Ionics **122**, 95 (1999).

[270] J. Koettgen and M. Martin, J. Phys. Chem. C **123**, 6333 (2019).

[271] M. Yashima, N. Ishizawa, and M. Yoshimura, J. Am. Ceram. Soc. **75**, 1541 (1992).

[272] J. Dexpert-Ghys, M. Faucher, and P. Caro, J. Solid State Chem. **54**, 179 (1984).

[273] H. Yoshida, H. Deguchi, K. Miura, M. Horiuchi, and T. Inagaki, Solid State Ionics **140**, 191 (2001).

Permissions to Reproduce Figures

Permission for figures 1.8, 1.9, 1.10, and 1.11

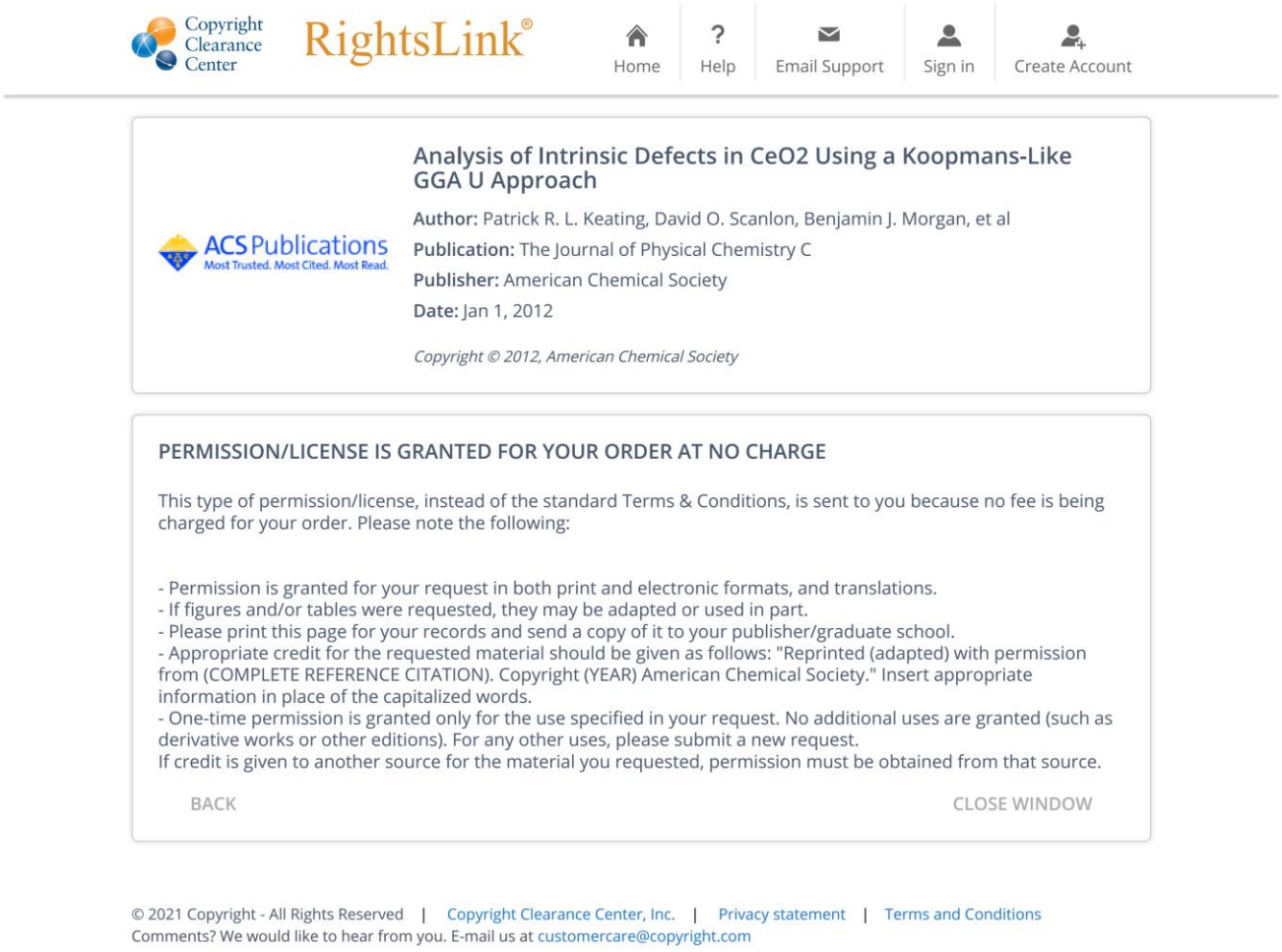

Permission for Figures 1.12 and 1.13

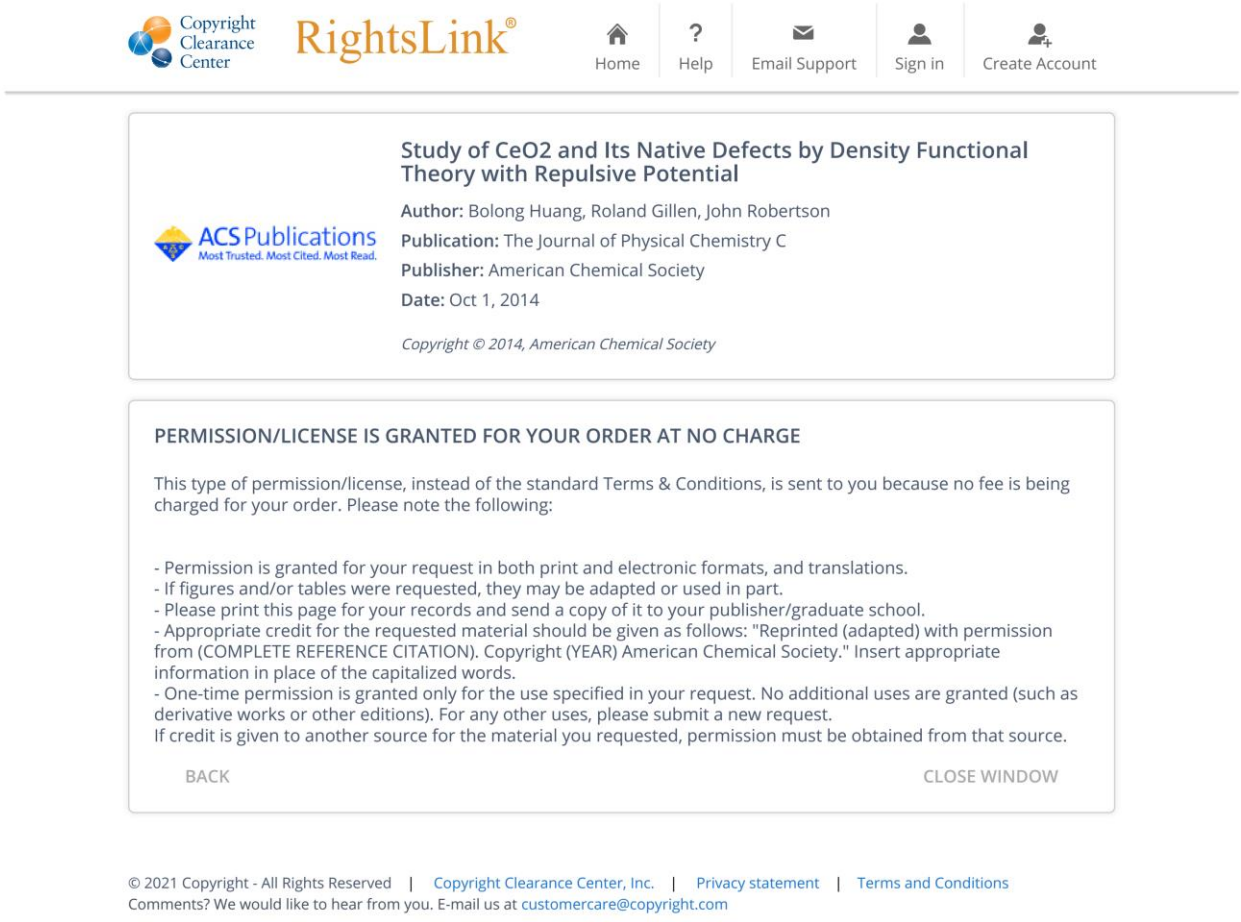

Copyright Clearance Center RightsLink®

Home | Help | Email Support | Sign in | Create Account

ACS Publications
Most Trusted. Most Cited. Most Read.

Study of CeO2 and Its Native Defects by Density Functional Theory with Repulsive Potential

Author: Bolong Huang, Roland Gillen, John Robertson
Publication: The Journal of Physical Chemistry C
Publisher: American Chemical Society
Date: Oct 1, 2014

Copyright © 2014, American Chemical Society

PERMISSION/LICENSE IS GRANTED FOR YOUR ORDER AT NO CHARGE

This type of permission/license, instead of the standard Terms & Conditions, is sent to you because no fee is being charged for your order. Please note the following:

- Permission is granted for your request in both print and electronic formats, and translations.
- If figures and/or tables were requested, they may be adapted or used in part.
- Please print this page for your records and send a copy of it to your publisher/graduate school.
- Appropriate credit for the requested material should be given as follows: "Reprinted (adapted) with permission from (COMPLETE REFERENCE CITATION). Copyright (YEAR) American Chemical Society." Insert appropriate information in place of the capitalized words.
- One-time permission is granted only for the use specified in your request. No additional uses are granted (such as derivative works or other editions). For any other uses, please submit a new request.

If credit is given to another source for the material you requested, permission must be obtained from that source.

BACK CLOSE WINDOW

Permission for Figure 2.1

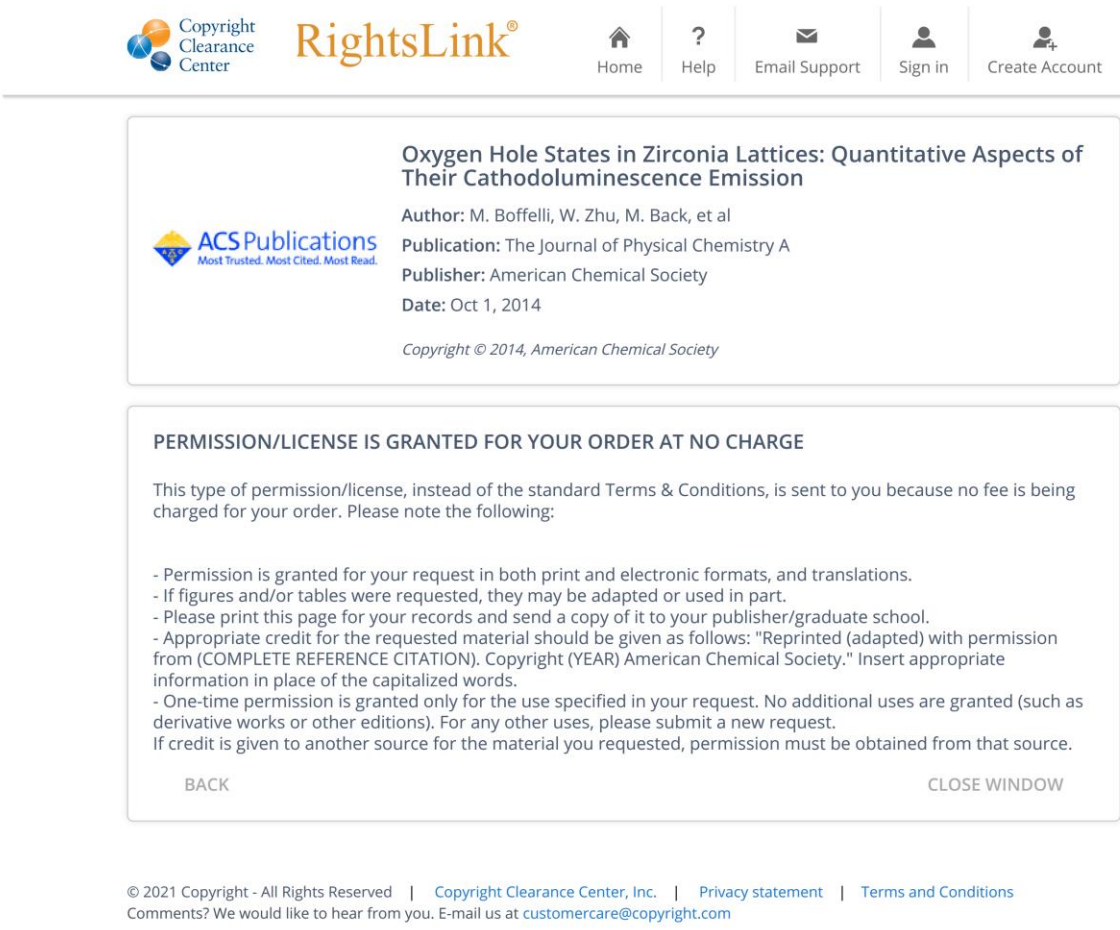

Permission for Figure 2.2

Copyright Clearance Center RightsLink®

Home | Help | Email Support | Thanveer Thajudheen

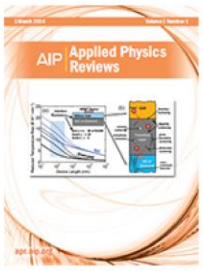

Cathodoluminescence for the 21st century: Learning more from light

Author: T. Coenen, N. M. Haegel
Publication: Applied Physics Reviews
Publisher: AIP Publishing
Date: Sep 1, 2017

Rights managed by AIP Publishing.

Order Completed

Thank you for your order.

This Agreement between Mr. Thanveer Thajudheen ("You") and AIP Publishing ("AIP Publishing") consists of your license details and the terms and conditions provided by AIP Publishing and Copyright Clearance Center.

Your confirmation email will contain your order number for future reference.

License Number	5036530229615
License date	Mar 26, 2021

Printable Details

Licensed Content

Licensed Content Publisher	AIP Publishing
Licensed Content Publication	Applied Physics Reviews
Licensed Content Title	Cathodoluminescence for the 21st century: Learning more from light
Licensed Content Author	T. Coenen, N. M. Haegel
Licensed Content Date	Sep 1, 2017
Licensed Content Volume	4
Licensed Content Issue	3

Order Details

Type of Use	Thesis/Dissertation
Requestor type	Student
Format	Print and electronic
Portion	Figure/Table
Number of figures/tables	1

About Your Work

Title	Spectroscopic investigation of Oxygen vacancies in CeO2
Institution name	Univerza v Novi Gorici
Expected presentation date	Sep 2021

Additional Data

Portions	Figure 4

Requestor Location

Requestor Location	Mr. Thanveer Thajudheen Univerza v Novi Gorici Vipavska 11c SI-5270 Ajdovščina Ajdovščina, Nova Gorica 5270 Slovenia Attn: Mr. Thanveer Thajudheen

Price

Total	0.00 EUR

Tax Details

Total: 0.00 EUR

CLOSE WINDOW ORDER MORE

Permission for Figures 3.1, 3.2 and 3.3

Copyright Clearance Center RightsLink®

Home | Help | Email Support | Thanveer Thajudheen

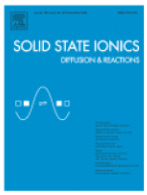

Physical, chemical and electrochemical properties of pure and doped ceria

Author: Mogens Mogensen,Nigel M. Sammes,Geoff A. Tompsett
Publication: Solid State Ionics
Publisher: Elsevier
Date: April 2000

Order Completed

Thank you for your order.

This Agreement between Mr. Thanveer Thajudheen ("You") and Elsevier ("Elsevier") consists of your license details and the terms and conditions provided by Elsevier and Copyright Clearance Center.

Your confirmation email will contain your order number for future reference.

License Number	5046441388841
License date	Apr 12, 2021

Printable Details

Licensed Content

Licensed Content Publisher	Elsevier
Licensed Content Publication	Solid State Ionics
Licensed Content Title	Physical, chemical and electrochemical properties of pure and doped ceria
Licensed Content Author	Mogens Mogensen,Nigel M. Sammes,Geoff A. Tompsett
Licensed Content Date	Apr 1, 2000
Licensed Content Volume	129
Licensed Content Issue	1-4
Licensed Content Pages	32
Journal Type	S&T

Order Details

Type of Use	reuse in a thesis/dissertation
Portion	figures/tables/illustrations
Number of figures/tables/illustrations	5
Format	both print and electronic
Are you the author of this Elsevier article?	No
Will you be translating?	No

About Your Work

Title	Spectroscopic investigation of Oxygen vacancies in CeO2
Institution name	Univerza v Novi Gorici
Expected presentation date	Sep 2021

Additional Data

Portions	Figures 2,3,4,8,12

Requestor Location

Requestor Location	Mr. Thanveer Thajudheen Univerza v Novi Gorici Vipavska 11c SI-5270 Ajdovščina Ajdovščina, Nova Gorica 5270 Slovenia Attn: Mr. Thanveer Thajudheen

Price

Total	0.00 EUR

Tax Details

Publisher Tax ID	GB 494 6272 12

Total: 0.00 EUR

CLOSE WINDOW ORDER MORE

Permission for Figure 3.4

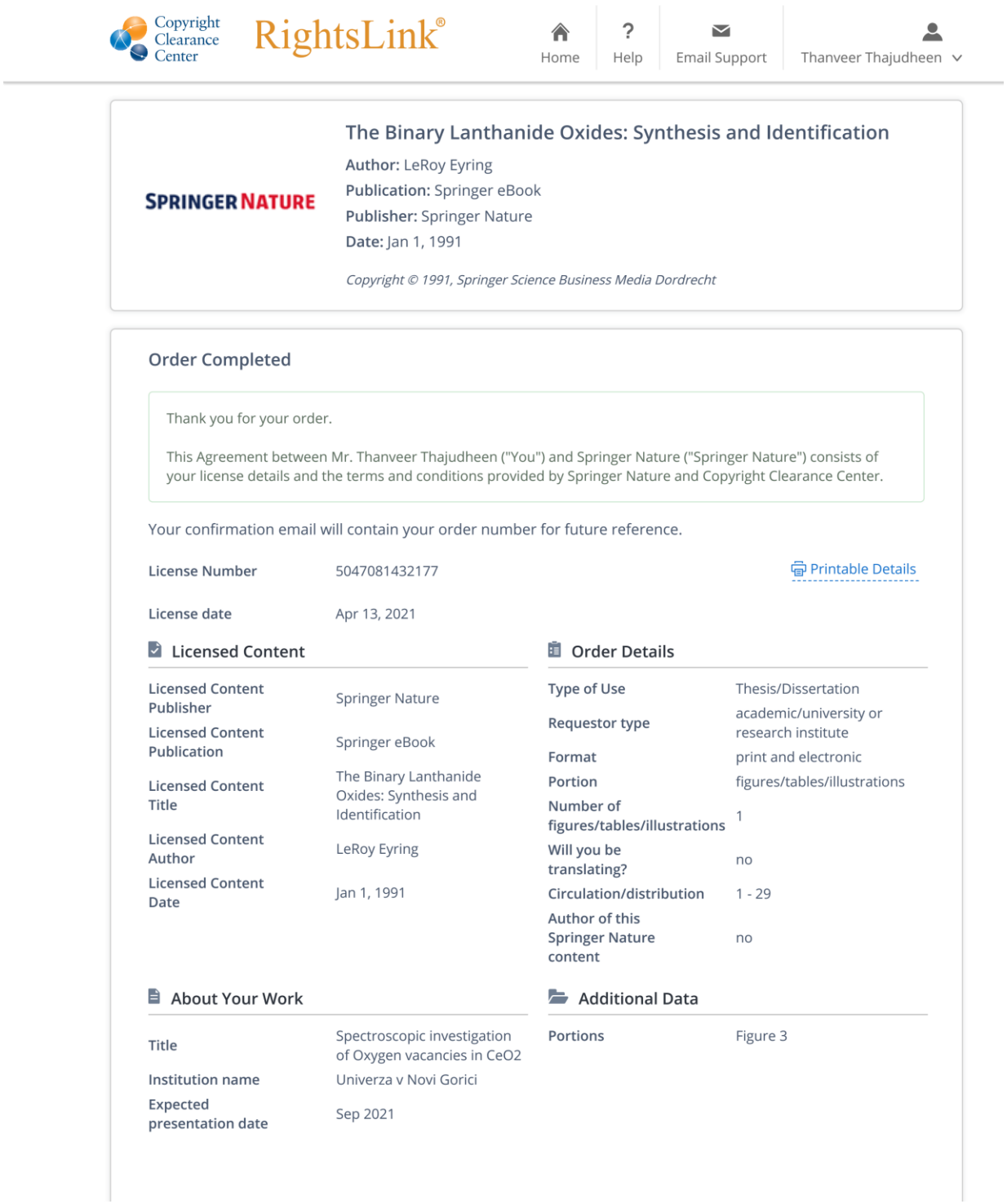

Requestor Location

Requestor Location	Mr. Thanveer Thajudheen Univerza v Novi Gorici Vipavska 11c SI-5270 Ajdovščina Ajdovščina, Nova Gorica 5270 Slovenia Attn: Mr. Thanveer Thajudheen

Price

Total	0.00 EUR

Tax Details

Total: 0.00 EUR

CLOSE WINDOW ORDER MORE

Permission for Figure 4.5

Licensed Content

Licensed Content Publisher	Elsevier
Licensed Content Publication	Journal of Luminescence
Licensed Content Title	Cathodoluminescence of cerium dioxide: Combined effects of the electron beam energy and sample temperature
Licensed Content Author	Jean-Marc Costantini,Pooreun Seo,Kazuhiro Yasuda,AKM Saiful Islam Bhuian,Tatsuhiko Ogawa,Didier Gourier
Licensed Content Date	Oct 1, 2020
Licensed Content Volume	226
Licensed Content Issue	n/a
Licensed Content Pages	1
Journal Type	S&T

Order Details

Type of Use	reuse in a thesis/dissertation
Portion	figures/tables/illustrations
Number of figures/tables/illustrations	1
Format	both print and electronic
Are you the author of this Elsevier article?	No
Will you be translating?	No

About Your Work

Title	Spectroscopic investigation of Oxygen vacancies in CeO2
Institution name	Univerza v Novi Gorici
Expected presentation date	Sep 2021

Additional Data

Portions	Figure 4.a

Requestor Location

Requestor Location	Mr. Thanveer Thajudheen Univerza v Novi Gorici Vipavska 11c SI-5270 Ajdovščina Ajdovščina, Nova Gorica 5270 Slovenia Attn: Mr. Thanveer Thajudheen

Tax Details

Publisher Tax ID	GB 494 6272 12

Price

Total	0.00 EUR

Total: 0.00 EUR

CLOSE WINDOW ORDER MORE